



universität  
wien

# DISSERTATION / DOCTORAL THESIS

Titel der Dissertation / Title of the Doctoral Thesis

„Graphene Nonlinearities for Quantum Computing.“

verfasst von / submitted by

Irati Alonso Calafell M.Sc.

angestrebter akademischer Grad / in partial fulfilment of the requirements for the degree of

Doktorin der Naturwissenschaften (Dr. rer. nat.)

Wien, 2020 / Vienna, 2020

Studienkennzahl lt. Studienblatt /  
degree programme code as it appears on  
the student record sheet:

A 796 605 411

Studienrichtung lt. Studienblatt /  
degree programme as it appears on  
the student record sheet:

Physik

Betreut von / Supervisor:

Univ.-Prof. Dipl.-Ing. Dr. Philip Walther



*Aitonari,  
nitaz harro izango zinelakoan.*

*To my grandpa,  
cause you would be proud of me.*



# Abstract

There is no doubt that the next great technological revolution will be brought about by the development of quantum technology. There are different approaches to build a universal quantum computer; from cold atoms or trapped ions, all the way to photons or superconducting circuits. Although these architectures are quite disparate, they each have many advantages and disadvantages. Therefore, it is not yet clear which the winning horse will be. In photonic quantum computing, the weak interaction of photons with their environment provides extremely long coherence times that could enable the realization of complex and intricate quantum algorithms. On top of this, they already allow one to transmit quantum information over very long distances with unbeatable speed and security. However, at the same time, this weak interaction with their surroundings hinders photon-photon interactions. As a result, the main drawback of photonic quantum computing is the lack of deterministic single-photon sources and quantum logic gates. Nevertheless, these challenges could be overcome by strong nonlinearities at the single-photon level.

In this thesis, I have worked both towards deterministic single-photon sources and quantum logic gates by taking advantage of the strong nonlinearity of graphene. On one hand, I propose a novel universal square-root of SWAP gate based on surface plasmons in graphene nanoribbons, whose strong nonlinearity provides a two-plasmon absorption larger than the single-plasmon absorption. This gives rise to a Zeno effect that prevents the system from evolving into failure states of the gate. The 99% success probability of our proposed gate could bring us closer to deterministic quantum gates, which would enable universal and scalable quantum computation. The strong two-plasmon absorption that this gate requires arises from the plasmon-assisted third-order nonlinearity in graphene, which has been predicted to be unprecedentedly high but has not yet been observed. To this end, we have experimentally explored the third-order nonlinearity in graphene by combining plasmons in graphene-metal heterostructures. Although the observed nonlinearity is not yet strong enough to drive nonlinear processes at the single-photon level, we measured an enhancement of 1500 on the third-harmonic signal and we found evidence of graphene plasmons present in the optical nonlinearity. This clearly indicates the potential of graphene to perform nonlinearities at the single-photon level.

Finally, parallel to the graphene investigations, we have implemented the first counterfactual communication protocol that relies on the Zeno effect to transmit a message without a weak trace of the photons travelling in the same direction. This experiment was carried out on a silicon-on-insulator nanophotonic processor, whose stability and tunability allowed us to counterfactually send a message from Bob to Alice while single-photons traveled from Alice to Bob with a bit error rate below 1%.



# Zusammenfassung

Die nächste große technologische Revolution wird zweifelsfrei durch Entwicklungen in der Quantentechnologie eingeleitet werden. Um den erhofften Durchbruch von Quantencomputern zu ermöglichen, gibt es unterschiedliche physikalische Systeme und Herangehensweisen; von kalten Atomen und Ionen bis hin zu Photonen oder supraleitenden Schaltkreisen. Obwohl sich diese unterschiedlichen physikalischen Strukturen sehr stark voneinander unterscheiden, haben alle ihre eigenen Vor- und Nachteile was das Rennen, welches System sich schlussendlich durchsetzen wird, zum jetzigen Zeitpunkt völlig offenlässt. Photonische Quantencomputer haben aufgrund der geringen Wechselwirkung zwischen Photonen und ihrer Umgebung, und den damit verbundenen langen Kohärenzzeiten, das Potential, komplexe Quantenalgorithmen realisierbar zu machen. Schon jetzt werden Photonen in der Quanteninformationstechnologie genutzt, um Daten sicher, schnell und über große Distanzen hinweg übertragen zu können. Andererseits ist genau diese schwache Wechselwirkung zwischen einem Photon und seiner Umgebung, und damit auch jene zwischen einzelnen Photonen selbst, das größte Hindernis für photonische Quantencomputer; es fehlt bis heute an deterministischen Einzelphotonenquellen und Quantengattern. Diese Herausforderungen könnten jedoch durch den Einsatz von starken Nichtlinearitäten auf Einzelphotonenniveau überwunden werden.

In dieser Dissertation beschäftige ich mich sowohl mit deterministischen Einzelphotonenquellen als auch mit Quantengattern unter Ausnutzung der starken optischen Nichtlinearität von Graphen. Ich zeige ein neues und universelles Quadratwurzel-SWAP-Gatter basierend auf Oberflächenplasmonen in Graphen-Nanobändern. Durch die starke Nichtlinearität dieser Struktur ist die Absorption von zwei Plasmonen stärker als jene eines einzelnen Plasmons; der damit einhergehende Zeno-Effekt verhindert, dass sich das System in Fehlerzustände des Gatters entwickelt. Unser vorgeschlagenes Gatter könnte uns durch dessen Erfolgswahrscheinlichkeit von 99% näher an ein deterministisches Quantengatter bringen, was unter anderem universelle und skalierbare Quanteninformationsverarbeitung ermöglichen würde. Die starke zeitgleiche Absorption von zwei Plasmonen, welche diese Gatter benötigt, basiert auf Graphens starker Nichtlinearität dritter Ordnung, die bisher zwar theoretisch vorausgesagt, aber experimentell noch nicht beobachtet wurde. In dieser Arbeit zeige ich unsere experimentelle Herangehensweise, um diesen Effekt dritter Ordnung durch die Kombination von Plasmonen in Graphen-Metall Heterostrukturen zu erforschen. Obwohl die von uns beobachtete Nichtlinearität noch nicht stark genug ist, um nichtlineare Effekte auf Einzelphotonenniveau zu erzeugen, so haben wir trotzdem eine Steigerung des Signals dritter Ordnung um den Faktor 1500 gemessen und zusätzlich experimentelle Beweise für die Existenz von Plasmonen in diesem Prozess gefunden. Dies zeigt eindeutig das Potential von Graphen, nichtlineare Effekte selbst auf Einzelphotonenniveau zu erzeugen, was wiederum deterministische Einzelphotonenquellen ermöglichen würde.

Zusätzlich zur Forschung mit Graphen, haben wir im Laufe meiner Dissertation ein kontrafaktisches Kommunikationsprotokoll basierend auf dem Zeno Effekt realisiert. In diesem Protokoll trennen wir eine eigentliche Nachricht von dem Medium, das die Information trägt, sodass wir im Experiment Nachricht und Photonen als Informationsträger in unterschiedliche Richtungen schicken. Dieses Experiment wurde auf einer integrierten photonischen Plattform durchgeführt, deren Stabilität und Durchstimbarkeit das kontrafaktische Überbringen einer Nachricht mit Einzelphotonen zwischen zwei Parteien ermöglichte. Die Bitfehlerrate bei einer Nachrichtenübertragung zwischen Alice und Bob ist dabei kleiner als 1%.

# Contents

<b>1</b>	<b>Introduction</b>	<b>3</b>
<b>2</b>	<b>Fundamentals of Photonics</b>	<b>7</b>
2.1	Linear Optics . . . . .	7
2.1.1	Maxwell's 1st equation: Gauss' Law . . . . .	8
2.1.2	Maxwell's 2nd equation: Gauss' law for Magnetism . . . . .	8
2.1.3	Maxwell's 3rd equation: Faraday's law of induction . . . . .	9
2.1.4	Maxwell's 4th equation: Ampere's Law . . . . .	9
2.2	Nonlinear Optics . . . . .	13
2.2.1	Second Harmonic Generation (SHG) . . . . .	14
2.2.2	Third Harmonic Generation (THG) . . . . .	15
2.2.3	Four Wave Mixing (FWM) . . . . .	15
<b>3</b>	<b>Fundamentals of Plasmonics</b>	<b>17</b>
3.1	Surface Plasmon Polaritons . . . . .	17
3.2	Localized Surface Plasmons . . . . .	20
3.3	Graphene Surface Plasmons launched via metallic antennas . . . . .	22
<b>4</b>	<b>Fundamentals of Graphene</b>	<b>27</b>
4.1	Electronic properties of graphene . . . . .	28
4.2	Optical properties of graphene . . . . .	30
<b>5</b>	<b>Fundamentals of Quantum Computing</b>	<b>35</b>
5.1	Qubits and entanglement . . . . .	35
5.2	Quantum logic gates . . . . .	37
5.2.1	Universal quantum gates . . . . .	39
5.3	Square-root of SWAP gate . . . . .	40
5.3.1	Optical qubit encoding . . . . .	42
5.3.2	Mathematics of a SWAP <sup>1/2</sup> based on a directional coupler . . . . .	45
5.4	The Zeno effect . . . . .	48
5.4.1	The Elitzur-Vaidman Bomb experiment . . . . .	50
<b>6</b>	<b>Experimental Graphene Research</b>	<b>53</b>
6.1	Quantum proposal . . . . .	53
6.2	Towards the quantum regime . . . . .	55
6.2.1	First steps in Exeter . . . . .	56
6.2.2	First steps in Vienna . . . . .	58
6.2.3	Success in Vienna . . . . .	59
6.2.3.1	Experimental details . . . . .	59
<b>7</b>	<b>Publications</b>	<b>69</b>
7.1	Quantum computing with graphene plasmons . . . . .	70

7.2	Trace-free counterfactual communication with a nanophotonic processor . . .	85
7.3	Giant enhancement of third-harmonic generation in graphene-metal heterostructures . . . . .	91
8	<b>Outlook</b>	105
8.1	Superconducting Nanowire Single-Photon detectors (SNSP) . . . . .	105
8.2	Looking for the first quantum signatures . . . . .	108
9	<b>Conclusion</b>	111



# Chapter 1

## Introduction

Photons interact weakly with their environment. On one hand, this property makes them extremely suitable for long-distance communication applications and provides extraordinarily long coherence times for quantum computation applications [79]. On the other hand, this characteristic hinders photon-photon interactions and hence, strong nonlinear processes at the single-photon-level remain a challenge. While this can be overcome for quantum computing applications at the cost of extra photons [48], the additional overhead makes purely linear-optical schemes difficult to scale up [64]. Alternatively, single-photon-level optical nonlinearities can be used to directly create deterministic gates [70]. Therefore, the main drawbacks of current photonic quantum computing could be overcome with strong optical nonlinearities.

Nonlinear plasmonics offers an unparalleled spatial control and spectral manipulation of light in a robust and high-fidelity manner for a wide range of applications, such as quantum information processing, ultrafast switching or sensing [8, 30]. In particular, metallic nanostructures are a promising candidate to enhance the nonlinear optical processes due to the ability of plasmons to strongly confine the electromagnetic fields down to the atomic scale and enhance optical nonlinear processes [56, 47]. Additionally, plasmon properties can be readily tailored by changing the shape and the materials that enclose these fields [88]. Nevertheless, as quantum computing is very sensitive to losses, the short lifetime of these metallic plasmons limits the effective strength of such nonlinear processes and prevents current applications to quantum information from scaling up.

As an alternative to metallic plasmons, in the last decade, graphene has been confirmed to be an exceptional platform to sustain electrically tuneable and long-lived plasmonic excitations in a wide spectral range [6, 49, 35, 28, 46, 97, 23, 96, 10, 24]. As a matter of fact, third-harmonic generation (THG) [51, 45, 40, 87], four-wave mixing (FWM) [37, 14, 45], optical Kerr effect [100, 17] and high-harmonic generations [98] have already been observed, exhibiting remarkably large nonlinear effects. This thesis aims to theoretically and experimentally explore graphene nonlinearities and enhance them by using heterostructures to achieve the ultimate limit; that is, nonlinear effects at the single-photon level.

We have theoretically developed a square-root of SWAP gate based on a directional coupler built with graphene nanoribbons as plasmonic waveguides, where the plasmonic excitations are used to encode qubits. Thanks to the strong two-plasmon absorption in graphene, which is a direct consequence of its high third-order nonlinearity, the Zeno effect prevents the gate

from evolving into those failure output states in which two plasmons are found in the same output port. We have theoretically shown that, even at room temperature, this nonlinear gate suppresses those failure states arising from the Hong-Ou-mandel effect and achieve a 87% success probability with current state of the art technology. Moreover, this success can be further enhanced up to 99% when the gate is cooled down to cryogenic temperatures. This efficiency would thus enable large scale universal quantum computing. This work is described in detail in Section 7.1.

The main focus of this thesis is the experimental study and characterization of enhanced optical nonlinearities in graphene heterostructures. Bare graphene has shown unprecedentedly high optical nonlinearities [45], well above those found in standard nonlinear crystals [37], and closer to those in atomic systems [5]. However, contrary to atomic systems, graphene does not require any vacuum or cryogenic environment, making it extremely suitable for scalable applications. Unfortunately, in practice, this nonlinearity is limited by the nm-scale thickness of such nonlinear samples; effectively showing weaker nonlinear effects than those in bulk nonlinear crystals. In order to compensate for this limitation, we study two main approaches to enhance graphene's nonlinearity. First, we use graphene-metal heterostructures in which gold nanoribbons are etched on top of the bare graphene. This allows one to resonantly excite metallic plasmons in the gold nanoribbons, which will then interact with the graphene to create nonlinear signals. Using this nanotechnology, we report a three-order of magnitude enhancement on third-harmonic generation (THG), compared to bare graphene. Secondly, we electrically dope the graphene. This enables us to tune the Fermi energy of the system and reach plasmonic resonances. Although we were not able to observe a major enhancement due to plasmons driving the nonlinearity [42], we did observe a modified THG signal that is explained by the excitation of surface plasmon polaritons (SPP) in the system. We expect to see such a plasmonic enhancement in the future, with higher quality devices and different methods to further tune the Fermi energy. Further details of this experiment can be found in Section 7.3.

During this thesis, as a parallel project, we had the opportunity to experimentally demonstrate a new protocol of counterfactual communication, where the single-photons and the transmitted information travel in opposite directions. This experiment was based on the protocol introduced by Arvidsson-Shukur, *et al.* [3], which takes advantage of the Zeno effect to be the first protocol to achieve counterfactual communication without any weak-trace of the photons travelling in the same direction as the information. The experiment was performed in a silicon-on-insulator nanophotonic processor, whose stability allowed us to achieve successful bit transmission rates above 99%. A more comprehensive study of this experiment can be found in Section 7.2.

In order to provide a pedagogical basis, the first chapters of this thesis are dedicated to the

introduction of the topics that are significant for the understanding of the work presented here. We first introduce the fundamentals of photonics (Section 2), which is the most relevant topic throughout the entire thesis. We continue with the fundamentals of plasmonics (Section 3), in general, and make a special mention to plasmons in graphene. The fundamentals of graphene itself are given in Section 4. Finally, in Section 5 we talk about the fundamentals of quantum computing, which is the main motivation of this thesis.

In addition to the publications collected in Section 7, the experimental results given in Section 6 aims to provide the reader a reasoning about the course of this thesis. Closing the thesis, I have added a final section (Section 8), where the promising future directions are summarized.



# Chapter 2

## Fundamentals of Photonics

Photonics is the science of light, studying the generation, manipulation and detection of photons; i.e. the unit of light, equivalent to the electron in electricity, with both wave- and particle-like behavior. Scientist have pursued the understanding of light, its properties and applications for centuries: from the foundation for modern optics established in ancient Greece by Socrates, Plato, Aristotle and Euclid around the 5th century B.C. [9], to the latest discovery of self-torquing property of light [78]. However, it was not till 1930s, with the discovery of the transmission electron microscope (TEM)[81] and the scanning electron microscope (SEM)[92], that technology allowed us to overcome the diffraction limit associated with lenses and microscopes [2], and we were able to image at the nanometer scale.

Once the nanoscale could be imaged, the next challenge was to actually squeeze light down to the nanoscale, achieving confinements well below the wavelength [29]. This field, known as nanophotonics, investigates materials and techniques to control light in the nanoscale. An example of these are surface plasmons polaritons in nanometric metal objects [36, 22] or nanoscale tips such as those used in near-field scanning optical microscopy [38]. This constitutes a whole field known as plasmonics, which will be further studied in Chapter 3, as plasmons play an important role in the work presented in this thesis.

Quantum photonics is another important branch of photonics that is relevant to this work [54]. Quantum photonics aims to understand and prove quantum mechanical effects using photons, which have been proved to be suitable to exploit quantum phenomena because of their minimal interaction with the environment. This property allows us to propagate quantum states for very long distances and to achieve long interaction times. Furthermore, photons have many degrees of freedom onto which quantum states can be prepared, processed and measured with relative simplicity. All these characteristics make quantum photonics an extremely fitting platform for quantum computation and information applications. This will be further discussed in Chapter 5.

### 2.1 Linear Optics

Light is an electromagnetic wave created by charge and current densities,  $\rho$  and  $\mathbf{j}$ . As such, from a classical perspective, it is possible to describe it as a solution of Maxwell's equations

given by,

$$\nabla \cdot \mathbf{D}(\mathbf{r}, t) = 4\pi\rho(\mathbf{r}, t) \quad (2.1a)$$

$$\nabla \cdot \mathbf{B}(\mathbf{r}, t) = 0 \quad (2.1b)$$

$$\nabla \times \mathbf{E}(\mathbf{r}, t) = -\frac{1}{c} \frac{\delta}{\delta t} \mathbf{B}(\mathbf{r}, t) \quad (2.1c)$$

$$\nabla \times \mathbf{H}(\mathbf{r}, t) = \frac{1}{c} \left[ \frac{\delta}{\delta t} \mathbf{D}(\mathbf{r}, t) + 4\pi\mathbf{j}(\mathbf{r}, t) \right] \quad (2.1d)$$

where  $\mathbf{E}(\mathbf{r}, t)$  and  $\mathbf{H}(\mathbf{r}, t)$  are the electric and magnetic field, respectively,  $\mathbf{D}(\mathbf{r}, t)$  is the electric displacement and  $\mathbf{B}(\mathbf{r}, t)$  is the magnetic induction [59]. Before proceeding with the mathematical description of an electromagnetic wave in a nanophotonic platform, we will start with a deeper explanation of each of the Maxwell's equations, as they are the main starting point of any of the topics studied in this thesis.

### 2.1.1 Maxwell's 1st equation: Gauss' Law

This equation dictates how the electric field behaves around electric charges. We first need to understand the conceptual meaning of the divergence  $\nabla \cdot$ , which mathematically is equivalent to

$$\nabla \cdot \mathbf{F} = \frac{\delta F_x}{\delta x} + \frac{\delta F_y}{\delta y} + \frac{\delta F_z}{\delta z}, \quad (2.2)$$

where  $F_x, F_y$  and  $F_z$  are the x, y and z components of the field, respectively. If we consider a point  $\mathbf{r} = (x, y, z)$ , the divergence is the measure of the vector flow that would cross a certain surface surrounding this point  $\mathbf{r}$ .

As sketched in Fig. 2.1a, if the total vector field flows away of this point (flows outside the surface) the divergence would give a positive result. However, if the total vector field would flow towards this point  $\mathbf{r}$  (flows inside the surface), the divergence would be negative. Thus, Gauss' law states that the total electric flux exiting any determined volume is equal to the total charge inside this volume.

### 2.1.2 Maxwell's 2nd equation: Gauss' law for Magnetism

In principle, Gauss's law for magnetism states the same as his law for electric fields; that the divergence of the magnetic flux density is equal to the magnetic charge density. However, to date, no one has found a magnetic charge so we set the right hand side of the equation to zero. In other words, no particle that produces a magnetic field has yet been discovered.

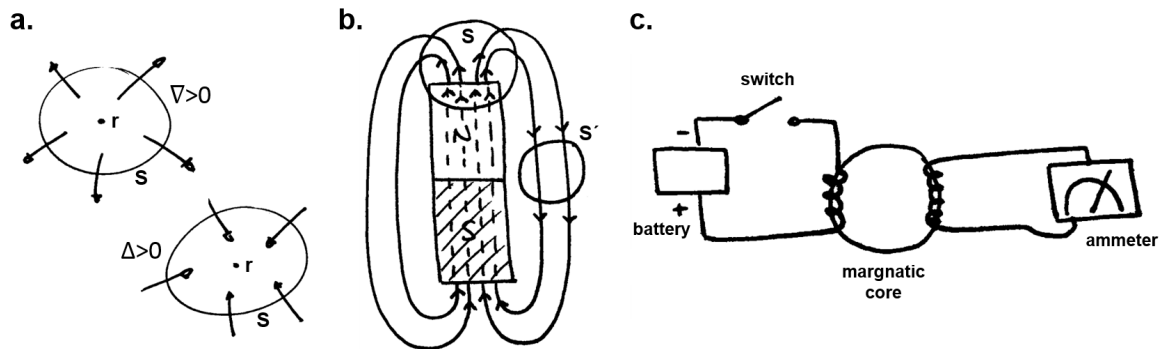


**Figure 2.1. Conceptual sketches to understand Maxwell's equations** **a.** When the total vector field flows exiting the surface given by  $S$ , the divergence will be positive. In contrast, when the divergence is negative, it indicates that the total vector field flows inside  $S$ . **b.** Sketch of magnetic fields around a magnet. The divergence of any given surface, such as  $S$  or  $S'$ , is always zero, indicating that there is no source of magnetic field. **c.** Faraday's experiment that made him discover that an electric field changing in space induces a magnetic field changing in time.

But, what about magnets? If one studies the divergence at different points around a magnet (see Fig. 2.1b), one finds that this is always zero. Even at the edge of the poles, when the field crossing the magnet (dashed line) is considered, the total vector flow cancels out. Moreover, this fact also explains the inexistence of monopoles.

### 2.1.3 Maxwell's 3rd equation: Faraday's law of induction

This law shows the relation between electric and magnetic fields and the influence they have on each other. In Fig. 2.1 we show a sketch of Faraday's experiment, where he connected a battery to a magnetic core via a metallic wire and connected an ammeter on the other side of the core. He observed that when he closed the switch, the current would flow and this could be measured on the ammeter; say 5A. But this would only hold for a very short time and then it would only read 0A. On the other hand, if he would open the switch, the ammeter would show -5A and then go back to 0A. After these observations, Faraday came up with the following conclusion: a changing electric field in space gives rise to a changing magnetic field in time and *vice versa*.

### 2.1.4 Maxwell's 4th equation: Ampere's Law

So as to understand this equation, we will consider the two terms on the right hand side of the equation independently. In fact, the initial expression derived by Ampere in 1826 only contained the first term,

$$\nabla \times \mathbf{H} = \mathbf{j}. \quad (2.3)$$

This claims that if there is a current flowing through a wire, this creates a magnetic field circling around it, where the circulation direction follows the right-hand rule. It is easier to see this interpretation when considering the problem in two dimensions; that is,

$$\oint H \, dL = I_{enc} \quad (2.4)$$

where  $L$  is the path delimiting an area around the wire where the current flows, and  $I_{enc}$  represents the enclosed electrical current. This law was well accepted until 1865, when Maxwell noticed that there was something wrong when the divergence of both sides of the equation was calculated; namely,

$$\nabla \cdot (\nabla \times \mathbf{H}) = \nabla \cdot \mathbf{j}. \quad (2.5)$$

As a matter of fact, the divergence of the curl of any vector is always zero, which would imply that the divergence of any current density is always zero, which is not true. A capacitor is a good example of this, since the current flows to one plate but does not flow towards the other one, resulting in a nonzero divergence. As a solution to this, Maxwell thought about the symmetry and reciprocity inherent to all the set of electromagnetic equations. So, if an electric field changing in space would give rise to a magnetic field changing in time (3rd equation), why would not a magnetic field changing in space give rise to an electric field (electric density flux  $\mathbf{D}$ ) changing in time. This is thus the adjustment that Maxwell made to Ampere's law to come up with his 4th equation.

Now that we have an intuitive understanding of the effects that Maxwell's equations describe, we can proceed to find solutions to them. To solve this set of equations, we first need some constitutive relations, which give the dependence of the intrinsic fields of materials on the external electromagnetic fields applied to them; that is,  $\mathbf{D} = \mathbf{D}[\mathbf{E}, \mathbf{H}]$  and  $\mathbf{B} = \mathbf{B}[\mathbf{E}, \mathbf{H}]$ . In the case of an isotropic, homogeneous, linear and nonmagnetic ( $\mu = 1$ ) medium with permittivity  $\epsilon$ , these constitutive relations are

$$\mathbf{D}(\mathbf{r}, t) = \iint \epsilon(\mathbf{r} - \mathbf{r}', t - t') \mathbf{E}(\mathbf{r}', t') \, dt' \, d\mathbf{r}' \quad (2.6a)$$

$$\mathbf{H}(\mathbf{r}, t) = \mathbf{B}(\mathbf{r}, t). \quad (2.6b)$$

In the case of standard materials and for sufficiently large structures (larger than the Fermi wavelength  $\lambda_F = \sqrt{4\pi/n} = f_{vF}/E_F \sim 10.33 \text{ nm}$  for  $E_F = 0.4 \text{ eV}$ ), we can neglect the dependence of the field on position  $\mathbf{r}$  on the field applied on position  $\mathbf{r}'$ ; i.e. we can ignore any spatial dispersion or nonlocality. However, at time  $t$  we need to consider the field previously applied at time  $t'$ . In other words, temporal dispersion needs to be accounted for. Thus we can

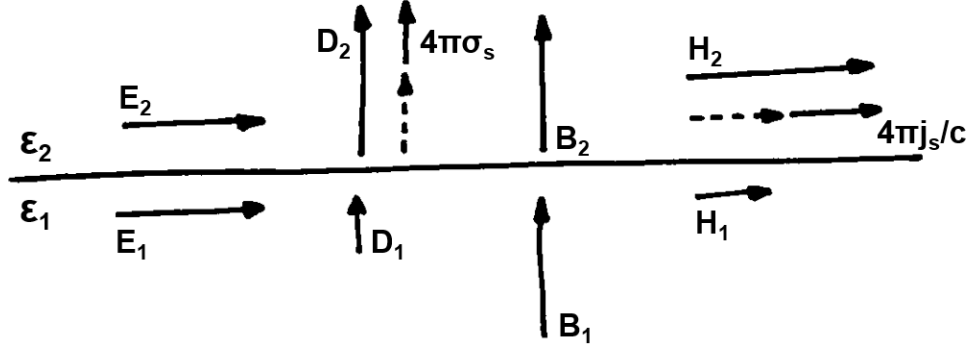


**Figure 2.2. Continuity conditions.** The fields in the interface between two materials with permittivities  $\epsilon_1$  and  $\epsilon_2$ .

rewrite the first constitutive relation, Eq. eq. (2.6a), as

$$\mathbf{D}(\mathbf{r}, t) = \int \epsilon(\mathbf{r}, t - t') \mathbf{E}(\mathbf{r}, t') dt'. \quad (2.7)$$

Furthermore, to simplify the equations, it is convenient to get rid off the time convolution by applying a Fourier transformation to convert the equations to the frequency domain instead. We do this by exchanging

$$\mathbf{E}(\mathbf{r}, \omega) = \int \mathbf{E}(\mathbf{r}, t) e^{i\omega t} \quad (2.8a)$$

$$\mathbf{E}(\mathbf{r}, t) = \int \frac{d\omega}{2\pi} \mathbf{E}(\mathbf{r}, \omega) e^{-i\omega t}. \quad (2.8b)$$

Note that due to the fact that the fields are real values in space-time, we also need to consider that  $\mathbf{E}^*(\mathbf{r}, \omega) = \mathbf{E}(\mathbf{r}, -\omega)$  when transforming the domain. After these changes, Maxwell's equations read

$$\nabla \cdot \mathbf{D}(\mathbf{r}, \omega) = 4\pi\rho(\mathbf{r}, \omega) \quad (2.9a)$$

$$\nabla \cdot \mathbf{B}(\mathbf{r}, \omega) = 0 \quad (2.9b)$$

$$\nabla \times \mathbf{E}(\mathbf{r}, \omega) = ik\mathbf{B}(\mathbf{r}, \omega) \quad (2.9c)$$

$$\nabla \times \mathbf{H}(\mathbf{r}, \omega) = -ik\mathbf{D}(\mathbf{r}, \omega) + \frac{4\pi}{c}\mathbf{j}(\mathbf{r}, \omega), \quad (2.9d)$$

and the constitutive relations simplify to

$$\mathbf{D}(\mathbf{r}, \omega) = \epsilon(\omega)\mathbf{E}(\mathbf{r}, \omega) \quad (2.10a)$$

$$\mathbf{H}(\mathbf{r}, \omega) = \mathbf{B}(\mathbf{r}, \omega), \quad (2.10b)$$

where  $k = \omega/c$  is the wave number of the incident electromagnetic wave and the characteristics

of the studied material are contained in  $\epsilon(\omega)$ .

Additionally, Maxwell's equations should also ensure charge conservation throughout the application of electromagnetic fields to the system. This condition leads to the continuity equation,

$$\nabla \cdot \mathbf{j}(\mathbf{r}, \omega) = i\omega\rho(\mathbf{r}, \omega), \quad (2.11)$$

where  $\mathbf{j}(\mathbf{r}, \omega)$  and  $\rho(\mathbf{r}, \omega)$  are the frequency-dependent current and charge densities, respectively.

We can further consider these electromagnetic fields in the absence of free charges or currents, as in the case of vacuum or a dielectric material. In this case, Maxwell's equations can be reduced to

$$\nabla \cdot \mathbf{E}(\mathbf{r}, \omega) = 0 \quad (2.12a)$$

$$\nabla \cdot \mathbf{B}(\mathbf{r}, \omega) = 0 \quad (2.12b)$$

$$\nabla \times \mathbf{E}(\mathbf{r}, \omega) = \frac{\epsilon}{c^2} \frac{\delta \mathbf{E}}{\delta t} \quad (2.12c)$$

$$\nabla \times \mathbf{B}(\mathbf{r}, \omega) = -\frac{\delta \mathbf{B}}{\delta t}. \quad (2.12d)$$

By combining the equations with the curls, we can write the so-called Helmholtz wave equations for the electric and magnetic fields as

$$\left( \nabla^2 - \frac{1}{v^2} \frac{\delta^2}{\delta t^2} \right) \{ \mathbf{E}(\mathbf{r}, t), \mathbf{B}(\mathbf{r}, t) \} = 0, \quad (2.13)$$

which is the solution of an electromagnetic wave traveling at speed  $v = c/\sqrt{\epsilon}$ .

All the equations presented above are applicable inside homogenous media, but very often electromagnetic waves travel through different materials with different electric or magnetic properties. In this case, one needs to study the interface between two materials by considering the following continuity conditions [44]:

$$\mathbf{n}_z \times (\mathbf{E}_2 - \mathbf{E}_1) = 0 \quad (2.14a)$$

$$\mathbf{n}_z \cdot (\mathbf{D}_2 - \mathbf{D}_1) = 4\pi\sigma_s \quad (2.14b)$$

$$\mathbf{n}_z \cdot (\mathbf{B}_2 - \mathbf{B}_1) = 0 \quad (2.14c)$$

$$\mathbf{n}_z \times (\mathbf{H}_2 - \mathbf{H}_1) = \frac{4\pi}{c} \mathbf{j}_s \quad (2.14d)$$

where  $\mathbf{n}_z$  is the unitary normal vector perpendicular to the face between the materials with permittivities  $\epsilon_1$  and  $\epsilon_2$ ,  $\sigma_s$  is the surface charge density and  $\mathbf{j}_s$  is the surface current density. In

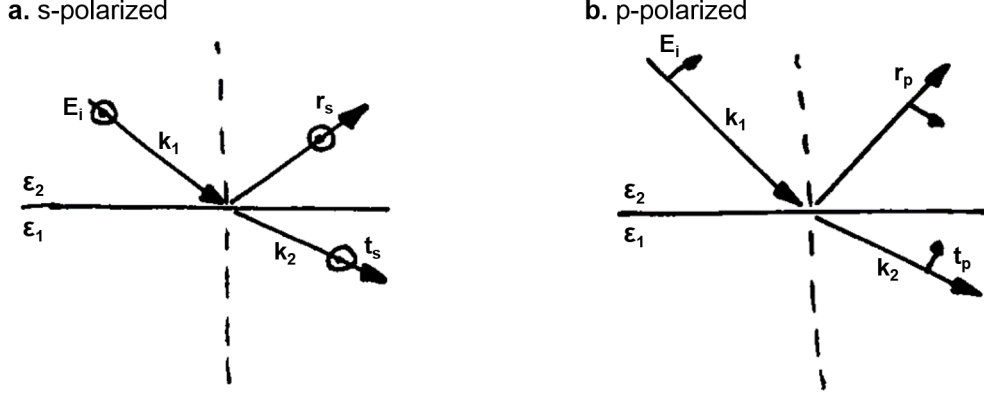


**Figure 2.3. Sketch of Fresnel coefficients.** Refraction and transmission components of an incident **a.** *s*-polarized and (TE mode) **b.** *p*-polarized (TM mode) light.

Fig. 2.2 we represent the continuity conditions for fields applied in material 1 and transmitted to material 2.

More interestingly, these boundary conditions also allow one to calculate the remaining transmitted  $t$  and reflected  $r$  waves after the incident electromagnetic field reaches the interface. These relations are known as the Fresnel coefficients and, assuming nonmagnetic materials, they are given by

$$\begin{aligned} r_p &= \frac{\epsilon_2 k_{1\perp} - \epsilon_1 k_{2\perp}}{\epsilon_2 k_{1\perp} + \epsilon_1 k_{2\perp}} & t_p &= \sqrt{\frac{\epsilon_2}{\epsilon_1}} \frac{k_{1\perp}}{k_{2\perp}} \\ r_s &= \frac{k_{1\perp} - k_{2\perp}}{k_{1\perp} + k_{2\perp}} & t_s &= 1 + r_s \end{aligned} \quad (2.15)$$

where  $k_{i\perp}$  and  $\epsilon_i$  are the perpendicular components to the interface (parallel to  $\mathbf{n}_z$ ) of the incident wave vector and the dielectric constant of materials 1 and 2, respectively.

Moreover, we consider the polarization of the incoming field as sketched in Fig. 2.3. It is called the *s*-polarized or TE mode when the electric component of the field is perpendicular to the incidence plane and *p*-polarized or TM when the electric field is parallel to the incidence plane.[43]

## 2.2 Nonlinear Optics

Light-light interactions have not yet been observed in vacuum; a nonlinear medium is necessary. These nonlinear materials are characterized by their nonlinear polarization  $P(\omega)$  (dipole moment per unit area), which allows mixing different fields to create new ones, respecting both energy and momentum conservation. This polarization should not be confused with the

one presented in the previous section: the former describes the direction in which the electric field of the wave oscillates with respect to the incidence plane, and the latter specifies the ease with which the electrons in a material follow the oscillations of the electromagnetic field. Mathematically, the polarization (as in the electron response) is written as

$$\mathbf{P}(\omega) = \epsilon_0 \left( \chi^{(1)}(\omega) E_{\text{ext}}(\omega) + \chi^{(2)}(\omega) E_{\text{ext}}^2(\omega) + \chi^{(3)}(\omega) E_{\text{ext}}^3(\omega) + \dots \right) \quad (2.16)$$

where  $E_{\text{ext}} = E_0(e^{i\omega t} + e^{-i\omega t})$  for a monochromatic plane wave with frequency  $\omega$ , and  $\chi^{(n)}$  is the  $n$ -order susceptibility [8]. In this expression we can distinguish the linear polarization to be  $P^{(1)}(\omega) = \chi^{(1)}(\omega) E_{\text{ext}}$ , while  $P^{(2)}(\omega) = \chi^{(2)}(\omega) E_{\text{ext}}^2$  and  $P^{(3)}(\omega) = \chi^{(3)}(\omega) E_{\text{ext}}^3$  are the second- and third-order polarizations, respectively. It is worth mentioning that there is no limit to the polarization terms. Now we proceed to study three of the most relevant nonlinear effects: second harmonic generation (SHG), third harmonic generation (THG) and four-wave mixing (FWM).

### 2.2.1 Second Harmonic Generation (SHG)

Recalling the form of  $E_{\text{ext}}$ , if we expand the second-order polarizability, we can rewrite it as follows:

$$P^{(2)}(\omega) = \chi^{(2)} E_{\text{ext}}^2 \quad (2.17a)$$

$$P^{(2)}(\omega) = \chi^{(2)} E_0^2 \left[ 1 + (e^{2i\omega t} + e^{-2i\omega t}) \right] \quad (2.17b)$$

$$P^{(2)}(\omega) = 2\chi^{(2)} E_0^2 [1 + \cos(2\omega t)] \quad (2.17c)$$

where the first term corresponds to a DC component that does not lead to any photon emission but simply increases the internal electric field in the nonlinear material. However, the second term shows a much more exciting term, where an electromagnetic field with double the frequency is created. Therefore, in this process, two external fields with frequency  $\omega$  combine to give rise to the emission of a single field with frequency  $2\omega$ . This phenomenon is known as second harmonic generation (SHG). Note that, in practice, these two fields with  $\omega$  can be part of a single beam.

### 2.2.2 Third Harmonic Generation (THG)

Once again, if we expand the third-order polarization, we end up with the expression

$$P^{(3)}(\omega) = \chi^{(3)} E_{\text{ext}}^3 \quad (2.18a)$$

$$P^{(3)}(\omega) = \frac{1}{8} \chi^{(3)} E_0^3 \left[ (e^{3i\omega t} + e^{-3i\omega t}) + 3(e^{i\omega t} + e^{-i\omega t}) \right] \quad (2.18b)$$

$$P^{(3)}(\omega) = \frac{1}{4} \chi^{(3)} E_0^3 [\cos(3\omega t) + 3 \cos(\omega t)] \quad (2.18c)$$

Here we also find two different terms. The first one corresponds to the so-called third-harmonic generation, where three fields with frequency  $\omega$  combine to create a single field with frequency  $3\omega$ . The second term, on the other hand, has the same frequency as the incident one. However, this term is responsible for shifting the refractive index of the nonlinear medium and it is known as the AC Kerr effect.

### 2.2.3 Four Wave Mixing (FWM)

We can also consider cases in which the fields are non-degenerate; i.e., they have different frequencies. There are many different combinations that one can study but for this thesis we will only introduce the case in which two different fields,  $E_{\text{ext},1} = E_1(e^{i\omega_1 t} + e^{-i\omega_1 t})$  and  $E_{\text{ext},2} = E_2(e^{i\omega_2 t} + e^{-i\omega_2 t})$ , mix together. This is known as four-wave mixing (FWM) and it can be derived as

$$P^{(3)}(\omega) = \chi^{(3)} E_{\text{ext},1}^2 E_{\text{ext},2} \quad (2.19a)$$

$$P^{(3)}(\omega) = \chi^{(3)} E_1^2 E_2 \left[ (e^{i(2\omega_1 + \omega_2)t} + e^{-i(2\omega_1 + \omega_2)t}) + (e^{i(2\omega_1 - \omega_2)t} + e^{-i(2\omega_1 - \omega_2)t}) \right] \quad (2.19b)$$

$$+ 2(e^{i\omega_2 t} + e^{-i\omega_2 t}) \quad (2.19c)$$

$$P^{(3)}(\omega) = 2\chi^{(3)} E_1^2 E_2 [\cos(2\omega_1 + \omega_2)t + \cos(2\omega_1 - \omega_2)t + 2 \cos(\omega_2 t)] \quad (2.19d)$$

In this solution we distinguish two main nonlinear processes: the first one where the frequencies are added is known as sum-frequency mixing (SFM) and the second one in which the frequencies are subtracted is called difference-frequency mixing (DFM). Note that, in practice, when the two input fields are mixed, the process will not distinguish  $E_{\text{ext},1}^2 E_{\text{ext},2}$  from  $E_{\text{ext},1} E_{\text{ext},2}^2$  and both processes will equally happen, given that the intensity of the fields is the same, unless there is something else going on, like phase matching. The third term is another field with the same incident frequency  $\omega_2$ , which is responsible for shifting the refractive index of the material, as explained in the case of THG.

In this chapter we have introduced the basics of photonics and gave special attention to nonlinear processes, as these are fundamental to the work presented in this thesis. In particular,

we have used THG to characterize the nonlinear strength of our graphene heterostructure devices and we will proceed with FWM experiments, as this process can lead to the emission of single-photons.

# Chapter 3

## Fundamentals of Plasmonics

One of the main goals of current nanophotonics is the control and manipulation of light in the nanoscale. However, due to the diffraction limit, one cannot simply focus light as tightly as one wants [2]. Thus, new venues need to be explored. Here we will introduce plasmons, which are one of the most promising approaches to confining light beyond the diffraction limit. When the electromagnetic wave of a photon impinges into a conductive material (most frequently metals), the free electrons in the conduction band follow the oscillations of the electrical field of the photon, creating a wave of electrons with a frequency that can be up to three orders of magnitude larger than that of the initial photon that excited this electron wave (see Fig. 3.1a) [71]. These electron waves are known as plasmons and their behaviour is similar to that of electromagnetic waves. Depending on the location of these electronic oscillations, we distinguish between bulk and surface plasmons. However, the high energy of the former hinders their applicability in current technology. Among the latter, on the other hand, there are two main types: surface plasmon polaritons (SPP) and localized surface plasmons (LSP). In the following sections we aim to emphasize the different nature of these [56, 33].

### 3.1 Surface Plasmon Polaritons

Surface plasmon polaritons (SPP) are optical modes found at the interface between two different materials, confined in the perpendicular direction. In Fig. 3.1b the simplest structure that can contain plasmons is shown: the interface between a dielectric material with a real positive dielectric constant,  $Re[\epsilon_2] > 0$ , and a metal with  $\epsilon_1(\omega)$ . The conductive nature of the first material is given when  $Re[\epsilon_1(\omega)] < 0$ , which in the case of metals happens for frequencies below the plasma frequency [4],

$$\omega_p = \sqrt{\frac{4\pi n e^2}{m_e^*}} \quad (3.1)$$

where  $n$  is the electron density in the conduction band,  $e$  is the electron charge and  $m_e^*$  is the effective electron mass.

Starting from Maxwell's equations one can derive the wave equation as

$$\nabla^2 \mathbf{E} - \frac{\epsilon}{c^2} \frac{\delta^2 \mathbf{E}}{\delta t^2} = 0 \quad (3.2)$$

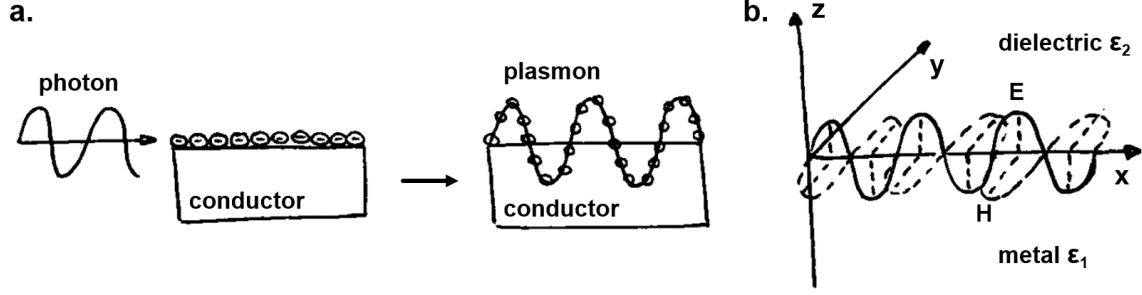


**Figure 3.1. Plasmon.** **a.** When a photon impinges into a metal, the free electrons in the conduction band follow the electromagnetic oscillation, creating a wave of electrons, known as plasmon, whose wavelength can be three times shorter than that of the initial photon. **b.** We look for plasmonic modes in the interface between two materials with opposite real dielectric constant signs; i.e., a conductor and a dielectric, where the modes propagate in the  $x$ -direction ( $\beta = k_x$ ) and are confined in the  $z$ -direction. Note that the plasmon field decays in the  $x$ -direction as  $e^{i\beta x}$ . However, for the sake of clarity, this is not represented in the sketch.

from which the TE ( $s$ -polarized) and TM ( $p$ -polarized) wave solutions can be calculated. Note that here we will always look for solutions of propagating waves confined in the interface; i.e. with an evanescent component in the  $z$ -direction [56]. In the case of an incident TE mode the field components are

$$z > 0 \quad \begin{cases} E_y(z) = A_2 e^{i\beta x} e^{-k_2 z} \\ H_x(z) = -i A_2 \frac{1}{\omega \mu_0} k_2 e^{i\beta x} e^{-k_2 z} \\ H_z(z) = A_2 \frac{\beta}{\omega \mu_0} e^{i\beta x} e^{-k_2 z} \end{cases} \quad (3.3)$$

and

$$z < 0 \quad \begin{cases} E_y(z) = A_1 e^{i\beta x} e^{k_1 z} \\ H_x(z) = i A_1 \frac{1}{\omega \mu_0} k_1 e^{i\beta x} e^{k_1 z} \\ H_z(z) = A_1 \frac{\beta}{\omega \mu_0} e^{i\beta x} e^{k_1 z} \end{cases} \quad (3.4)$$

Using the continuity conditions given in Eq. 2.14 we find the relation between  $A_1$  and  $A_2$  to be

$$\left. \begin{aligned} \mathbf{n}_z \times (\mathbf{E}_2 - \mathbf{E}_1) = 0 &\rightarrow E_{1,y} = E_{2,y} \\ \mathbf{n}_z \times (\mathbf{H}_2 - \mathbf{H}_1) = 0 &\rightarrow H_{1,x} = H_{2,x} \end{aligned} \right\} A_1(k_1 + k_2) = 0, \quad A_1 = A_2 \quad (3.5)$$

Since  $\text{Re}[k_1, k_2] > 0$ , this relation forces  $A_1 = 0$  and because  $A_1 = A_2 = 0$ , we conclude that no plasmonic excitation can occur when the incident light is in a TE mode.

Let us now study the case in which the incident light is in a TM mode. The Field components

are given by

$$z > 0 \quad \begin{cases} H_y(z) = A_2 e^{i\beta x} e^{-k_2 z} \\ E_x(z) = iA_2 \frac{1}{\omega \epsilon_0 \epsilon_2} k_2 e^{i\beta x} e^{-k_2 z} \\ E_z(z) = -A_1 \frac{\beta}{\omega \epsilon_0 \epsilon_2} e^{i\beta x} e^{-k_2 z} \end{cases} \quad (3.6)$$

and

$$z < 0 \quad \begin{cases} H_y(z) = A_1 e^{i\beta x} e^{k_1 z} \\ E_x(z) = -iA_1 \frac{1}{\omega \epsilon_0 \epsilon_1} k_1 e^{i\beta x} e^{k_1 z} \\ E_z(z) = -A_1 \frac{\beta}{\omega \epsilon_0 \epsilon_1} e^{i\beta x} e^{k_1 z} \end{cases} \quad (3.7)$$

Once again, we use the continuity conditions to find the relations between the parameters to be

$$\left. \begin{aligned} \mathbf{n}_z \times (\mathbf{E}_2 - \mathbf{E}_1) = 0 &\rightarrow E_{1,y} = E_{2,y} \\ \mathbf{n}_z \times (\mathbf{H}_2 - \mathbf{H}_1) = 0 &\rightarrow H_{1,x} = H_{2,x} \end{aligned} \right\} \frac{k_2}{\epsilon_2} = -\frac{k_1}{\epsilon_1}, \quad A_1 = A_2 \quad (3.8)$$

This relation is thus a confirmation that plasmons can only exist in the interface between materials with opposite sign permittivities; that is, a conductor and a dielectric. As a remark, note that the solutions in equations 3.7 and 3.8 describe an electromagnetic wave propagating along the  $x$ -axis ( $\beta = k_x$ ), where the electric field oscillates in the  $x$ - $z$  plane and the magnetic field in the  $x$ - $y$  plane (see Fig. 3.1b). In the case of TM modes, the  $H_y$  field component also needs to fulfill the wave equation given by

$$\frac{\delta^2 H_y}{\delta z^2} + (k_0^2 \epsilon - \beta^2) H_y = 0, \quad (3.9)$$

from which we find that

$$k_1^2 = \beta^2 - k_0^2 \epsilon_2 \quad (3.10a)$$

$$k_2^2 = \beta^2 - k_0^2 \epsilon_1. \quad (3.10b)$$

Now, by combining these two expressions, we can derive the dispersion relation of the plasmon

$$\beta = k_0 \sqrt{\frac{\epsilon_1 \epsilon_2}{\epsilon_1 + \epsilon_2}} \quad (3.11)$$

where  $\beta = k_x$  is the wave vector in the propagating direction and  $k_0 = \omega/c$  is the wave vector of the propagating wave in vacuum; i.e. the wave vector of the photon that would excite this specific plasmon.

For metals, the simplest model to calculate the permittivity is given by the Drude model, where the electrons are considered to be free [18],

$$\epsilon(\omega) = \frac{\omega_p^2}{\omega(\omega + i\gamma)} \quad (3.12)$$

where  $\gamma$  is the damping parameter of the material. Using this expression, together with the dispersion relation given in Eq. 3.11, we can derive two of the most relevant properties of plasmons: the confinement factor that gives the ratio between the plasmon wavelength  $\lambda_{\text{SPP}}$  and the free space wavelength of the electromagnetic wave  $\lambda_0$ , and the propagation distance  $L_{\text{SPP}}$ , which gives the distance at which the field intensity is  $1/e$  of the initial. These are given by

$$\frac{\lambda_{\text{SPP}}}{\lambda_0} = \frac{2\pi}{\lambda_0} \frac{1}{\text{Re}[k_{\text{SPP}}]} \quad (3.13a)$$

$$L_{\text{SPP}} = \frac{1}{2\text{Im}[k_{\text{SPP}}]}, \quad (3.13b)$$

respectively [33]. The confinement factor is of great interest as it shows the confinement of the free space light into the plasmonic form. The larger the confinement, the larger the plasmonic effect, as the field intensity has a cubic dependence on this parameter. On the other hand, the propagation distance is also of extreme relevance as it is directly related to the plasmon lifetime and a long interaction time leads to stronger nonlinear effects, which could be applicable to current technologies. Therefore, the challenge lies on finding materials that would sustain surface plasmons with a large confinement property; in other words,  $\text{Re}[k_{\text{SPP}}] \gg 1$ , and long propagating distances; meaning,  $\text{Im}[k_{\text{SPP}}] \ll 1$ . In the case of metallic plasmons two main drawbacks are currently holding up the use of SPPs in commercialized devices:

- i.* The high plasmon confinement hinders the coupling between the incident free space light  $k_0$  and the plasmon  $k_p$ . This is due to the large wave vector mismatch that these have, as momentum conservation dictates that these should be equal.
- ii.* The typical lifetime of metallic plasmons is so short that the plasmon only propagates for a few cycles before it completely decays and this is a huge limitation in its applicability in new technologies; especially to quantum technology, where loss is extremely important and long interaction times are required.

## 3.2 Localized Surface Plasmons

In summary, we have just seen that SPPs are propagating, dispersive electromagnetic waves coupled to the electron plasma of a conductor at a dielectric interface. On the other hand, localized surface plasmons (LSP) are characterized by being non-propagating excitations of the conduction electrons of metallic nanostructures coupled to the incident electromagnetic field [56]. To understand the origin of LSPs and their optical response, we will analyze a small, homogeneous and isotropic sphere with a radius  $a$ , a dielectric function  $\epsilon(\omega)$ , and surrounded by an isotropic and non-absorbing medium with dielectric constant  $\epsilon_m$  (see Fig.

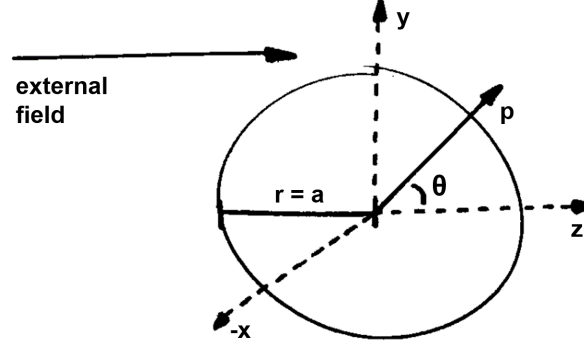


**Figure 3.2. Metallic sphere in a uniform electrostatic field.** We consider a homogeneous and isotropic sphere, with radius  $a$  and dielectric constant  $\epsilon(\omega)$ , in an isotropic and non-absorbing medium.

3.2). Assuming that the incident wavelength is smaller than the sphere,  $d \ll \lambda_0$ , we can use the quasi-static approximation, where the harmonic oscillation of the fields is considered to be time invariant in the entire particle, and we can consider it as an electrostatic field. The harmonic behaviour can be added later on, after the solutions are found.

Considering the external field to be of the form  $\mathbf{E} = E_0 \hat{z}$ , one can solve the Laplace equation,  $\nabla^2 \cdot \phi = 0$ , where  $E = -\nabla \cdot \phi$ , and find the electrical potential  $\phi$  inside and outside of the sphere to be

$$\phi_{\text{in}}(r) = -\frac{3\epsilon_m}{\epsilon + 2\epsilon_m} E_0 r \cos \theta \quad (3.14a)$$

$$\phi_{\text{out}}(r) = -E_0 r \cos \theta + \frac{\epsilon - \epsilon_m}{\epsilon + 2\epsilon_m} E_0 a^3 \frac{\cos \theta}{r^2} \quad (3.14b)$$

Interestingly,  $\phi_{\text{out}}(r)$  describes the superposition of the applied field and that of a dipole with origin at the center of the sphere. Thus, if we rewrite Eq. 3.18b as

$$\phi_{\text{out}}(r) = -E_0 r \cos \theta + \frac{\mathbf{p} \cdot \mathbf{r}}{4\pi\epsilon_0\epsilon_m r^3}, \quad (3.15)$$

we find the dipole moment  $\mathbf{p}$  to be

$$\mathbf{p} = 4\pi\epsilon_0\epsilon_m a^3 \frac{\epsilon - \epsilon_m}{\epsilon + 2\epsilon_m} E_0. \quad (3.16)$$

Furthermore, we can also find the polarizability  $\alpha$ , which is related to the dipole moment as  $p = \epsilon_0\epsilon_m\alpha E_0$  with

$$\alpha = 4\pi a^3 \frac{\epsilon - \epsilon_m}{\epsilon + 2\epsilon_m}. \quad (3.17)$$

From this expression we can conclude that the polarizability shows a resonance when  $|\epsilon + 2\epsilon_m|$  is minimum, which confirms the strong dependence of this resonance frequency on the dielectric constant of the environment: it red-shifts as  $\epsilon_m$  increases. The mode associated with

this resonance condition is the so-called dipole surface plasmon on a metal nanoparticle.

Without entering into too much detail, one of the consequences of resonantly exciting a plasmon in such a small particle is that this radiates electromagnetic fields. This radiation scatters the plane wave that excited the dipole in the first place. An additional consequence of this excitation that is more relevant to this work is that the optical scattering and absorption of such a sphere also depends on whether the sphere has a resonantly enhanced polarization  $\alpha$ . The corresponding scattering  $C_{\text{sca}}$  and absorption  $C_{\text{abs}}$  cross sections are

$$C_{\text{sca}} = \frac{k^4}{6\pi} |\alpha|^2 = \frac{8\pi}{3} k^4 a^6 \left| \frac{\epsilon - \epsilon_m}{\epsilon + 2\epsilon_m} \right|^2 \quad (3.18a)$$

$$C_{\text{abs}} = k \text{Im}[\alpha] = 4\pi k a^3 \text{Im} \left[ \frac{\epsilon - \epsilon_m}{\epsilon + 2\epsilon_m} \right] \quad (3.18b)$$

Here we clearly see that when  $a \ll \lambda_0$ , the scattering proportional to  $a^6$  dominates the absorption, which has an  $a^3$  dependence. This hinders the excitation of LSPs.

### 3.3 Graphene Surface Plasmons launched via metallic antennas

We have already mentioned that, although plasmons provide huge field confinements, there are two main drawbacks related to metallic plasmons that currently hinder their industrial application. These are the momentum mismatch between the free space wave vector  $k_0$  and the plasmon wave vector  $k_p$ , which makes it almost impossible to excite SPPs in a homogeneous metal surface, and their short lifetime, which limits their propagation to a few plasmon wavelengths.

As an alternative to metallic plasmons, in the last decade, graphene has been shown to sustain long lived plasmons that can be tuned actively via electrostatic gating. Lifetimes of  $\tau_p \sim 500$  fs at room temperature [94] and even  $\tau_p \sim 10$  ps at cryogenic temperatures [65] have already been observed. However, the momentum mismatch between the free space photons and graphene plasmons is as large as that found with metallic plasmons and so the excitation of graphene plasmons remains a challenge. One promising way around this problem is to use a metallic structure on top of the graphene sheet. When resonant light impinges on these structures, they behave like an optical dipole, which is capable of launching SPPs propagating through graphene.

To better understand this mechanism, we proceed to study one of the simplest systems [33]. As depicted in Fig. 3.3, we consider an infinitely long metallic stripe with width  $L$  placed on top of an infinite sheet of planar graphene. For the mathematical description we will consider the metal to cover  $|x| < L/2$  with the center at  $x = 0$  and assume that the metal is much

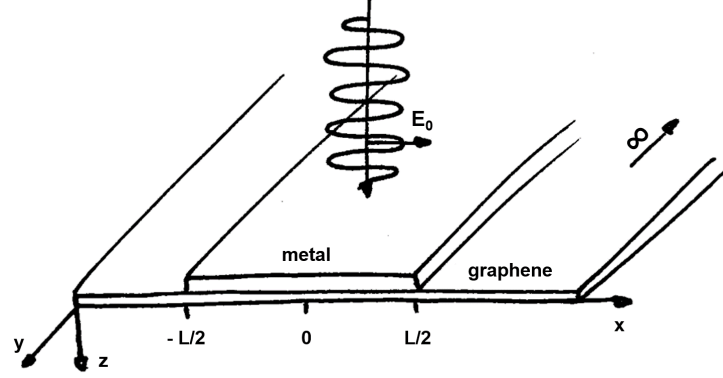


**Figure 3.3. Sketch of a metallic stripe on planar graphene.** Graphene is infinite in  $x$  and  $y$  directions and the metallic stripe has a width  $L$ , centered at  $x = 0$  and extends infinitely in the  $y$  direction. The incident electromagnetic wave  $\mathbf{E}$  propagates in the  $z$  direction and is polarized in the  $x$  direction.

thinner than the wavelength of the external field  $\mathbf{E}^{\text{ext}}$ , which means that we can consider it as a 2D structure. Furthermore, we will also assume that the conductivity of this strip is so high that it effectively behaves as a metal strip between two separated sheets of graphene; in other words, the graphene enclosed below the metal is negligible.

If there is a monochromatic electromagnetic wave polarized in the  $x$ -direction, propagating in the  $z$  direction through the metallic strip, this external field would be described as

$$E^{\text{ext}} = E_0 e^{i(k_z z - \omega t)} \quad (3.19)$$

where  $k_z = \sqrt{\epsilon}\omega/c$  is the wave vector in the propagation direction  $z$ , and  $\epsilon$  is the relative permittivity of the medium. Under these assumptions it is possible to write the linear response of the entire system as a current density that only varies in  $x$  and depends on both the metal and graphene conductivities,  $\sigma_m$  and  $\sigma_g$ , respectively. We should also note that the external field will induce another field  $E^{\text{ind}}$ , and that both should be considered in our study; that is,

$$E_x = E_x^{\text{ext}} + E_x^{\text{ind}}. \quad (3.20)$$

Due to the symmetry of the system, we only need to find the solutions of the electric field in the  $x$  and  $z$  directions and the magnetic field in the  $y$  direction; that is,  $\mathbf{E} = (E_x, 0, E_z)$  and  $\mathbf{H} = (0, H_y, 0)$ . There are some mathematical tricks and approximations that one needs in order to get the solutions, but these are not relevant in this thesis so we will just provide the solutions so that we can have a qualitative understanding of the behavior of the in-plane electric field at  $z = 0$  and analyze the effects that this external field has on the system (refer to [33], chapter 6 for full mathematical procedure). In the solutions we distinguish between

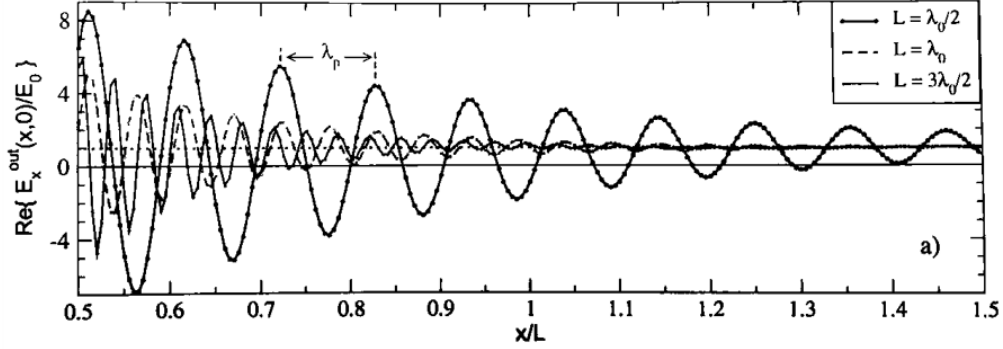


**Figure 3.4. Electric field outside the metal stripe.** As a result of the incident electromagnetic wave  $E^{\text{ext}}$ , there is a field originating on the edge of the metal and propagating away from it in the  $x$  direction. For  $L/\lambda_0/2$  the resonance condition is found, where the field strength is much stronger than with the non-resonant cases. Additionally, the field strength decreases as  $x$  increases and far away, there is no sign of plasmonic behaviour and only a homogenous field above zero can be observed. Image taken from [33], page 157.

the fields inside and outside the metallic stripe as

$$E_x^{\text{in}}(x, 0) = \sum_{n=0}^N A_n \cos\left(\frac{2n\pi x}{L}\right) \quad (3.21a)$$

$$E_x^{\text{out}}(x, 0) = \frac{1}{\zeta_0} E_0 + \frac{2\eta_\sigma}{\pi} \sum_{n=0}^N (-1)^n A_n \int_0^{\text{inf}} \frac{\cos(ux/L)}{\zeta_u} \frac{u \sin(u/2)}{u^2 - 4n^2\pi^2} du, \quad (3.21b)$$

where  $\eta_\sigma = \sigma_m/\sigma_g - 1$ ,  $u = qL$ ,  $A_n$  are the Fourier coefficients and  $\zeta_u$  is a function given by

$$\zeta_u = 1 - \frac{E_F}{\hbar\omega} \frac{2\alpha\Omega_L}{\hbar\omega + i\hbar\gamma} \sqrt{u^2 - a^2}, \quad (3.22)$$

where  $a = \sqrt{\epsilon}\hbar\omega/\Omega_L$  and  $\Omega_L = \hbar c/L$ .

Fig. 3.4 shows the result of Eq. 3.21b for different metal widths  $L$ , a constant Fermi energy, a largely conductive metal  $\sigma_m/\sigma_g \ll 1$  and a fixed incident wavelength. Here we can observe that there is a strong propagating field when  $L = \lambda_0/2$ , which corresponds to the excitation of a graphene SPP originating at the edge of the metal and propagating through the graphene, away from the metal. We can also directly find the plasmon wavelength  $\lambda_p$  and calculate the confinement ratio to be around 19, as  $\lambda_p \sim 0.052\lambda_0$ . Furthermore, we also notice that, as expected, the plasmonic field decreases as  $x$  gets larger. This is due to the Ohmic losses within the graphene. In fact, far away from the metal one can no longer distinguish the characteristic oscillations of the plasmon excitations and only the homogenous response of the system is present; namely,  $E_x^{\text{ext}}/E_0 \rightarrow \zeta_0^{-1} = 1$ . Thus we have shown that the momentum mismatch between the free space electromagnetic field and the plasmon can be overcome by metallic structures that provide a suitable platform for launching such SPPs in graphene.

In this chapter we have introduced the fundamentals of plasmonics and placed special emphasis to graphene surface plasmons, which will later appear both in our theoretical work in Section 7.1 and experimental work in Section 7.3. The last section about launching graphene surface plasmons via metallic antennas is particularly interesting because this effect is the reason of the huge nonlinear optical enhancement that we have observed in our graphene devices.



## Chapter 4

# Fundamentals of Graphene

Carbon is all over the place. From simple rocks to sophisticated diamonds, passing through uncountable intricate compounds. It constitutes the 15th most abundant element on Earth and the 4th in the universe, right after hydrogen, helium and oxygen. It is thus not surprising the curiosity that humans have shown towards this element since early times. Leaving aside the vast variety of heteronuclear composites that nature displays, this brief introduction will only focus on homonuclear carbon compounds, also known as carbon allotropes.

The first carbon allotrope ever known was graphite, which happens to be the most stable under standard conditions. Although it was already used in the 4th century BC, it was not until 1789 that geologist A. Werner gave this material its current name, which came from its use in graphical purposes such as, painting, marking or writing. As shown in Fig. 4.1a, graphite is formed by layers where the atoms are arranged in a hexagonal structure; that is, graphene. These layers are weakly bonded to each other by van der Waals forces and this is why graphite leaves a trace when pressed against another harder material like paper.

Fullerene is another example of a carbon allotrope [50]. This consists of 60 carbon atoms forming a hollow sphere, where the individual atoms are arranged forming pentagons and hexagons, just like a soccer ball (see Fig. 4.1b). We should mention that there are other numbers of atoms and shapes that are also known as fullerenes, but the most known one is the  $C_{60}$ , also known as buckminsterfullerene or bucky ball. This name was given in 1985 as a homage to the American architect Buckminster Fuller, as his designs resemble those of the fullerenes.

A few years later, in 1991, single-walled carbon nanotubes (CNTs) were discovered [41, 7]. As shown in Fig. 4.1c, These are rolled up graphene sheets with a cylindrical structure of a few nanometer diameter, which makes them effectively two dimensional. Depending on the edges of the original graphene sheet that leads to the nanotube, we can distinguish between zig-zag and armchair configurations. This characteristic, together with the angle at which this graphene sheet is rolled (chirality), CNTs can be manufactured to have very different electrical properties: from conducting to semiconducting.

Finally, in 2004, the long awaited graphene was isolated in a laboratory [67]. It happened at the Manchester University thanks to the simple method known as the *scotch tape method* developed by K. Novoselov and A. Geim, who later won the Nobel prize in 2010. This original method consists of literally using scotch tape to tap on a bulk piece of graphite and looking for

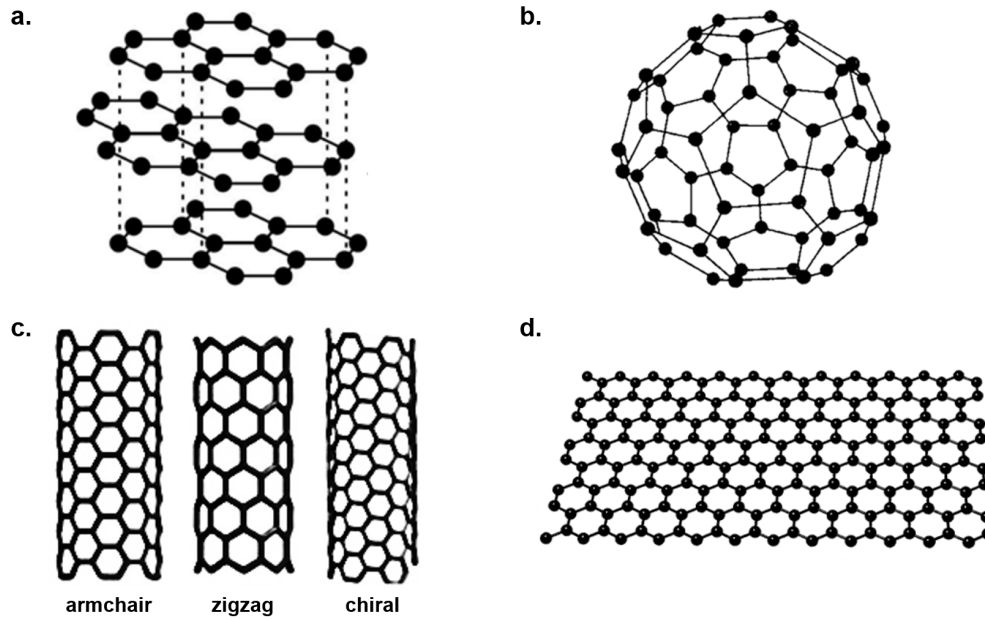


**Figure 4.1. Carbon allotropes.** **a.** Graphite. Graphene layers stick to each other via Van der Waals forces to form macroscopic size stacks. **b.** Buckminsterfullerene or bucky ball. 60 carbon atoms form a mesh of pentagons and hexagons and acquire a stable hollow sphere. **c.** Single-walled carbon nanotubes. Graphene sheets are rolled up to form cylinders with different diameters in the nanometer scale. Depending on the edges of the initial graphene and the chirality at which this is rolled up, its electronic properties can be tuned. **d.** Graphene. Carbon atoms form hexagons to build a stable 2D structure where electrons can hop from atom to atom, leading to extraordinary electronic mobility.

single-layer graphene areas on the tape. Technically, this is known as mechanical exfoliation and, although it is a tedious and nondeterministic method, it is still the method that provides best quality graphene today. This is because the exfoliated flakes are single-domain and this ensures great electron mobility, leading to huge conductivity and other optical properties that derive from it. However, this method is limited to graphene samples in the order of few tens of micrometers. For larger samples and industrial applications, the so-called chemical vapor deposition (CVD) method is used, which allows one to cover areas on the order of tens of centimeters with a monolayer [89].

## 4.1 Electronic properties of graphene

The electronic configuration of carbon is

$$[C] = 1s^2 2s^2 2p^2 \quad (4.1)$$

where the last three electrons ( $2s, 2p_x, 2p_y$ ) combine to give a  $sp^2$  hybridization and an electron is left free [33]. Those electrons in the hybrid orbitals form  $\sigma$  bonds with the neighboring

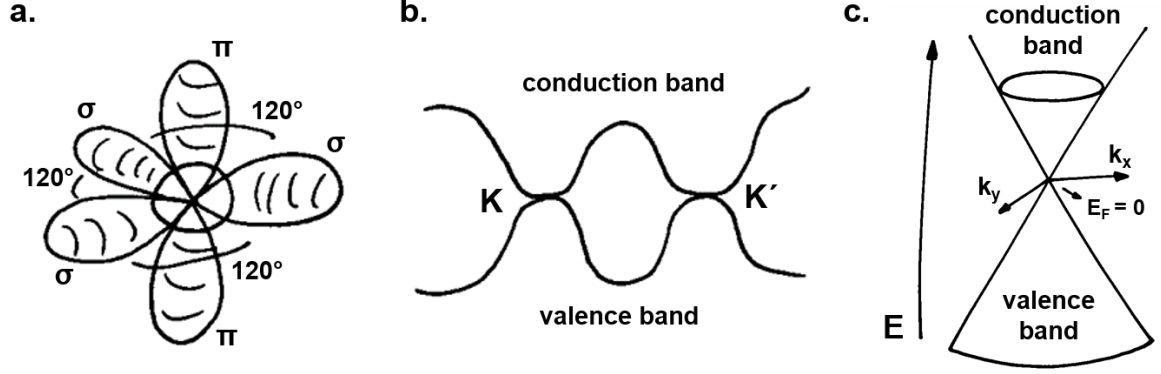


**Figure 4.2. Graphene's electronic properties.** **a.** Sketch of the orbitals of a carbon atom. The  $sp^2$  hybrid orbitals lie on the  $x - y$  plane with  $120^\circ$  separation between them. These have strong  $\sigma$  bonds with the neighboring atoms. The  $p_z$  orbital extends along the  $z$  axis, with an unpaired electron that can create weak  $\pi$  bonds. **b.** Valence and conduction bands of graphene. These are completely symmetric and intersect at points  $\mathbf{K}$  and  $\mathbf{K}'$ , where  $E_F = 0$ . **c.** For relatively low energies ( $|E_E| < 2$  eV) the dispersion relation of graphene is linear and has the shape of two cones known as the Dirac cones. This is due to its similarity to the Dirac equation for massless fermions. At the intersection of the cones, known as the Dirac point,  $E_F = 0$ .

carbon atoms, keeping a  $120^\circ$  separation in between the arms (see Fig. 4.2a). These strong bonds are responsible for the extraordinary mechanical properties of graphene. The fourth orbital ( $2p_z$ ) is perpendicular to the plane defined by the  $sp^2$  orbitals and it creates  $\pi$  bonds between the graphene layers, forming multilayer graphene or even graphite. In the case of monolayer graphene, these unpaired electrons can freely hop from one  $\pi$  orbital to another, leading to the remarkable electronic and optical properties of graphene.

Mathematically, graphene can be described by two intersecting triangular Bravais sublattices, with lattice vectors

$$\mathbf{a}_1 = \frac{a_0}{2}(3, \sqrt{3}) \quad \mathbf{a}_2 = \frac{a_0}{2}(3, -\sqrt{3}) \quad (4.2)$$

where  $a_0 = 1.421\text{\AA}$  is the distance between two neighboring carbon atoms (see Fig. 4.3a). The corresponding reciprocal space is defined by the vectors

$$\mathbf{b}_1 = \frac{2\pi}{3a_0}(1, \sqrt{3}) \quad \mathbf{b}_2 = \frac{2\pi}{3a_0}(1, -\sqrt{3}) \quad (4.3)$$

which define the first Brillouin zone (see Fig. 4.3b).

The tight binding model considering only  $\pi$  electron hopping between the nearest neighbors gives the following form of the electronic bands in the reciprocal space:

$$E_k = \pm t \sqrt{1 + 4 \cos^2 \left( \frac{\sqrt{3}a_0}{2} k_y \right) + 4 \cos \left( \frac{\sqrt{3}a_0}{2} k_y \right) \cos \left( \frac{3a_0}{2} k_x \right)} \quad (4.4)$$

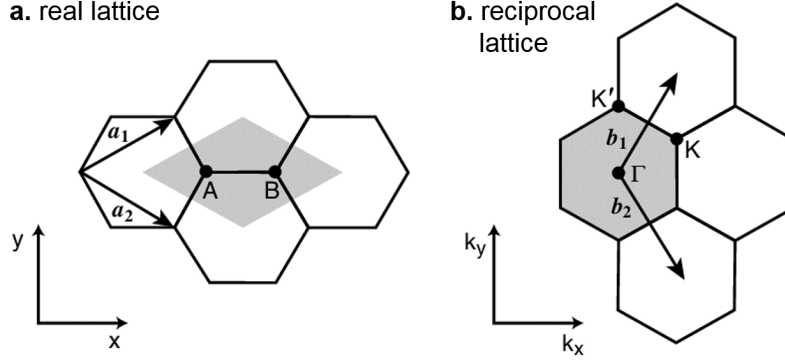


**Figure 4.3. Real and reciprocal lattices of graphene.** **a.** In the real lattice, the unit cell is determined by the shaded area, where A and B are two atoms separated by the minimum distance  $a_0 = 1.421\text{\AA}$ .  $a_1$  and  $a_2$  are the lattice vectors of the Bravais sublattice describing the honeycomb structure of graphene. **b.** In the reciprocal lattice, the first Brillouin zone is defined by the shaded area with the center at  $\Gamma$ .  $b_1$  and  $b_2$  are the basis vectors of the reciprocal lattice. Image taken from[91].

where  $t = 2.8\text{ eV}$  is the hopping energy between neighboring orbitals. In Fig. 4.2b we have plotted the valence ( $E_k < 0$ ) and conduction ( $E_k > 0$ ) bands and find two points at which they intersect:

$$\mathbf{K} = \frac{2\pi}{3a_0} \left( 1, \frac{1}{\sqrt{3}} \right) \quad \mathbf{K}' = \frac{2\pi}{3a_0} \left( 1, -\frac{1}{\sqrt{3}} \right) \quad (4.5)$$

where  $E_K = E_{K'} = 0$ . We can now shift the wave vector coordinates to have the origin at this  $K$  point; that is,  $\mathbf{k} = \mathbf{K} + \mathbf{q}$ , where  $\mathbf{q}$  is the wave vector with respect to this new origin at point  $K$ . The characteristic linear dispersion relation of graphene is then given by

$$E_q = \hbar v_F |\mathbf{q}| \quad (4.6)$$

where  $v_F = \frac{3ta_0}{2\hbar} \sim \frac{c}{300} \sim 10^6\text{ m/s}$  is the Fermi velocity of the electrons [82]. If we have a closer look at the region around these singular points, we distinguish a conical shape, known as the Dirac cone, as this is similar to that given by the Dirac equation for massless fermions. Thus, we can conclude that the free electrons in graphene behave like massless particles.

## 4.2 Optical properties of graphene

Apart from the electronic properties, the linear dispersion relation of graphene also leads to two very characteristic optical features. On one hand, when graphene is undoped,  $E_F = 0$ , it has a constant absorption coefficient  $A = \pi\alpha \sim 2.3\%$  that is independent of the incident wavelength [29]. This is explained by the symmetry between the valence and the conduction bands, and the fact that, since the conduction band is empty, any electron excitation is allowed, regardless of the photon energy, as long as the linearity of the dispersion relation

holds. On the other hand, due to this linear dispersion, the density of states in graphene is very low and this leads to major changes in the Fermi energy even with weak electronic doping. To be precise, the dependence of the Fermi energy on the density of injected carriers  $n$  is given by

$$E_F = \hbar v_F \sqrt{\pi n}. \quad (4.7)$$

In practice, this electrical doping is carried out by an external constant electric field  $\mathbf{E}$  applied across the graphene sheet. The resulting carrier density is the  $n = -|\mathbf{E}|/4\pi e$ . It should be mentioned that the carriers could either be electrons in the conduction band or holes in the valence band, depending on the polarity of the applied field. As expected, shifting the Fermi energy brings changes to the optoelectrical response of graphene. This can be easily described by the local random phase approximation model, in which the conductivity is given by:

$$\sigma(\omega) = \frac{-e^2}{\pi \hbar^2} \frac{i}{\omega + i\gamma} \int_{-\infty}^{\infty} \left( |E| \frac{\delta f_E}{\delta E} + \frac{E/|E|}{1 - \left(\frac{2E}{\hbar(\omega + i\gamma)}\right)^2} f_E \right) dE, \quad (4.8)$$

where

$$f_E = \frac{1}{1 + e^{(E - E_F)/k_B T}} \quad (4.9)$$

is the electron distribution with energy  $E$  [26]. In this expression for the conductivity we distinguish two terms in the integral. The first one corresponds to intraband transitions, where electrons are excited within the band, and the second term corresponds to the interband transitions, where electrons are excited from one band to another. It is worth mentioning that by ignoring the second term and taking  $T \rightarrow 0$  this equation reduces to the conductivity given by the Drude model [19, 34], where electrons are treated as classical particles bouncing off of the nuclei in the material,

$$\sigma(\omega) = \frac{e^2}{\pi \hbar^2} \frac{i|E|}{\omega + i\gamma}. \quad (4.10)$$

So as to better explain the optical properties of graphene and understand the difference between intra- and interband transitions, we will take a step back and focus on the optical dispersion relation of graphene shown in Fig. 4.4a. In this sketch we have chosen some arbitrary Fermi energy  $E_F = 0.4 \text{ eV}$ . At this doping level, the valence band is completely filled with electrons and the conduction band is slightly filled. The transitions occurring within the same band are known as intraband transitions, and those where an electron from the valence band fills a hole in the conduction band are called interband transitions. In this example, intraband transitions are only allowed in the conduction band, as those in the valence band are Pauli blocked because the band is already full with electrons. It is worth mentioning that transitions can only occur within states on the surface of the cones.

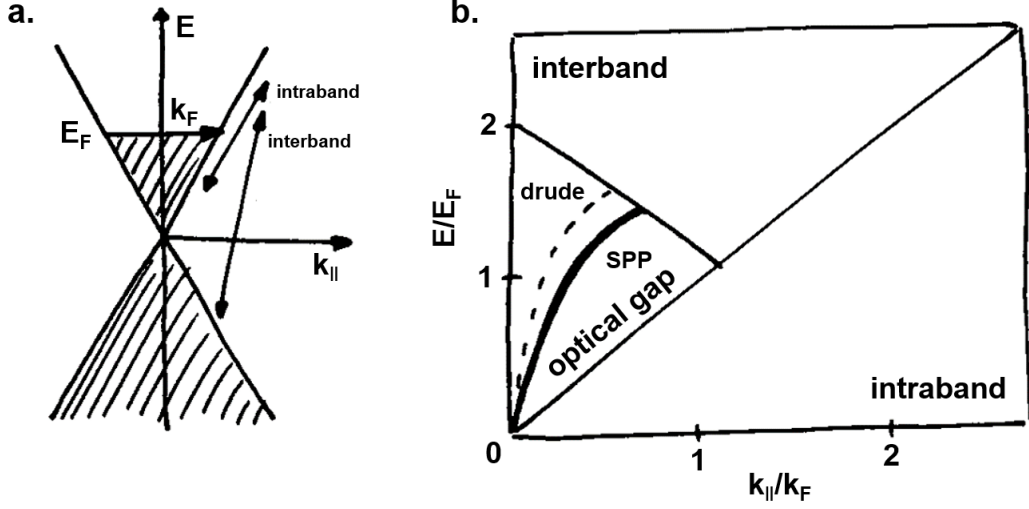


**Figure 4.4. Dispersion relation of graphene** **a.** Sketch of the optical dispersion relation of graphene and **b.** density plot summarizing all the allowed transitions in graphene, including intraband and interband transitions, and excitations of SPPs. This is calculated via the random-phase approximation (RPA) model for a free standing graphene ( $\epsilon_1 = \epsilon_2 = 1$ ) with  $E_F = 0.4$  eV and  $\mu = 10^4$  cm<sup>2</sup>/Vs. Image taken from [26], page 37.

Similar to how we derived the Fresnel coefficients (Eq. 2.15) at the interface between two different materials, one can derive the reflection coefficient of a  $p$ -polarized (TM) electromagnetic wave impinging on a layer of graphene sandwiched between two materials with  $\epsilon_1$  and  $\epsilon_2$ . This is given by,

$$r_p = \frac{\epsilon_2 k_{1\perp} - \epsilon_1 k_{2\perp} + 4\pi\sigma/\omega k_{1\perp} k_{2\perp}}{\epsilon_2 k_{1\perp} + \epsilon_1 k_{2\perp} + 4\pi\sigma/\omega k_{1\perp} k_{2\perp}} \quad (4.11)$$

The imaginary part of this reflection coefficient corresponds to absorption of the incident light, which describes the states that can be excited; that is, the density of states. In Fig. 4.4b, we show  $Im\{r_p\}$  as a function of the energy and momentum of the photon for  $E_F = 0.4$  eV and  $\mu = 10^4$  cm<sup>2</sup>/Vs. In this figure, the light line lies almost on the vertical axis because of the steep dispersion relation of light,  $\omega = ck$ , with  $c = 3 \cdot 10^8$  m/s. Here we distinguish three main possible transitions. In the bottom right corner we have the intraband transitions that occur within the conduction band. Note that for  $k_{\parallel} = 0$  no intraband transition can occur because the only allowed transitions are those within the surface of the cone. In the top of the figure interband transitions are allowed; those from the valence band to the conduction band. Finally, there is an optical gap in the left bottom corner. This area is limited by the conditions  $k_{\parallel} < k_F$  and  $\hbar\omega < 2E_F$ , where neither intraband nor interband transitions can occur; in other words, it is impossible to absorb the photon and conserve both energy and momentum. However, the thick line that crosses the optical gap corresponds to momenta and energies for which SPPs can be excited.

The dispersion relation of the  $p$ -polarized graphene SPPs can then be obtained through the pole of  $r_p$ , which satisfies the equation

$$\frac{\epsilon_1}{\sqrt{k_{\text{spp}}^2 - \epsilon_1 k^2}} + \frac{\epsilon_2}{\sqrt{k_{\text{spp}}^2 - \epsilon_2 k^2}} = -\frac{4\pi i \sigma}{\omega}, \quad (4.12)$$

where  $k_{\text{spp}}$  is the in-plane component of the plasmon wave vector.

In this chapter we have summarized the timeline of the discovery of the different carbon allotropes, from the most ancient graphite to the latest graphene. We have then described the electronic properties of graphene, which lead to its optical properties. Apart from the constant linear absorption that graphene's continuous band structure provides, the dispersion relation of graphene, related to the conductivity given in Eq. 4.8, plays a special role in this work: we experimentally tune the Fermi energy to enable transitions that would otherwise be Pauli-blocked. It should be mentioned that the nonlinear optical properties of graphene are not included in this chapter because it is a very involved calculation that is beyond the scope of this thesis [60, 61, 11, 12, 80].



## Chapter 5

# Fundamentals of Quantum Computing

For decades, scientists developed new theories based on classical mechanics that failed to explain the observed effects when atoms and photons interacted with each other. Among others, these include the solution of Max Planck in 1900 to the black body radiation problem or the photoelectric effect first explained by Albert Einstein in 1905. Finally, in the mid-1920s, Erwin Schrödinger, Werner Heisenberg, Max Born and other renowned scientists developed the so-called Quantum Theory, which aims to describe the behavior of the smallest things in nature, all the way down to the atomic and subatomic scale. In this theory, every particle is associated to a wave function, which can be used to predict the probabilities of finding the particle in a certain state.

In the subsequent years, scientific discoveries kept confirming the accuracy of this counter-intuitive quantum theory and more and more phenomenology was explained on this basis. However, as computers were becoming the key point in research, and more complex quantum systems were being studied, in 1982, Richard Feynmann wondered how one could simulate the probabilistic behaviour of nature based on quantum mechanics with a classical non-probabilistic computer [25].

So as to understand why this was a major concern and to understand the current push to build a quantum computer, there are a few concepts that we first need to introduce [1, 66, 75].

### 5.1 Qubits and entanglement

In quantum mechanics any quantum system can be in a state known as a quantum state [66]. The simplest case is that of a two-level system, known as qubit, which can be in two different pure states; say 0 or 1. The difference between a bit in a classical computer and a qubit in a quantum computer is that the latter can also be in any arbitrary superposition of these two pure states; namely,

$$|\psi\rangle = \alpha |0\rangle + \beta |1\rangle \quad (5.1)$$

where  $|0\rangle = \begin{pmatrix} 1 \\ 0 \end{pmatrix}$  and  $|1\rangle = \begin{pmatrix} 0 \\ 1 \end{pmatrix}$  are normalized and orthogonal states that make up a basis set, and  $\alpha$  and  $\beta$  are complex numbers that, due to conservation of probability, obey  $|\alpha|^2 + |\beta|^2 = 1$ .

Generally speaking, this state  $|\psi\rangle$  can be represented as a vector in the Bloch sphere with unit length as

$$|\psi\rangle = \cos(\theta/2) + e^{i\phi} \sin(\theta/2) \quad (5.2)$$

If we now expand this single-qubit example to a separable  $n$ -qubit system, the pure state would be defined as the tensor product of the individual quantum states as

$$|\psi_{tot}\rangle_{sep} = |\psi_1\rangle \otimes |\psi_2\rangle \otimes |\psi_1\rangle \otimes \cdots \otimes |\psi_n\rangle \quad (5.3)$$

where

$$|\psi_i\rangle = \alpha_i |0\rangle + \beta_i |1\rangle \quad (5.4)$$

This means that, classically, we would need  $2n$  amplitude values to describe the system. However, if the  $n$ -qubit system is entangled or nonseparable, this state could no longer be written as the tensor product of the individual  $n$ -qubits. Instead, we would have to write the state as

$$|\psi_{tot}\rangle_{nonsep} = \sum_{x \in \{0,1\}^n} \alpha_x |x\rangle \quad (5.5)$$

where  $\alpha_x$  is a vector with all components of the form  $\{\alpha_{0000\dots 0}, \alpha_{0000\dots 1}\}$ , the length of which scales as  $2^n$ . This means that, classically, describing this system requires  $2^n$  amplitudes, which becomes unfeasible very rapidly. To give a more intuitive idea of this magnitude, already for  $n = 300$ , the size of  $\alpha_x$  is larger than the number of atoms in the universe. This is exactly part of where the speed up of quantum computers comes from when compared to classical computers. We should also emphasize that, if resources were unlimited, classical computers would also be able to simulate quantum systems. However, in practice, the amount of required resources limits the feasibility to a very little amount of quantum bits.

Apart from the separable and nonseparable (entangled) states, we also distinguish mixed states, which can be interpreted as probability distributions over quantum superpositions. Mathematically, we represent these states via the density matrix given by

$$\rho_i = \sum_i p_i |\psi_k\rangle \langle \psi_k| \quad (5.6)$$

where  $p_k$  is the probability corresponding to the single pure state  $|\psi_k\rangle$ . So as to ensure that the density operator is physical, there are three conditions that this needs to fulfill:

- $\rho$  needs to be square.
- $\rho$  needs to be Hermitian; that is,  $\rho = \rho^\dagger$ .
- $\rho$  must be non-negative, meaning that it has positive eigenvalues; that is,  $Tr(\rho^2) = 1$  for pure states and  $Tr(\rho^2) < 1$  for mixed states.

The diagonal terms  $\rho_{ii} = \langle i|\rho|i\rangle$  known as the *population*, indicate the probability of collapsing the system in the state  $|i\rangle$  after measuring the observable with eigenstates  $\{|i\rangle\}$ . The off-diagonal terms  $\rho_{ij} = \langle j|\rho|i\rangle$  are known as the *coherences* and they assess the interference between the states  $|i\rangle$  and  $|j\rangle$ .

The simplest maximally entangled states are those given by two particles. These are the so-called Bell states, which we introduce here, as they will appear later in the work presented in Section 7.1,

$$|\phi^\pm\rangle = \frac{1}{\sqrt{2}} (|0\rangle_1 |0\rangle_2 \pm |1\rangle_1 |1\rangle_2) \quad (5.7a)$$

$$|\psi^\pm\rangle = \frac{1}{\sqrt{2}} (|0\rangle_1 |1\rangle_2 \pm |1\rangle_1 |0\rangle_2) \quad (5.7b)$$

where  $|0\rangle_1 |0\rangle_2 = |0\rangle_1 \otimes |0\rangle_2$  represents the first and the second particle in state  $|0\rangle$ . For simplicity, here we will also write it as  $|00\rangle$ .

## 5.2 Quantum logic gates

Classical computers consist of wires that carry information around the circuit and connect logic gates together. In a similar way, quantum computers can also be described as a circuit, where qubits are transmitted through a set of quantum logic gates. Although there are some differences, there is an analogous quantum logic gate for each classical logic operation. Additionally, due to the special properties that qubits have, such as superposition, there are also other types of quantum gates that have no classical analogue.

The most elementary single-qubit gates are the  $2 \times 2$  Pauli matrices ( $\sigma_x, \sigma_y, \sigma_z$ ) and the identity operator  $\mathbb{I}$ :

$$\sigma_x = \begin{pmatrix} 0 & 1 \\ 1 & 0 \end{pmatrix} \quad \sigma_y = \begin{pmatrix} 0 & -i \\ i & 0 \end{pmatrix} \quad \sigma_z = \begin{pmatrix} 1 & 0 \\ 0 & -1 \end{pmatrix} \quad \mathbb{I} = \begin{pmatrix} 1 & 0 \\ 0 & 1 \end{pmatrix} \quad (5.8)$$

Due to the way in which these alter the state of the qubit,  $\sigma_x$  and  $\sigma_z$  are known as the *bit flip* and *phase* gates, respectively. Another very relevant gate in quantum computing is the Hadamard gate (H), which maps the  $\{|0\rangle, |1\rangle\}$  basis to the  $\{|+\rangle, |-\rangle\}$  basis, where

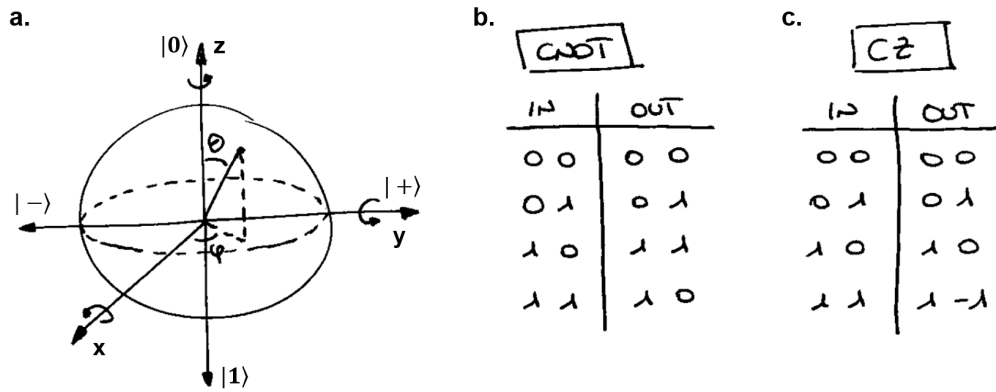


**Figure 5.1.** a. Every point in the Bloch sphere represents a quantum state. The computational basis,  $|0\rangle$  and  $|1\rangle$ , is defined along the z-axis, while the diagonal basis,  $|+\rangle$  and  $|-\rangle$ , lies on the x-axis. b. CNOT and c. CZ truth tables. These gates flip or change the phase of a target qubit if the control qubit is 1.

$|+\rangle = 1/\sqrt{2}(|0\rangle + |1\rangle)$  and  $|-\rangle = 1/\sqrt{2}(|0\rangle - |1\rangle)$ . In the matrix form this is written as

$$H = \frac{1}{\sqrt{2}}(\sigma_x + \sigma_z) = \frac{1}{\sqrt{2}} \begin{pmatrix} 1 & 1 \\ 1 & -1 \end{pmatrix} \quad (5.9)$$

Additionally, there are also rotation gates,  $R_x(\theta) = e^{-i\frac{\theta}{2}\sigma_x}$ ,  $R_y(\delta) = e^{-i\frac{\delta}{2}\sigma_y}$ ,  $R_z(\delta) = e^{-i\frac{\delta}{2}\sigma_z}$ , where the qubit is rotated around the  $x$ ,  $y$  and  $z$  axis in the Bloch sphere, respectively (see Fig. 5.1a).

Another set of very important gates in quantum circuits are the two-qubit gates, as they create superposition and entanglement between different qubits. The most frequently used ones are the controlled-NOT (CNOT) and the controlled-Z (CZ) gates (see truth tables in Fig. 5.1b and c), where the target qubit gets flipped or acquires a phase depending on the state of the control qubit. In the computational basis  $|00\rangle, |01\rangle, |10\rangle, |11\rangle$  these are given by

$$CNOT = \begin{pmatrix} 1 & 0 & 0 & 0 \\ 0 & 1 & 0 & 0 \\ 0 & 0 & 0 & 1 \\ 0 & 0 & 1 & 0 \end{pmatrix} \quad CZ = \begin{pmatrix} 1 & 0 & 0 & 0 \\ 0 & 1 & 0 & 0 \\ 0 & 0 & 1 & 0 \\ 0 & 0 & 0 & -1 \end{pmatrix} \quad (5.10)$$

Note that in quantum mechanics, in general, and hence also in quantum computation, matrix

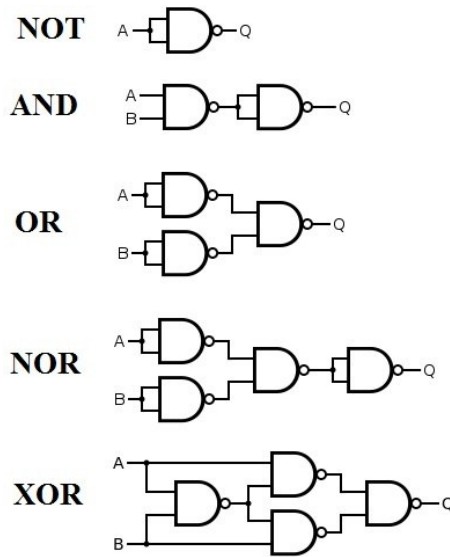


Figure 5.2. Logic gates built from the universal NAND gate.

operations have to be hermitian ( $A^\dagger = A$ ) to ensure that the eigenvalues are real and they need to be unitary ( $U^\dagger U = \mathbb{I}$ ) to ensure that the operation keeps the norm (energy conservation).

### 5.2.1 Universal quantum gates

In classical computation a logic gate or set of logic gates is known as *universal* if connecting together enough gates from this set one can compute any boolean function; i.e. if one can implement any computation by only using these set of gates. One of the most common example is the NAND gate, from which one can easily build most of the common gates; such as, NOT, AND, OR, NOR or XOR (see Fig. 5.2). On the other hand, although it might not be intuitive, sets like  $\{AND, OR\}$  or  $\{NOT, XOR\}$  are not universal.

Similar in quantum computation, but now the gates need to implement an arbitrary operator. There are uncountable permutations by which one could find a universal set of gates but, although not always sufficient, there are certain necessary conditions that these sets need to fulfill [1]

- The gate set should be able to create interference or superposition.
- The gate set should be able to create entanglement.
- The gate set should contain both real and imaginary gates.

Although there are many gate combinations that lead to a universal set of quantum gates, the most well-known sets in quantum computation are centered around the CNOT gate; such as,

$$\{CNOT, H, S, T\}$$

where H is the Hadamard gate given in eq. 5.9, S is the so-called phase gate or Z90 gate, as it represents a  $90^\circ$  rotation around the  $z$ -axis and T is half of a phase gate; that is,  $S = T^2$ . Another relevant universal set of gates is given by the Toffoli and Hadamard gates. The former is also known as the CCNOT gate as it acts as the CNOT gate but conditional on two control qubits. Finally, and relevant to this work, we should point out that the SWAP<sup>1/2</sup> gate together with single-qubit gates also forms a universal set of gates. This is due to the fact that, as shown in Fig. 5.3b, one can implement a CNOT gate using single-qubit rotations ( $R_y(\theta), R_z(\theta)$ ), the Pauli Z gate ( $\sigma_z$ ) and two SWAP<sup>1/2</sup> gates ( $1/2$ ).

### 5.3 Square-root of SWAP gate

Despite the nonlinear nature of logic operations, it is possible to implement any quantum computation based on linear optical elements [48]. Several approaches have been experimentally demonstrated [74, 72, 68, 83, 31, 101, 73], including the controlled-NOT (CNOT) gate, which is considered to be the ultimate universal quantum gate in photonic quantum computing. However, these linear devices are inherently probabilistic, which conditions their fidelity and limits their scalability. It is possible to circumvent this probabilistic nature and increase the success rate of such linear devices by including a large number of entangled ancilla photons and using high-efficiency detection systems, but scalability remains a problem.

An example of such an implementation is the one developed by Pittman, *et al.* [72], where one photon of an entangled Bell pair interacts, via a polarizing beam splitter, with the control qubit and the other one with the target qubit (see Fig. 5.3a). A successful CNOT operation will occur if only one photon is detected in each of the polarization-sensitive detectors, which happens with 25% probability. Thus, such a gate is considered to fail when more than one photon is found in the same optical mode. Our group has also recently experimentally demonstrated the implementation of such a gate on a laser-written waveguide [99]. To suppress such events, Franson, *et al.* [27] suggested using the Zeno effect to prevent the system from evolving into failure outcomes. Although they claim that this method could directly be applied to the original CNOT gate, they propose implementing the Zeno effect on a square-root of SWAP gate (SWAP<sup>1/2</sup>), which, together with single-qubit operations, completes a universal set of quantum gates.

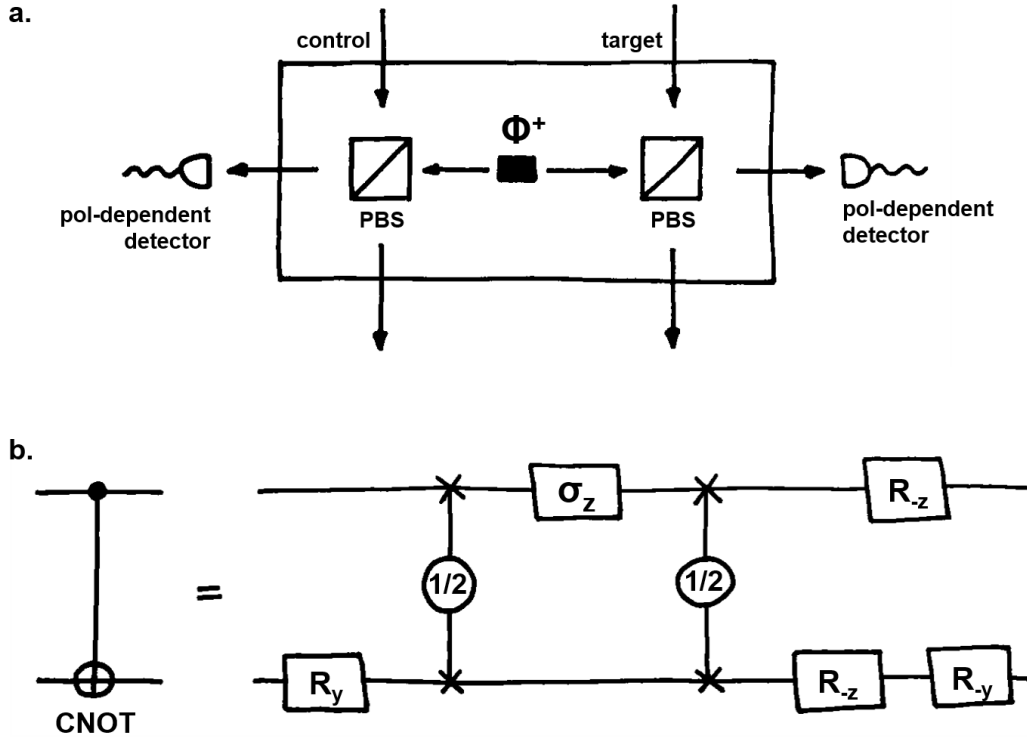


**Figure 5.3. CNOT gate.** **a.** Implementation of the CNOT gate proposed by Pittman, *et al.* [72], where the gate succeeds when a single photon is detected on each polarization-sensitive detector. **b.** Quantum circuit of a CNOT gate operation with single-qubit  $\pi/2$  rotations ( $R_y$ ,  $R_z$ ), two SWAP<sup>1/2</sup> gates (1/2) and a Pauli z operator ( $\sigma_z$ ).

Experimentally, the SWAP<sup>1/2</sup> gate can easily be implemented on a bulk optical beam splitter. However, as explained in Section 5.4, for the Zeno effect to take place, the observation (or loss channel in this case) needs to be applied in a continuous manner. To be precise, Franson, *et al.* proposed building a SWAP<sup>1/2</sup> gate on a directional coupler (DC) embedded in single atoms that are transparent to single photons but show a strong two-photon absorption (see Fig. 5.4a). The idea of the strong two-plasmon absorption versus single-photon transparency is explained by the energy level diagrams shown in Fig. 5.4b. Assume a three level system, equally separated by energy  $\hbar\omega$ . If the incident photons are resonant, both single- and two-photon states can be absorbed. However, if the second level is slightly shifted, single photons are no longer resonant to the transitions but two photons can be simultaneously absorbed, as energy is conserved.

This was the original idea from which we developed the work presented in Section 7.1, where instead of using single-atoms, we propose taking advantage of graphene's strong nonlinearity to achieve strong two-plasmon absorption without requiring any vacuum or cryogenic technology.

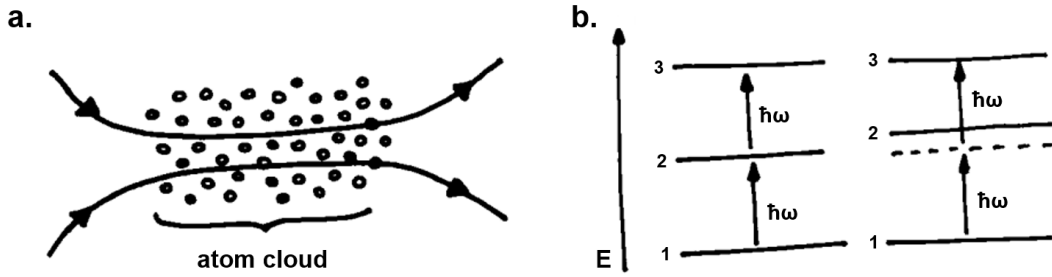


**Figure 5.4.**  $\text{SWAP}^{1/2}$  gate with a directional coupler and atoms. **a.** The waveguides of the directional coupler are surrounded by an atom cloud that shows single-photon transparency and strong two-photon absorption. **b.** Energy-level diagram of a three-level atom. *Left:* If the energy difference between the energy levels is the same, both single- and two-photon states can be absorbed. *Right:* However, if the energy of the second level is shifted, a single photon is no longer resonant but two photons can still be absorbed, as energy conservation is obeyed.

### 5.3.1 Optical qubit encoding

We have seen that, in theory, quantum computation can be described in a binary basis (0 and 1) and all its possible superpositions. We will now study how this binary basis can be implemented when the quantum information is carried by single photons.

The first and most intuitive option is to consider photons as particles in which information is encoded using some bipartite degree of freedom. Polarization (H, V) and spatial degree of freedom (path 1, path 2) are two of the most common degrees, which are easily interchangeable using a polarization beam-splitter. Additionally, there are other degrees of freedom that one could use; such as, temporal encoding (early, late) or frequency encoding (blue, red). Note that in all these cases, the photons have to be completely identical except for the degree of freedom used for encoding the information. For example, in the case of polarization encoding, the spatio-temporal and spectral state of the photons must be identical, and only the polarization can be different. This kind of encoding requires two optical modes per particle and we refer to it as dual-rail encoding [48].

An alternative to the dual-rail encoding is the single-rail encoding [76]. In this case the field mode is considered to be the carrier and the information is encoded in the different field states that this can acquire. A straightforward example is the basis formed by two Fock states. The most common one is given by the vacuum to be logic  $|0\rangle$  and the presence of a single photon to be logic  $|1\rangle$ .

Although there are many distinctions between these two types of encoding, there are two major differences that are most relevant: the evolution of the information carriers and the practical implementation of quantum computation. As for the evolution, in the case of dual-rail encoding, the qubit is in a stationary state; that is, the polarization does not change as the photon propagates. However, in the single-rail encoding, the optical modes correspond

to energy states and these experience a phase evolution as the mode propagates. Therefore, a co-propagating classical mode is needed as a phase reference [76]. With regard to the implementation, in the dual-rail encoding, single-qubit operations do not pose any challenge while non-trivial two-qubit gates are difficult and probabilistic. On the contrary, in the case of single-rail encodings, deterministic two-qubit gates are relatively easy, while single-qubit gates are difficult and probabilistic [95]. Nonetheless, for two-qubit gates, both encodings fail when two-photons are found in the same optical mode.

We have previously claimed that quantum logic operations are inherently nonlinear but mentioned that Knill, *et al.* [48] developed the so-called linear optical quantum computing (LOQC) approach in which only linear elements are required to perform universal quantum computing. However, this is not entirely true, as the detectors, together with postselection represent a nonlinear process [16]. When using a single-photon avalanche photodiode, for example, the nonlinearity is inherent in the exponential dependence of the measured electrical voltage on the number of excited photons [20]. In fact, both single- and dual-rail encodings require some sort of nonlinear process to verify that the operation has been successful. In the case of the dual-rail encoding, one does not require nonlinearities throughout the computations but needs a detection and postselection process to verify the outcome of the gate. An example of such process is the CNOT gate presented by Pittman, *et al.* [72] (see fig.5.3a), in which the CNOT gate only works when a single photon is detected on each of the polarization-sensitive detectors. In the case of the single-rail encoding, the nonlinearity is present in the computation of the scheme but there is no detection required to ensure that the gate has been successful.

In the work presented in Section 7.1 the information is single-rail encoded. More precisely, our logic 1 is represented by the presence of a resonant plasmon and the logic 0 is given by the absence of this plasmon. Neglecting experimental imperfections, this type of encoding enables creating entanglement in a deterministic manner and there is no need to detect the output to ensure that the gate has performed correctly. Nonetheless, as mentioned before, single-qubit operations remain a challenge. However, it has been shown that one can switch encodings [53, 55]. Thus, although our proposed quantum computation platform with graphene plasmons is based on single-rail encoding, one could switch to dual-rail encoding if needed.

Although we have not studied the self- or cross-phase modulation (XPM) on our SWAP<sup>1/2</sup> based on plasmons in graphene nanoribbons, it is important to mention that the strong third-order nonlinearity of graphene could affect the fidelity of this gate via the Kerr effect. In 1995, Chuang and Yamamoto [13] suggested that the XPM between two optical fields could be used for universal quantum computation, provided that the nonlinearity was sufficiently large. In the Kerr effect, due to the  $\chi^{(3)}$  of a nonlinear medium, the presence or absence of a photon conditions the phase shift of another photon. In single-rail encoding, where  $|0\rangle$  and  $|1\rangle$  refer

to the vacuum and single-photon states, respectively, the XPM is given by,

$$\frac{1}{\sqrt{2}}(|0\rangle + |1\rangle) |1\rangle \rightarrow \frac{1}{\sqrt{2}}(|0\rangle + e^{-i\phi} |1\rangle) |1\rangle \quad (5.11)$$

where  $\phi = \kappa n_1 n_2$  is the phase shift that depends on the number of photons in each mode,  $n_1$  and  $n_2$ , and  $\kappa$  is a constant that depends on the material's nonlinear strength. The interesting thing of such operation is that with  $\kappa = \pi$ , in the  $(|0\rangle \pm |1\rangle)/\sqrt{2}$  basis, this is equivalent to a CNOT operation. However, materials with such strong nonlinearities also lead to large losses due to absorption. To avoid this problem, in 1996, Schmidt and Imamoglu [84] found a giant Kerr-effect by resonantly enhancing the Kerr nonlinearity while also decreasing the linear susceptibilities, which is the cause of the strong absorption and consequent losses. Without entering into too much detail, their scheme took advantage of the strong nonlinearity to induce a strong electromagnetically induced transparency (EIT) that would diminish the losses, while still having a strong XPM.

Ever since, these very promising approaches aroused great curiosity and there are several studies that have put into question the fidelity of such XPM gates. In 2006 Shapiro [85] carried out a thorough study, where he considered the multimode and continuous-time nature of the quantized electromagnetic fields taking part in the XPM. In other words, he studied the response time and duration of the nonlinear response with respect to the temporal duration of the single-photon pulse, which is related to the bandwidth of the photon. In his article he considered two regimes. The first one is the fast-response regime, where the nonlinear response happens very fast compared to the pulse duration. In this case, he found that it is possible to induce a  $\pi$  phase shift but that it only occurs in a very short region of the single-photon pulse and at a random time. Therefore, no overall phase shift is observable. In the second regime, he considered the nonlinear response time to be much longer than the pulse duration. In this case, he found that an overall  $\pi$  phase shift can be easily achieved but that the noninstantaneous nonlinear response leads to noise-phase terms that have a large negative impact on the fidelity of this XPM gate.

Supporting Saphiro's claims, in 2010, Gea-Banaacloche [32] studied a similar XPM gate but he described the travelling fields as localized single-photon pulses, which would be comparable to the fast-response regime in Shapiro's work. He came to the same conclusion: that large phase shifts would only be possible if the bandwidth of the nonlinear medium is close to the spectral width of the single-photon pulse; that is, when the response time of the nonlinear interaction is equivalent to the temporal width of the photon. However, he also pointed out that in this regime the EIT suggested in [84] would no longer be strong enough to suppress the losses arising from the strong absorption in the material.

In conclusion, phase modulation induced by third-order Kerr nonlinearities is an extremely

involved study that has been going on for decades. I would like to point out that the work presented in Section 7.1, and specially the fidelity estimation of the gate, does not include a study on the possible phase modulations that plasmons could undergo in the presence of graphene's  $\chi^{(3)}$  nonlinearity. Therefore, beyond the simplistic model in which our work is based, further analysis are needed to be able to give a quantitative value of the fidelity of the gate considering these effects.

### 5.3.2 Mathematics of a SWAP<sup>1/2</sup> based on a directional coupler

In this section we will introduce the square-root of SWAP (SWAP<sup>1/2</sup>) gate performed with a directional coupler, which is the basis of the work presented in Section 7.1. To understand how this universal SWAP<sup>1/2</sup> works, let us start by introducing the SWAP gate first. This is a two input and two output gate, where the qubit input in one of the modes always *swaps* to the other output port (see Fig. 5.5a). Now, one can imagine that this swapping process happens only *halfway*, so that one can no longer determine whether the qubit was swapped or not (see Fig. 5.5b). And this is indeed how the SWAP<sup>1/2</sup> gate works. The name is given due to the fact that by applying twice the SWAP<sup>1/2</sup> gate, one ends up with the SWAP gate.

Focusing on photons, this gate can be carried out by a simple 50 – 50% beam splitter, where the photon entering one port ends in a superposition of both output ports. However, this change of states happens in a single step and, due to the requirements of our work, we need the SWAP to be a continuous process, where one can interact with the system while the swapping process is happening. This can be done using a directional coupler to perform the SWAP<sup>1/2</sup> gate. As shown in Fig. 5.5c, a directional coupler consists of two photonic waveguides placed so close to each other that the fields of the waveguide modes overlap due to evanescent coupling. There is certain length  $L$  after which a photon input in the upper port will always exit the lower port. However, as shown in Fig. 5.5d, if this interaction length is shortened to half,  $L/2$ , one can no longer determine whether the photon swapped modes or not, and this uncertainty creates a quantum superposition of modes between the upper and the lower port. Thus, this process corresponds to a SWAP<sup>1/2</sup> operation. Now we will go through the theory behind an optical directional coupler built with waveguides to be able to calculate the interaction length  $L$  and its dependence on the evanescent coupling between the waveguides  $\kappa$  [90].

Let us assume that two waveguides with refractive indices  $n_1$  and  $n_2$  are placed close to each other, as shown in fig. 5.6. We will also assume that the waveguides are single-mode and that the light, polarized along the  $y$ -axis, propagates along the  $z$ -axis. Under these assumptions,

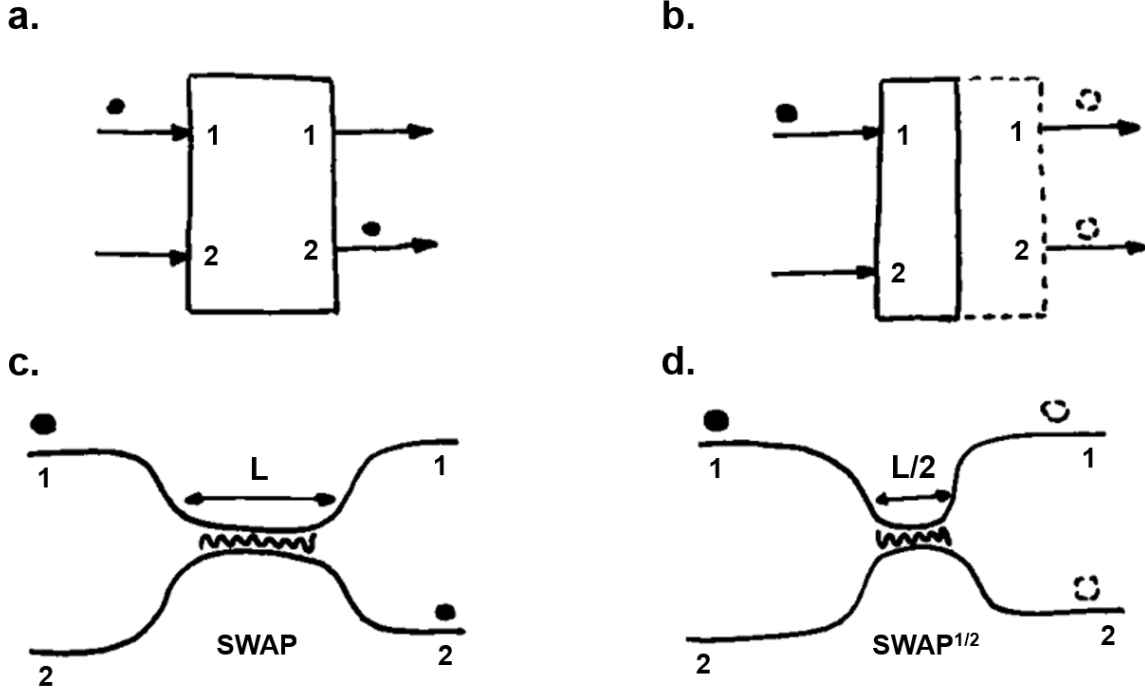


**Figure 5.5. Concept of a  $\text{SWAP}^{1/2}$  gate with a directional coupler.** a. On a SWAP gate, the qubit always swaps modes between the input and the output ports. b. When this SWAP operation is only performed halfway, one can no longer define whether the qubit has swapped modes or not, thus creating a superposition of output modes. In a directional coupler, two waveguides are placed so close to each other that the evanescent field of the photon allows it to swap from one mode to the other. c. There is a certain interaction length  $L$ , after which it is certain that the qubit has swapped modes. d. However, if this interaction length is shortened to  $L/2$ , one can no longer determine whether the SWAP has happened or not, leading to a superposition of output modes; that is, a  $\text{SWAP}^{1/2}$  operation.

we can write the wave equation for each waveguide as

$$\nabla^2 E_i(x, y, z) + n_i^2 k_0^2 E_i(x, y, z) = 0 \quad (5.12)$$

where  $i = \{1, 2\}$  for waveguide 1 and 2, respectively, and  $n_i = n_i(x, y)$  is the refractive index that we will assume to be constant over the entire propagation length. The solution to this wave equation is found to be

$$E_i(x, y, z) = E_i(x, y) e^{-i\beta z}, \quad (5.13)$$

where  $\beta = k_z$  is the wave vector in the propagation direction. If we try these solutions in the wave equation 5.12, we will end up with the following expression, which will come in handy

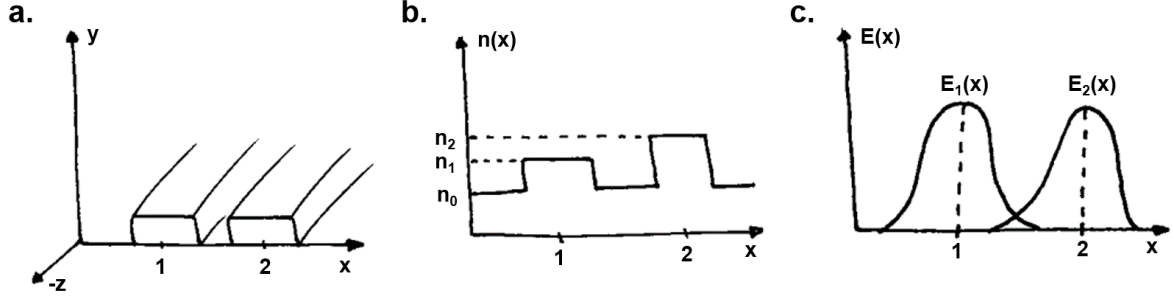


**Figure 5.6. SWAP<sup>1/2</sup> gate** **a.** Sketch of the arrangement of the waveguides in a directional coupler. **b.** Refractive index as a function of  $x$ . In this example the waveguides have different refractive indices but we have considered the case with identical waveguides. **c.** Field distributions of both waveguides, where the overlapping tails contribute to the coupling between them.

couple of steps ahead:

$$\nabla_{xy}^2 E_i(x, y) + \left( n_i^2 k_0^2 - \beta_i^2 \right) E_i(x, y) = 0 \quad (5.14)$$

where  $\nabla_{xy}^2$  is the Laplace operator defined as

$$\nabla_{xy}^2 f(x, y) = \Delta_{xy} f(x, y) = \frac{\delta^2 f}{\delta x^2} + \frac{\delta^2 f}{\delta y^2} \quad (5.15)$$

We will now consider the system as a whole, and have a single total refractive index  $n_T(x, y)$  that is valid for both waveguides. The total wave equation is then

$$\nabla^2 E(x, y, z) + n_T^2 k_0^2 E(x, y, z) = 0 \quad (5.16)$$

and the solution has the form

$$E(x, y, z) = A_1(z) E_1(x, y) e^{-i\beta_1 z} + A_2(z) E_2(x, y) e^{-i\beta_2 z}. \quad (5.17)$$

If we insert this solution into the wave equation 5.16 and use the single wave equations 5.14 to replace the  $\nabla_{xy}^2 E_i(x, y)$  terms, we can reduce the expression to

$$\sum_{i=\{1,2\}} \left[ \frac{\delta^2 A_i(z)}{\delta z^2} - 2i\beta_i \frac{\delta A_i(z)}{\delta z} + k_0^2 (n_T^2 - n_i^2) A_i(z) \right] E_i(x, y) e^{-i\beta_i z} = 0 \quad (5.18)$$

Note that  $n^2 = \epsilon$  is the dielectric constant. Therefore, one can interpret  $(n_T^2 - n_i^2)$  as the perturbation of the dielectric constant in the first waveguide, due to the presence of the field in the second waveguide, and *vice versa*. We can further simplify this expression by considering that the wave amplitudes,  $A_1(z)$  and  $A_2(z)$  evolve very slowly in time and thus we can assume that  $\frac{\delta^2 A_i(z)}{\delta z^2} = 0$ . Moreover, we can divide everything by  $e^{-i\beta_1 z}$  and have a single exponential decay as  $e^{-i\Delta\beta z}$ , where  $\Delta\beta = \beta_2 - \beta_1$  represents the phase mismatch between the first and the second mode.

After some mathematical tricks, we finally reach to the so-called coupled mode equations, which are given by

$$\frac{\delta A_1}{\delta z} + i\kappa A_2 e^{-i\Delta\beta z} = 0 \quad (5.19a)$$

$$\frac{\delta A_2}{\delta z} + i\kappa A_1 e^{-i\Delta\beta z} = 0, \quad (5.19b)$$

where  $\kappa$  is the coupling constant

$$\kappa = \frac{k_0^2}{2\beta} \frac{\langle (n_1^2 - n_2^2) E_2, E_1 \rangle}{\langle E_1, E_1 \rangle} \quad (5.20)$$

Here we have used the bracket notation where  $\langle E_i, E_j \rangle = \iint E_i E_j^* dx dy$  and we have assumed  $\beta_1 = \beta_2 = \beta$ . We will now look for the easiest solution to this system of equations, where the waves propagate synchronously; that is, without any phase mismatch,  $\Delta\beta = 0$ . Under this assumption, we arrive at the solution

$$A_1(z) = C_1 \cos(\kappa z) + C_2 \sin(\kappa z), \quad (5.21)$$

where  $C_1$  and  $C_2$  are constants that will be determined by the boundary conditions. To do so, we can consider that initially, at  $z = 0$ , there is only light in one of the waveguides, so  $A_1 = 1$  and  $A_2 = 0$ . By applying these into equations 5.19, we find

$$A_1(z) = \cos(\kappa z) \quad (5.22a)$$

$$A_2(z) = -i \sin(\kappa z) \quad (5.22b)$$

so the probability of finding light in waveguide 1 and 2 at a specific  $z$  are  $P_1 = A_1 A_1^* = \cos^2(\kappa z)$  and  $P_2 = A_2 A_2^* = \sin^2(\kappa z)$ , respectively. This means that the interaction length between the waveguides, after which the light has swapped from one waveguide to the other depends on the coupling between these; the stronger the coupling, the shorter the interaction length needs to be for the SWAP<sup>1/2</sup> process to happen.

## 5.4 The Zeno effect

The Zeno effect alters the time evolution of a system depending on the observations that are made on it [62]. In order to give a comprehensive and intuitive understanding, we will introduce two main interpretations and corresponding examples, where the first one is based on a quantum system and the second one can be completely explained by classical mechanics.

The first explanation is based on the following claim: *Continuous observation of the system*

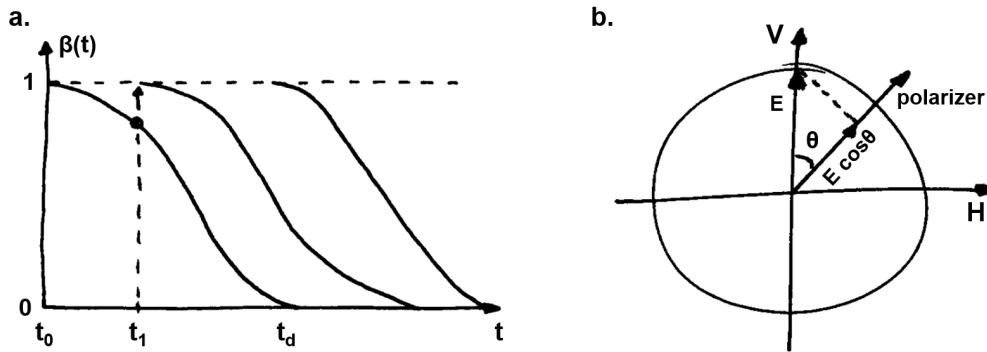


**Figure 5.7. Sketched examples of the Zeno effect interpretations.** **a.** If the system is prepared in the excited state at  $t_0$ , in the absence of external forces, it will decay into the ground state at time  $t_d$ . However, if continuous observations are carried out, these measurements will keep collapsing the system into the excited state and will keep it in place. **b.** If the polarizer is set perpendicular to the incident light, no light will make it through. However, if the polarizer angle is slowly rotated starting from the polarization of the incident light, this will evolve in a way to adapt and avoid the loss channel. In this case the beam will change the polarization to that set by the polarizer.

*keeps the system in place.* Let us imagine a two-level quantum system, where we define a ground state  $|g\rangle$  and an excited state  $|e\rangle$ . As shown in Fig. 5.7a, if the system is prepared in the excited state at certain initial time  $t_0$ ,  $|\psi(t = t_0)\rangle = |e\rangle$ , it is inevitable that, without any external interaction, it will decay back to the ground state within certain time  $t_d$  that will vary depending on the system's details; that is,  $|\psi(t = t_d)\rangle = |g\rangle$ . Now, let us assume that we perform a measurement at a time  $t_1$ , shortly after  $t_0$ . At this point, the system will be in a superposition of states in the form of

$$|\psi(t = t_1)\rangle = \alpha(t_1) |g\rangle + \beta(t_1) |e\rangle, \quad (5.23)$$

where  $\alpha(t)$  and  $\beta(t)$  are probability coefficients that vary in time and are normalized such that  $|\alpha(t)|^2 + |\beta(t)|^2 = 1$ . In a handwavy manner, from the graph we can see that if the measurement is carried out right after  $t_0$ ,  $\alpha(t_1) \ll \beta(t_1)$ , and the probability of finding the system in the excited state is close to one. If this would indeed be the case, our measurement would collapse the superposition state into the state  $|\psi(t_1)\rangle = |e\rangle$ . Therefore, if we would repeat this measurement within tiny time intervals,  $\Delta t \ll (t_d - t_0)$ , we would be continuously collapsing the system into the excited state; i.e., keeping the system in place.

The second interpretation is based on the following statement: *The system always evolves in a way to avoid loss channels.* To get a more intuitive understanding of this interpretation, let us imagine a linear polarizer at which a V polarized wave is impinged (see Fig. 5.7b). If the polarizer is set to H, within the experimental error, there will be no light passing through the polarizer. However, if the angle of the polarizer is set close to the vertical,  $\theta \ll 1$ ,  $E \cos \theta$  amount of light will make it through the polarizer and this will have the same polarization as that from the polarizer. If we stack  $n$  polarizers, each one rotated by  $\theta$  with respect to the

previous one, where  $\theta = \pi/2n$ , we will end up with  $(E \cos \theta)^n$  field transmitted through the final polarizer. For  $n \rightarrow \infty$ , the system would slowly change the polarization and all the light would be transmitted through the polarizer. Thus, the system would have evolved to avoid the loss channel. [43]

#### 5.4.1 The Elitzur-Vaidman Bomb experiment

We now present one of the first applications of the quantum Zeno effect: the bomb-tester, which will be the basis of the work presented in Section 7.2. This is a thought experiment presented by Avshalom Elitzur and Lev Vaidman in 1993 [21]. It is based on interaction-free measurements, in which one can obtain information about a system without actually interacting with it. This is indeed a controversial concept given the disruptive nature of measurements in quantum mechanics. In principle, measuring a quantum state in a superposition of pure states collapses it into a single pure state, thus destroying and erasing all the information about the initial state of the system.

To understand their proposed experiment, let us assume a perfectly balanced Mach-Zehnder interferometer (MZI) composed by two perfect 50/50 beam splitters (BS) and two perfect mirrors (m), which we arrange as shown in Fig. 5.8a

If the upper and lower arms of the interferometer are balanced, when a photon is input in the lower path, self-interference makes it exit the upper output port with 100% probability. Now imagine that, as shown in Fig. 5.8b, a photon-sensitive bomb is placed on the upper arm of the MZI; i.e. the bomb explodes if there is a photon in the upper path. If we input a photon into the lower input port, there is a 50% chance that the photon will be transmitted into the upper path and the bomb will explode, but there is also a 50% chance that the photon will be reflected into the lower path, the bomb will not explode and the photon will bounce off the lower mirror and impinge on the lower input port of the second BS. Here again the photon has 50 – 50% probability of outputting the upper or lower path. Hence, in total, if the bomb does not explode, we have a 75% chance of finding the photon in the upper output port and 25% probability of finding it in the lower output port. This means that if, with 25% chance, the photon is found in the lower port, we can be sure that there is a bomb without ever detonating it.

As a follow up to this thought experiment, in 1995 Paul Kwiat, *et al.* [52] realized that the probability of detecting the bomb without interacting with it can be made arbitrarily close to unity if many MZIs are concatenated as shown in Fig. 5.9. As we will show, this success probability depends on the number of BSs in the concatenated MZI (cMZI).

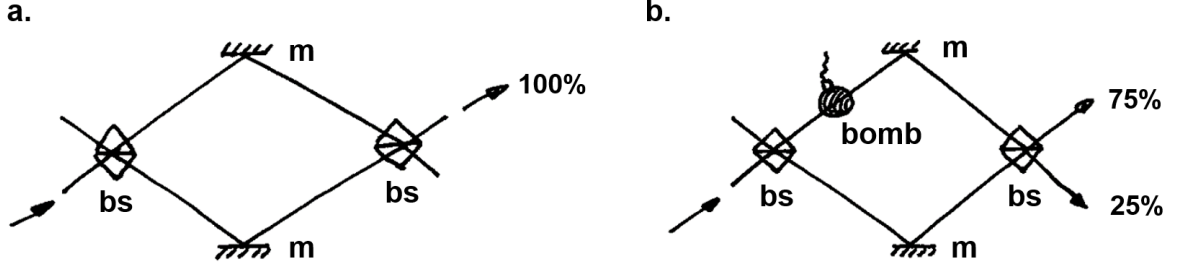


**Figure 5.8. Bomb-tester thought experiment.** **a.** When the upper and lower arms of a Mach-Zehnder interferometer are balanced, if a photon is inserted in the lower input port, its self-interference will make it always exit through the upper output port. **b.** However, when a bomb is placed on the upper arm, if the bomb is not detonated, the photon has 75% and 25% probability of exiting the upper and lower ports, respectively. Thus, one can detect whether a bomb is present without ever interacting with it.

We will use the matrix notation where a BS is represented by

$$\hat{B}(\theta) = \begin{pmatrix} \cos \theta & \sin \theta \\ -\sin \theta & \cos \theta \end{pmatrix} ; \quad \hat{B}(\theta = \pi/4) = \begin{pmatrix} 0 & 1 \\ -1 & 0 \end{pmatrix} \quad (5.24)$$

where the  $\theta = \pi/4$  corresponds to a 50 – 50 BS. It is easy to show that when  $N$  BS operations are applied, the operator can simply be written as

$$\hat{B}(\theta)^N = \begin{pmatrix} \cos N\theta & \sin N\theta \\ -\sin N\theta & \cos N\theta \end{pmatrix} \quad (5.25)$$

where we need  $\theta = \pi/2N$  to achieve perfect interference in the absence of bombs in the cMZI. Let us first consider what happens when a photon enters the empty cMZI in the lower input port of the first BS.

$$\hat{B}(\theta = \pi/2N)^N |\downarrow\rangle = \begin{pmatrix} \cos N\frac{\pi}{2N} & \sin N\frac{\pi}{2N} \\ -\sin N\frac{\pi}{2N} & \cos N\frac{\pi}{2N} \end{pmatrix} \begin{pmatrix} 0 \\ 1 \end{pmatrix} = \begin{pmatrix} 1 \\ 0 \end{pmatrix} = |\uparrow\rangle \quad (5.26)$$

where we define the input basis to be  $|\uparrow\rangle = \begin{pmatrix} 1 \\ 0 \end{pmatrix}$  and  $|\downarrow\rangle = \begin{pmatrix} 0 \\ 1 \end{pmatrix}$  representing the upper and lower arms, respectively. This solution shows that, regardless of  $N$ , in the absence of a bomb, the photon always outputs the upper port.

We now consider the case in which bombs are placed along the upper arm of the cMZI.

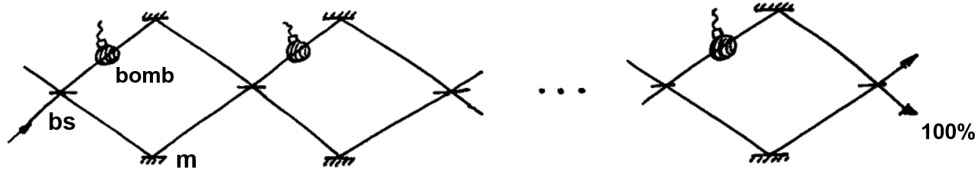


**Figure 5.9. Concatenated Mach-Zehnder interferometers.** Kwiat, *et al.* noticed that the probability of determining whether a bomb is present in the interferometer or not can be arbitrarily high if one concatenates several Mach-Zehnder interferometers. The success probability is thus proportional to the total number of BSs chained.

After the first BS, the probabilities of the photon being transmitted to the upper path  $|\uparrow\rangle$  or reflected to the lower arm  $|\downarrow\rangle$  are

$$\hat{B}(\theta = \pi/2N) |\downarrow\rangle = \begin{pmatrix} \cos \theta & \sin \theta \\ -\sin \theta & \cos \theta \end{pmatrix} \begin{pmatrix} 0 \\ 1 \end{pmatrix} = \sin \theta |\uparrow\rangle + \cos \theta |\downarrow\rangle \quad (5.27)$$

where  $|\sin \theta|^2$  and  $|\cos \theta|^2$  are the probabilities of finding the photon in the upper and lower paths, respectively. Since we are only interested in the probability of detecting the bomb without interacting with it, we will only pay attention to the second term. If we expand this solution to  $N$  number of BSs, the probability would be  $|(\cos \pi/2N)^N|^2$ , which in the  $N \rightarrow \infty$  limit goes to 1. Thus, we have shown that the success probability does indeed depend on the number of concatenated BSs, where already  $N = 4$  gives a  $> 50\%$  success.

In this chapter we have gone through the basic mathematical description of quantum computation and paid special attention to quantum logic gates. In particular, we have introduced the universal SWAP<sup>1/2</sup> gate, which we have implemented on a plasmon-based directional coupler, shown in Section 7.1. In the final part, we have put our focus on the Zeno effect, which is the key effect in both the theoretical work presented in Section 7.1 and the experimental work introduced in Section 7.2.

# Chapter 6

## Experimental Graphene Research

### 6.1 Quantum proposal

This thesis work was initially funded by the European project called Graphene-based single-photon nonlinear optical devices (GRASP). Based on the goals of this project, the purpose of this thesis is to find an approach to achieve nonlinear optical properties at the single-photon level and on a chip scale. This achievement would revolutionize classical information technologies, enabling all-optical routing and switching, wavelength conversion or high-bandwidth communication in the nanoscale and open the door to quantum computing. Ultimately, the realization of such a device would leave aside high-power optics and bulk systems, which is the current major limitation toward universal and scalable photonic quantum computing.

This regime of single-photon nonlinear optics would thus enable to create new ways to manipulate photons beyond what classical technology allows. The goal of this project is an extremely important building block for quantum technologies and could result in single-photon sources, secure quantum communication, metrology or quantum sensing.

The main limitation of nonlinear optical approaches to quantum computing is the weak nonlinearity of currently available materials, which leads to setups with high intensities and long interaction lengths, thus hindering their scalability and industrial applicability. This project aims to overcome this barrier by using graphene-based nanostructures, where the nonlinearity surpasses that of bulk nonlinear crystals by several orders of magnitude. Apart from the huge intrinsic nonlinearity of graphene that is given by its particular band structure, nonlinearities in graphene can be driven by plasmons, whose wavelength can be three orders of magnitude smaller than that of the free space field exciting them. Therefore, this feature results in huge field confinements, leading to unprecedented effective optical nonlinearities.

The aim was originally to observe strong graphene-based nonlinearities via the so-called photon-blockade effect. To explain how this classical nonlinearity can lead to a quantum emission of light, let us imagine a bulk cavity with a third-order nonlinear media inside (see Fig. 6.1a). Classically, the resonance frequency of the cavity depends on the nonlinear refractive index of this media, which, at the same time, depends on the incident intensity  $I$  as

$$\omega(I) = \omega_0 + \beta I \tag{6.1}$$

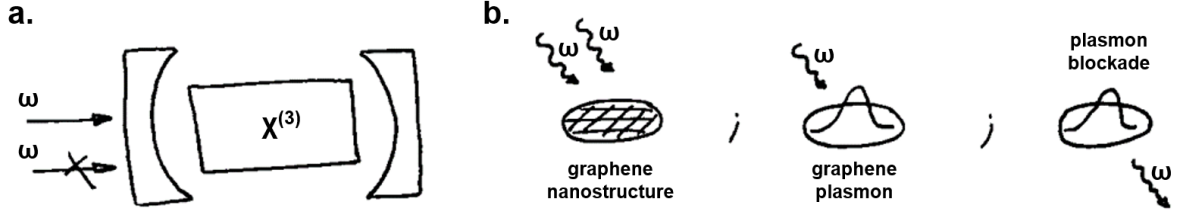


**Figure 6.1. Photon-blockade.** **a.** Classically, when a nonlinear medium is placed in a cavity, the resonance frequency depends on the refractive index of the material. At the same time, this refractive index varies with intensity. Thus, when a resonant photon enters the cavity, the refractive index of the nonlinear media changes, which leads to a shift of the cavity resonance, which means that the next photon will need some extra energy to be resonant. **b.** A graphene nanostructure works as a cavity for plasmons. When a photon excites a plasmon in the graphene, the resonance energy of the nanostructure shifts so a second photon would require a different frequency to be resonant to the system.

where  $\omega_0$  is the resonance of the empty cavity and  $\beta$  is a material-dependent parameter that contains the nonlinearity.

From a quantum mechanics perspective, the energy is quantized and the nonlinear interaction can be interpreted as an extra energy  $u$  required to add a second photon into the cavity after a photon is already present. In other words, as shown in Fig. 6.1a, the interaction between the first photon with  $\omega$  and the nonlinear media leads to a shift of energy  $u$  in the resonance frequency of the system (now consisting of the nonlinear media and the first photon). Thus, the second photon can only enter the cavity if its energy is  $\omega + u$ . This energy shift depends on the third-order nonlinearity  $\chi^{(3)}$  and the mode volume of the cavity  $V$  as

$$u \propto \frac{\chi^{(3)}}{V}. \quad (6.2)$$

In the ideal case, we want  $u$  to be as big as possible so that no second photon can enter the cavity, but in practice, it is enough if the energy shift is larger than the bandwidth of the photon;  $u \gg \Delta\omega$ .

In the case of graphene nanostructures, the nanostructure itself acts as a cavity (see Fig. 6.1b). If the first photon is resonant to the cavity,  $\omega = \omega_c$ , this will excite a graphene plasmon and the resonance of this excited cavity will be shifted by  $u$ . Here the shift and bandwidth relation is given by,

$$\frac{u}{\Delta\omega} \propto \frac{\chi^{(3)}Q}{V} \quad (6.3)$$

where  $Q$  is the quality factor of the cavity, which will depend on the edges and impurities of the graphene, and  $V$  is the mode volume of the plasmon, which can be a million times smaller than that of the free space, as  $\lambda_{sp} \sim \alpha\lambda_0$ , where  $\alpha \sim 1/137$ , and  $V \sim \lambda_{sp}^3$ . Thus, combining all the properties of these graphene nanostructures (strong  $\chi^{(3)}$ , high  $Q$  and small  $V$ ), it is relatively easy to reach the ultimate condition for deterministic photon-blockade;

$u/\Delta\omega \gg 1$ .

For this ambitious project, four different institutions and six research groups worked together for 3 years. At the Institut de Ciències Fòniques, in Spain, the group of Frank Koppens was responsible for the fabrication and linear optical characterization of graphene nanostructure samples and the groups of Darrick Chang and Javier García de Abajo were in charge of the theory development. At the University of Exeter, in the United Kingdom, the group of Prof. Euan Hendry was in charge of the nonlinear experiments, the group of Fariba Hatami at the Humbolt University in Germany, developed technology for photon-plasmon coupling and at the University of Vienna, in Austria, we were responsible for the development of single-photon detectors in the NIR. Although the original plan was adapted as experimental difficulties were found on the way, the main steps in which the whole project was divided were:

- Producing graphene nanostructures that are capable of sustaining high-quality (long lived) plasmons in a broadband wavelength in the NIR and visible regime.
- Observing and studying the plasmonic nonlinear enhancement in such structures.
- Confirming classical optical switching at the level of several-photon occupation numbers in the graphene nanostructures.
- Measuring photon antibunching provided by the photon-blockade in the cavities defined by the nanostructures.
- Observing quantum mode-splitting arising from the second-order nonlinearity of graphene.
- Developing comprehensive theories for second- and third-order nonlinear processes in graphene nanostructures.
- Proposing novel applications for this technology in areas such as quantum information processing or quantum simulation.
- Implementing photonic-plasmonic structures to overcome the huge momentum mismatch and consequent coupling limitations.

## 6.2 Towards the quantum regime

Initially, the group of Prof. Euan Hendry was going to perform the measurements of nonlinear effects with graphene nanostructures, as they had already observed nonlinear signals from graphene before [37]. Our goal was to develop single-photon detectors in the  $1 - 2\mu m$  regime. However, since our best bet was using superconducting nanowire single-photon (SNSP) detectors, we needed to perform the measurements in Vienna, as these detectors require cryogenic

temperatures and cannot be transported easily. In addition, we also needed a laser system that would allow us to characterize the detectors in the NIR, as we only had sources with longest wavelengths at the telecom regime ( $\sim 1550$  nm). Thus, we decided to take part in the experimental observations of the nonlinear effects with graphene based devices.

As we had little experience in the field of classical nonlinear optics, we joined Prof. Euan Hendry and his students on two different occasions, for a total of 20 days, to both acquire the required experience for us to be able to set our own experiments in Vienna, and to together characterize the first set of samples that the group of Frank Koppens had fabricated. This consisted of CVD graphene, where arrays of nanoribbons with widths  $\sim 100 - 500$  nm were etched. Although these measurements did not succeed, it is relevant for this thesis to introduce the original setup and its characteristics as we now understand the reasons why we could not observe any nonlinear signal from graphene with Exeter's setup.

### 6.2.1 First steps in Exeter

Due to the collaboration with Prof. Euan Hendry at the University of Exeter we had access to two independent optical parametric amplifiers (OPA) that were pumped by a Ti:sapph laser with 1 kHz repetition rate and  $\sim 200$  ps pulse length. These led to tunable wavelengths in the  $0.2 - 10$   $\mu\text{m}$  range. This would allow any nonlinear measurement without any restriction on the incident wavelengths, as these two beams are not spectrally correlated. In this case, we performed four-wave mixing experiments, where the beam from the first  $\omega_1$  and second  $\omega_2$  OPAs are mixed as

$$2\omega_1 - \omega_2 = \omega_{\text{FWM}} \quad (6.4)$$

As shown in Fig. 6.2, both beams were focused and impinged on the sample with angles  $\alpha$  and  $\beta$  with respect to the normal. This configuration was designed both for convenience to spatially overlap the beams into the sample and for spatially separating the FWM signal  $\omega_{\text{FWM}}$  at the output.

Due to the momentum conservation, it is straightforward to calculate where the FWM signal should be collected:

$$2\mathbf{k}_1 - \mathbf{k}_2 = \mathbf{k}_{\text{FWM}} \quad (6.5a)$$

$$\frac{2}{\lambda_1} \sin \alpha - \frac{1}{\lambda_2} \sin \beta = \frac{1}{\lambda_{\text{FWM}}} \sin \gamma \quad (6.5b)$$

This detection was done using an avalanche photodiode (APD) (Thorlabs APD120A) with a sensitivity of  $0.20$  pW/ $\sqrt{\text{Hz}}$ . The measurements consisted of recording the collected power as a function of the delay stage, as it was moved back and forth to bring both beams in and

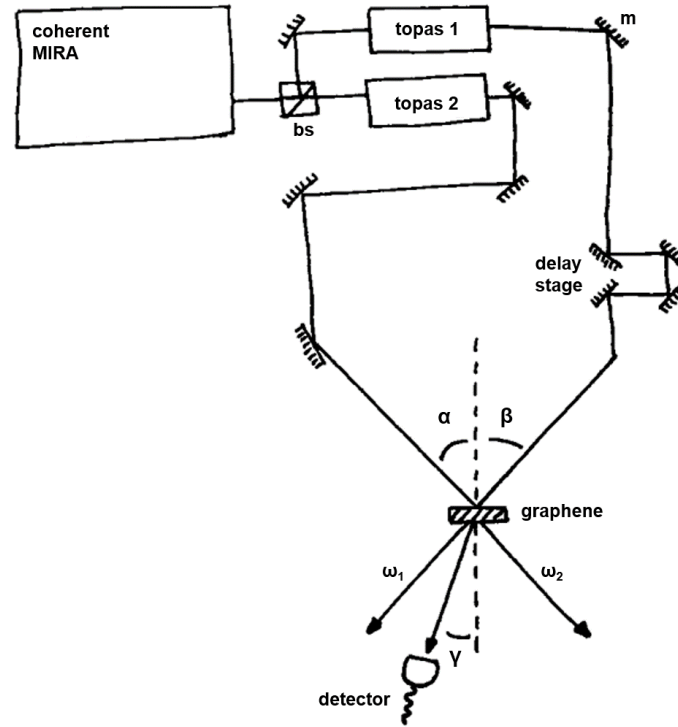


**Figure 6.2. Setup in Exeter.** A 1kHz pulsed laser pumps two independent OPAs with tunable wavelengths in the 480 – 2600 nm. These two beams are then spatially and temporally overlapped on the graphene sample and the generated FWM signal is collected at the angle given by momentum conservation. This is done with an APD. Hence, the measurement consists of monitoring the detected signal as a function of the temporal overlap between the beams; only when both beams coincide temporally will the FWM process take place.

out of time overlap. Thus, only when the beams were temporally overlapped would the signal appear. As a practical note, bear in mind that, due to the repetition rate and pulse length of such laser systems, the pulses are meters apart from each other and that one needs to find the time overlap with micrometer precision prior to the actual measurement. We did this by first inserting a nonlinear crystal in the position where the sample would be placed later.

During the time we spent in Exeter, we did not manage to measure any FWM signal generated by the graphene nanoribbons, but we saw a FWM signal from the  $SiO + Si$  substrate on which the graphene was grown, which is known to have an optical third-order nonlinearity. This confirms that, although we could not distinguish a signal from graphene, the method was not the problem, as we had both spatial and temporal overlap between the two beams.

We later realised that because of the low repetition rate of the laser, the incident fluence was way above the damage threshold of graphene [15] so we had to lower it. We had high peak powers, low average power, and this led to extremely low average powers of the nonlinear signal.

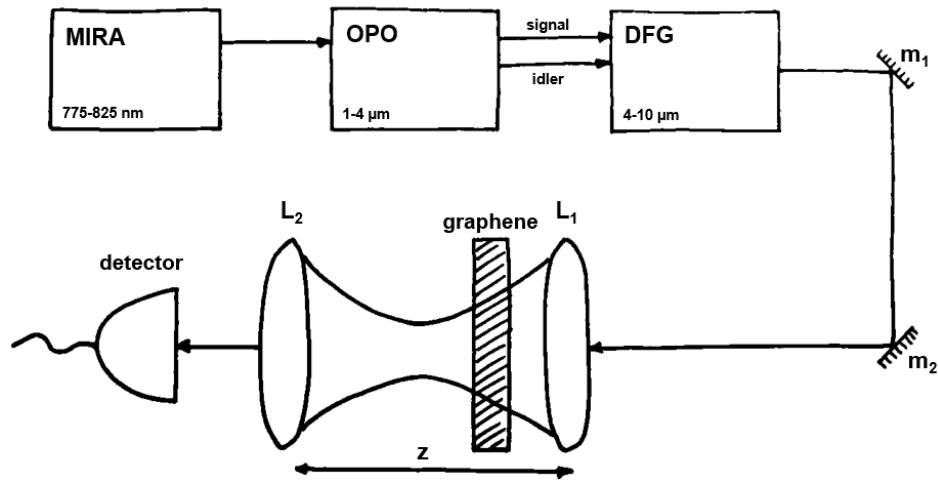


**Figure 6.3. Setup in Vienna.** A 80MHz pulsed laser pumps an OPO, whose signal and idler beams cover the  $1 - 4 \mu\text{m}$  wavelength range. These are further mix on a DFG process, covering the spectrum all the way to  $10 \mu\text{m}$ . Due to the architecture of the setup, both spatial and temporal overlap are given. The beams are then focused down and collimated via two short focal length lenses, in between which the sample is placed. A set of series will then filter the pump beams from the created nonlinear signal (FWM, THG...) and these are measured using a single-photon APD or a SNSP detector, depending on the wavelength. The measurement thus consists on detecting the nonlinear signal as the sample is moved in and out of the focus; the signal is biggest at the focal point.

### 6.2.2 First steps in Vienna

The acquired expertise from Prof. Euan Hendry's group, allowed us to quickly start our own research at the University of Vienna. We purchased a Mira-OPO-XP from Coherent and APE, which combines three modules to cover the  $1 - 10 \mu\text{m}$  wavelength. A 80 MHz repetition rate Ti:sapph tunable in the  $775 - 825 \text{ nm}$  range pumps the OPO with  $\sim 200 \text{ fs}$  pulses. The OPO can be considered as a stimulated down conversion process, where the cavity set resonant to the signal beam and the phase matching conditions of the nonlinear crystal determine the preferable conversion wavelengths, always respecting energy conservation. In our OPO system, the cavity and crystal position are automatically optimized to have nonlinear emission in the  $1 - 4 \mu\text{m}$ , considering both the signal ( $1000 - 1600 \text{ nm}$ ) and idler ( $1600 - 4000 \text{ nm}$ ). The third and last module consists of a difference frequency generator (DFG), where the signal and idler beams from the OPO are spatially and temporally overlapped on another nonlinear crystal to generate a DFG signal in the  $4 - 10 \mu\text{m}$  range. The lower peak powers of this system let us get higher average power without reaching the damage threshold of graphene.

At first we tried to replicate the setup from Exeter but because our signal and idler beams are spectrally correlated, instead of pursuing FWM, we decided to look for THG, which is also a third-order nonlinear process but only needs a single input wavelength. In addition, we also simplified the measurement by using standard monolayer CVD graphene, as this had been previously observed [40]. So the difference in comparison to the scheme in Exeter is that

we would first split the beam into two and recombine them onto the sample, and look for the THG signal as a function of the delay.

For almost two years we tried different input wavelengths, spatial configurations and beam collection methods, including a home made spectrometer with a grating that would spatially separate the input from the generated THG signal, but we did not succeed to observe any signal from graphene. During this time, we developed the theoretical proposal of the SWAP gate presented in Section 7.1.

### 6.2.3 Success in Vienna

When looking for the THG signal, we realised that we had to change the way in which we were trying to perform the measurement. So we listed the main challenges of our setup, and looked for a configuration that would overcome all these problems.

In summary, the main issue was the number of uncertainties in the setup due to the required spatial and temporal overlap to create the nonlinear signal. This resulted in an inability to properly debug and fine-tune these parameters due to the long acquisition times required to compensate for the low signal-to-noise ratio of the detector. Therefore, we needed a scheme that would avoid the need for spatial and time overlap, and a detection method with higher sensitivity to reduce the measurement time.

As for the spatial and temporal overlap, the solution that we came up with is what we call the modified z-scan, shown in Fig. 6.3, where the measurement consists of looking at the filtered THG signal as a function of the sample in and out of the focal point of the incoming pump. Only when the intensity is maximum, at the focal point, would we expect a strong signal.

With regard to the detection problems, we decided to leave the photodiode aside and work with the tools that we felt most comfortable with: single-photon detectors. So, depending on the generated wavelength, we would either use an avalanche photodiode detector (APD) or a superconducting nanowire single-photon (SNSP) detector.

With this new setup, we finally succeeded in finding a THG signal and we were able to perform the measurements that are summarized in the paper in Section 7.3.

#### 6.2.3.1 Experimental details

In this section I am going to go through the basics of the setup alignment and provide worth mentioning insights that I found out over the years looking for a TH signal via the well-known *try and error* method. Although the setup is not too complex (there is no interferometer or

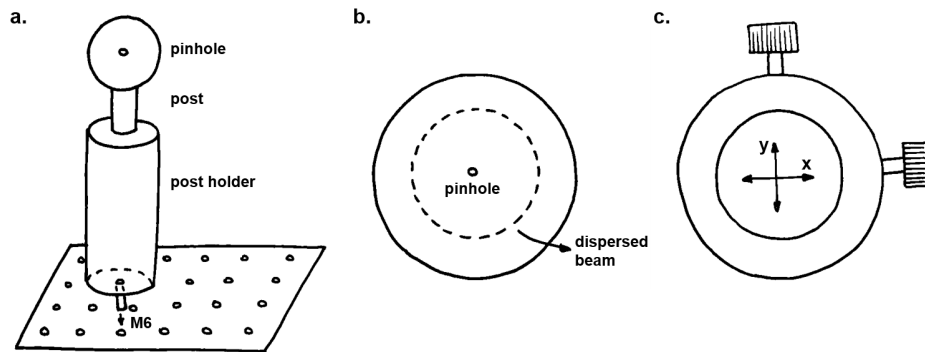


**Figure 6.4. Optical components.** a. It is recommendable screwing the post holder directly on the table holes instead of using clamps. This way it is easier to keep the beamline straight when other optical components are added. b. Sketch of the pinhole with the dispersed beam after this goes through the tight focus lens. c. Sketch of the lens holders with translation degree in the x and y direction.

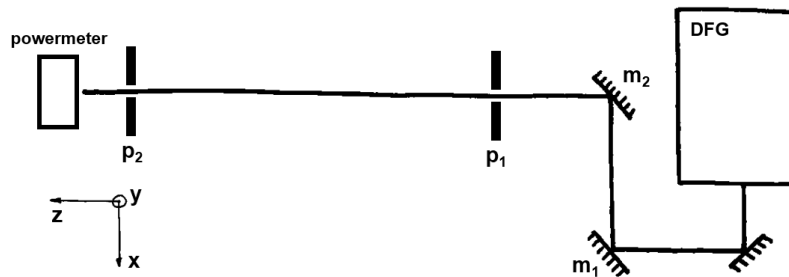


**Figure 6.5. Alignment procedure step 1.** Place pinholes  $p_1$  and  $p_2$  on the chosen line and steer the beam to follow this line by using mirrors  $m_1$  and  $m_2$ . First do it roughly using the IR card that allows you seeing the beam at 1500 nm and then proceed with the fine alignment by walking the beam into the powermeter, as explained in the main text.

component that requires active stabilisation), the main challenge relies on the operation in the regime of the NIR wavelength, which is invisible to the naked eye. The advantage, and sometimes disadvantage, is that, when using the DFG module, there is some leakage from the MIRA pump and the signal and idler beams. These shorter wavelengths can be very convenient when aligning, as these are visible with the help of an IR card.

As shown in Fig. 6.3, the light in the setup follows a straight line, so the main priority is to place the optical elements along this beam without distorting its path. I recommend using pinholes that are attached to the table, directly using the holes in the table, instead of using a clamp (see Fig. 6.4a). In this way, we make sure to always keep the straight line, parallel to the line of holes on the table. Regardless of the wavelength that we are using, the light beam always comes out of the DFG box. Although, in principle, one can align the setup with any wavelength, experience has taught me that the best is to start with the signal beam at 1500 nm. The first step is to direct the beam in a straight line parallel to the table holes. To be able to reach all the degrees of freedom you will need two mirrors,  $m_1$  and  $m_2$  in

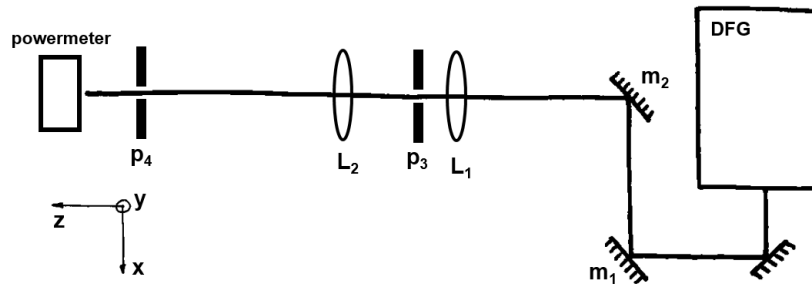


**Figure 6.6. Alignment procedure step 2.** Once the beam is properly align, proceed inserting the first lens  $L_1$  by taking pinhole  $p_3$  as a reference. Afterwards, collimate back the beam with lens  $L_2$ . Use pinhole  $p_4$  as a reference, both close to  $L_2$  and very far from it. Placing  $L_2$  on a translation stage will provide you the required accuracy to find the optimal distance between  $L_1$  and  $L_2$ .

Fig. 6.5. Our mirrors are protected silver mirrors that have close to unity reflectivity in an extremely broadband that include all our wavelengths. Screw the pinholes along the chosen line of holes, and place them around 40 cm away from each other. To redirect the beam, you will first roughly do it with the help of an IR card, with which the 1500 nm beam is visible. After the rough alignment, place the powermeter at the end of the beam line and tune the alignment. To do so, open  $p_2$  and close  $p_1$ . Note that *close* means leaving a hole of about 1 – 2 mm of diameter. Now move  $m_1$  to maximize the power at the powermeter. Once you have reached the maximum, open  $p_1$  and close  $p_2$  and maximize the power by moving  $m_2$  this time. You have to iterate this procedure until you reach a point, where you barely need to move the mirror in order to read the maximum value on the powermeter. This step has crucial importance because it sets the base of the entire setup so, as irrelevant as it might feel, do not rush it. Once this alignment is finished, I recommend never touching these pinholes again; they will always be your initial reference.

The second step is to place the lenses. Now the challenge is the extremely short focal length of these. This means that the beam suffers a large dispersion and thus it is difficult to determine the beam direction. I recommend screwing another pinhole  $p_3$  on a hole along the beam line, very close to the first lens  $L_1$  (see Fig. 6.6). This time make sure that the pinhole is centered and then use the IR card in front of it to make sure that the focused beam is still following the initial line. Place the lens roughly in position and fine-tune its position by using the translation degrees provided by the lens holder (see Fig. 6.4c). If you can place the pinhole close enough, you might be able to make the beam go through the pinhole but if you place the pinhole in a further position, it will be very dispersed so you will have to estimate the center. To have an idea, it will look similar to the inset in Fig. 6.4b. For the second lens, you can remove the pinhole and place it on position  $p_4$ . Bare in mind that the second lens will collimate the tightly focused beam and that, to achieve a good collimation, the distance between the two lenses needs to be extremely precise. Therefore, you will need to mount  $L_2$  on a translation stage that will allow you to fine tune its position along the beam line. Once

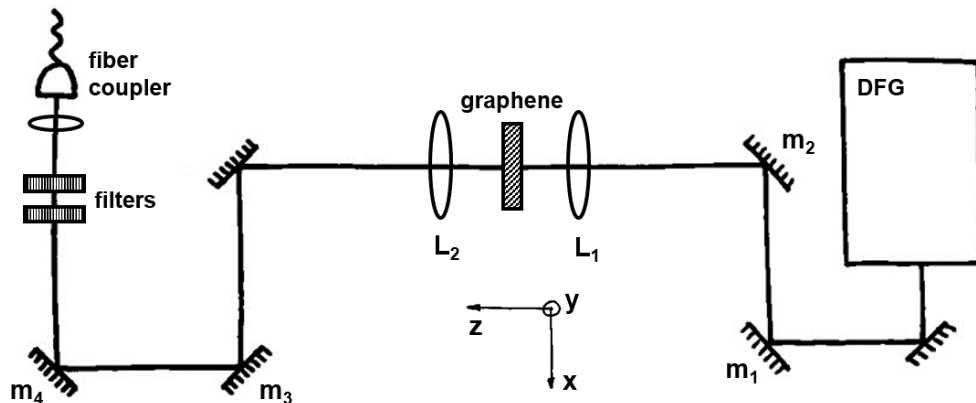


**Figure 6.7. Alignment procedure step 3.** After setting the lenses, you need to couple the light into a multi-mode fiber. Use mirrors  $m_3$  and  $m_4$  to walk the beam into the fiber coupler. Use the x-y-z degrees of freedom of the coupling lens to further optimize the coupling. Spectral filters will clear the desired wavelength from leakage light from the MIRA pump, and signal and idler beams of the OPO.

again, I recommend closing  $p_4$  as tight as possible and maximizing the power at the other side of the pinhole by changing the x and y positions of  $L_2$ , together with the translation in z. Do the same thing with  $p_4$  at a further distance. Remember that, experimentally, you will never achieve a perfectly collimated beam but the closest to that configuration will be when the beam waist is minimum at a very far distance; even a few meters away from  $L_2$ .

The third and last step is to couple the beam into a fiber. As shown in Fig. 6.7, you will need two mirrors,  $m_3$  and  $m_4$ , that will provide you with the necessary degrees of freedom. In addition to the spatial degrees, note that our fiber coupler has a movable coupling lens  $L_3$ , which means that the focal point, together with its position in y and z will also have to be optimized.

At this point the setup is ready to create and detect THG signals. Place the graphene sample on a x-y-z stage and in between  $L_1$  and  $L_2$ . If the lenses do not have the same focal lengths, determine the position of the focal point, which will not be in the middle of the lenses. Although it is more difficult to understand, in Fig. 6.8 I have added a real picture of the setup and sample to show how these look in reality.

Since we want to work at longer wavelengths, you can now switch to the idler beam at 1800 nm and optimize the coupling again. Note that whenever you change the wavelength, the beam walks off and both focusing and collimating distances will change. Thus, everytime you want to change the working wavelength, you need to optimize the collimation lens  $L_2$  and the coupling into the fiber. It is also worth mentioning that if you want to switch wavelengths by a large amount, you will have to do it step by step and always making sure that you do not completely lose the signal. If you lose it, unless you get lucky, you will have to start the

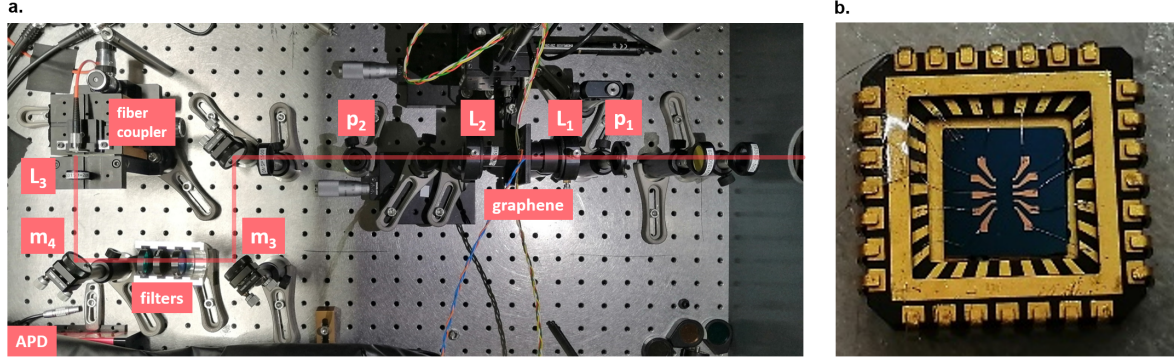


**Figure 6.8. Picture of the setup and sample.** **a.** Top view of the setup. The red line is a visual guide representing the laser beam that travels from right to left in the picture.  $p_1$  and  $p_2$  are the pinholes used for the initial alignment,  $L_1$  and  $L_2$  are the tight focusing and collimating lenses, respectively, and  $m_3$  and  $m_4$  are the mirrors to walk the beam and couple it into the multi-mode fiber. In this case, the collected signal is detected with an avalanche photodiode (APD). Note that all the optical components in the setup are standard parts from Thorlabs. **b.** Sample with gold nanoribbons. The visible gold pads correspond to the source and drain connections of the different graphene stripes shown in Fig. 6.9. These are connected one at a time, depending on the stripe that is being measured. On the other hand, the gate is shared.

alignment through  $p_1$  and  $p_2$ . Here are some of the spectral filter combinations (Thorlabs serial numbers) that might be useful to walk the beam towards longer wavelengths.

- $\lambda_{\text{pump}} = 2550 \text{ nm}$ ,  $\lambda_{\text{THG}} = 850 \text{ nm} \rightarrow \text{BP-850-10} + \text{BP-850-40} + \text{FESH1000}$
- $\lambda_{\text{pump}} = 3600 \text{ nm}$ ,  $\lambda_{\text{THG}} = 1200 \text{ nm} \rightarrow \text{BP-1200-10}$
- $\lambda_{\text{pump}} = 3900 \text{ nm}$ ,  $\lambda_{\text{THG}} = 1300 \text{ nm} \rightarrow \text{BP-1300-10} + \text{BP-1300-30}$

Once you have reached the desired wavelength you are ready to measure the TH signal of any sample. In our case we used the samples with gold nanoribbons built by the group of Frank Koppens at ICFO. As shown in Fig. 6.9, the gold nanoribbons are distributed in different arrays with different nanoribbon widths. The first step is to map the sample so that one knows where the nonlinear signal comes from. To do so, I recommend using the powermeter instead of the single-photon detector because it is faster and easier to use because you do not need to worry about the coupling. In this case, since the nanoribbons are all oriented in the same direction, they only absorb light polarized perpendicular to the nanoribbon orientation. Our incoming beam is already linearly polarized so you only need to rotate it with a half-wave plate (HWP).

After mapping the sample you first need to make sure that the detected signal corresponds to the TH signal that you are looking for. In order to distinguish the different contributions of the components in the sample, we proceed performing z-scans on the four different areas: substrate, substrate+gold, substrate+graphene and substrate+graphene+gold. In Fig. 6.10 we show the ideal result; that is, a very small contribution for both substrate and gold,

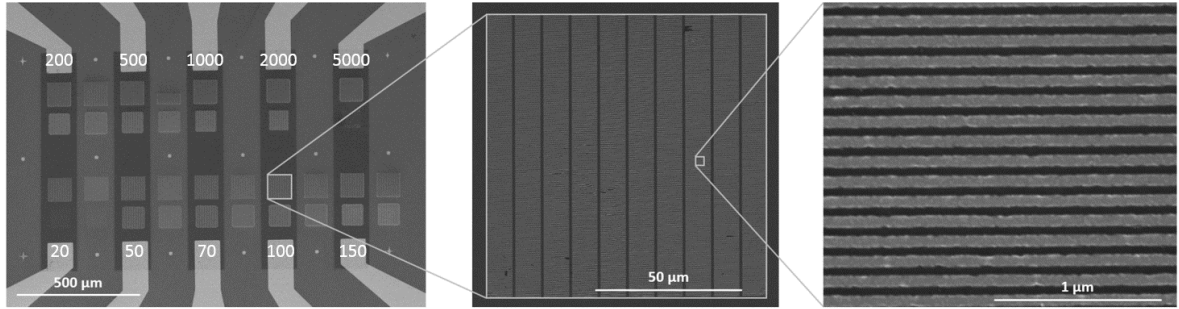


**Figure 6.9.** SEM images of the graphene with gold nanoribbon sample. The samples build by the group of Prof. Frank Koppens at ICFO have different arrays of nanoribbons with different widths, indicated in the image in nm units. The dark vertical stripes are the areas where there is graphene. There is a replica of the same kind of nanoribbon arrays with and without graphene in order to make reference measurements. On the right panel, the good quality of the nanoribbons can be appreciated.

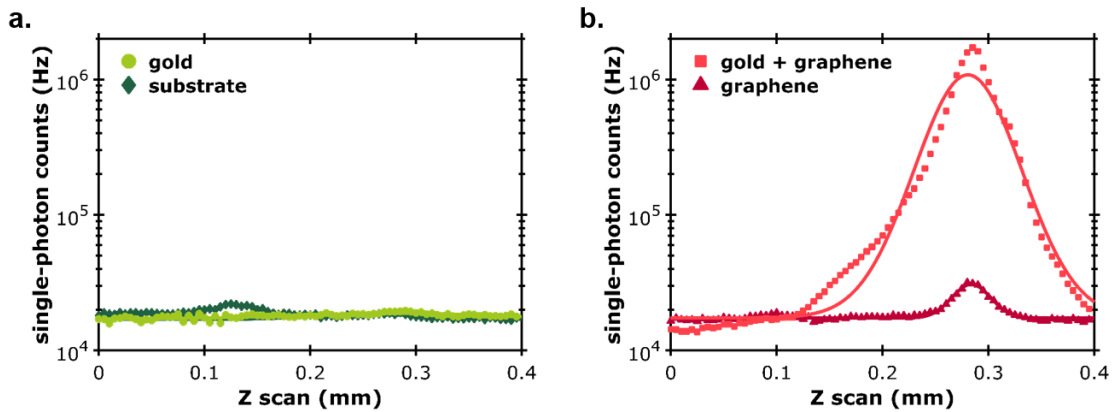


**Figure 6.10.** Sample component contributions to the TH signal. The sample allows us to study the individual contribution of each component of the sample. **a.** We find no nonlinear signal when there is only substrate or gold nanoribbons and **b.** shows a significant signal with bare graphene and an extremely enhanced signal when gold nanoribbons are added on top of the graphene. Note the logarithmic scales of the plots.

a noticeable signal from bare graphene and a hugely enhanced TH signal when the gold nanoribbons are on top of the graphene layer.

Among the different measurements that we have carried out, I would make a clear distinction between three types of measurements: enhancement characterization, where we quantify the signal enhancement provided by the gold nanoribbons; polarization measurements, where we confirm the cubic dependence of the TH signal on the pump beam, together with the copolarization between these; and gating measurements, where we apply a gate voltage to the sample in order to tune the Fermi energy  $E_F$  and observe the role of plasmon excitation in the THG process.

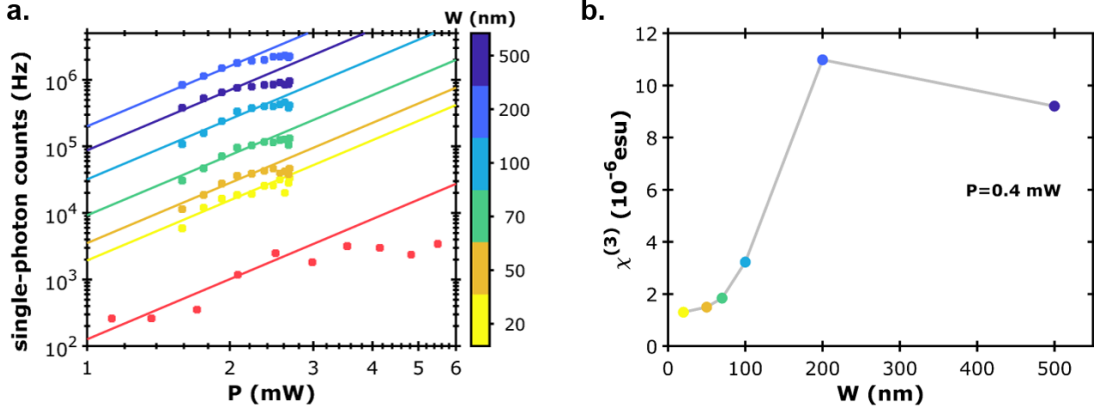


**Figure 6.11. TH signal enhancement quantification.** **a.** Power dependence of the TH for bare graphene (red) and graphene with gold nanoribbons of different widths (yellow through blue). The interception points found with the fits, whose slopes are set to 3, enable calculating the enhancement of the signals due to the field confinement. In the case of THG, the maximum enhancement is 1580 for  $W = 200$  nm. **b.** Calculated  $\chi^{(3)}$  for different nanoribbon widths with input power  $P = 0.4$  mW.

### Enhancement

We calculate the enhancement of the nanoribbons for different widths by measuring the TH signal as a function of the input power. As expected, the TH signal dependence on the pump is cubic. To verify this, we plot the data on a logarithmic scale and fit a line to it, where we fix the slope to 3 and keep the interception point as a free parameter (see Fig. 6.11a). Comparing the values of the nanoribbon interception points with the one from bare graphene, we find the enhancement factors. In Fig. 6.11b, we can clearly see that the signal enhancement depends on the nanoribbon width and that the optimal is at  $W \sim 200$  nm. The conversion from the observed TH signal in photon counts to the  $\chi^{(3)}$  value is calculated following the supplementary information in [45] and it is further detailed in the Methods section in our paper presented in Section 7.3.

### Polarization

For the polarization study, we change the input polarization with a HWP and a polarizer, and make sure that the input power is constant. As shown in Fig. 6.12a, the THG signal from graphene (red triangles) is isotropic and shows no dependence on the input polarization. On the contrary, when the gold nanoribbons take part (blue squares), there is a  $\cos^6 \theta$  dependence on the input polarization angle  $\theta$ . This is due to the cubic dependence of the TH process on the input power.

In the measurement shown in Fig. 6.12b, we check the polarization of the TH signal with respect to the input polarization. To do so, we fix the input power and polarization and rotate

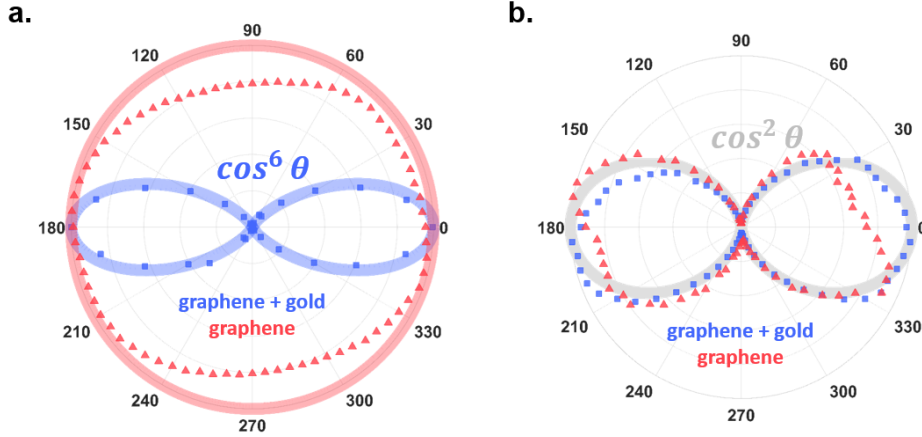


**Figure 6.12. Study of the input and output polarization.** **a.** When rotating the polarization of the input light, as theoretically predicted, bare graphene is isotropic to the incident polarization while the gold nanoribbons impose a  $\cos^6 \theta$  dependence for TH, maximizing the signal when the incident light is perpendicular to the direction of the nanoribbons. **b.** Changing the output polarization while keeping the input polarization fixed shows that the pump and TH signals are copolarized. The discrepancies between the theory and data are due to the polarization-dependent efficiency of the SNSP detectors.

the output polarization with a HWP. As expected, the data confirms that the input pump and the output TH signal are indeed copolarized. Note that the disagreement of the data with the theoretical prediction is due to the polarization-dependent efficiency of the SNSP detectors.

### Gating

Gating measurements are technically more challenging because there is a gate voltage that one needs to apply to the sample in order to be able to tune the Fermi energy  $E_F$ . Precisely, we need three electrical connections to the sample. We apply a small current ( $\sim 10^{-7}$  A, 1 mV) between the source and drain and monitor the resistance of graphene as  $E_F$  is changed. The maximum resistance corresponds to the Dirac point, where  $E_F = 0$ . The actual change of  $E_F$  is carried out by the gate voltage applied between the graphene and the substrate. A way of understanding this is by picturing a capacitor defined by the conductive graphene and Si layer, with the dielectric  $SiO_2$  in between.

The samples that we measured could be gated in the  $\pm 200$  V range, which was equivalent to  $E_F = \pm 0.5$  eV. In this gating measurements we were interested in observing the single-, two- and three-photon transition resonances and the shift of these resonance energies when changing the pump wavelength (see Fig. 6.13a). We also performed the same measurements on graphene with nanoribbons. In Fig. 6.13b and c we show the results for nanoribbon width and gap of ( $W = 55$  nm,  $g = 45$  nm) and ( $W = 47$  nm,  $g = 53$  nm), respectively. In

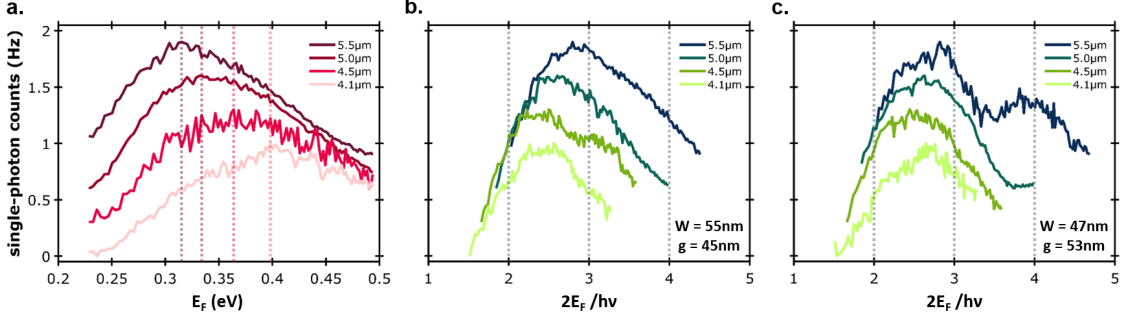


**Figure 6.13. Fermi energy tuning via electrical doping.** **a.** TH signal as a function of the Fermi energy  $E_F$  tuned by an applied gate voltage. When the  $E_F$  increases, the TH signal increases as it matches the single-, two- and three-photon transitions. As expected, these resonances shift with the input wavelength. **b.** and **c.** show TH signal gating measurements for nanoribbon arrays with widths  $W = (55 \text{ nm}, 47 \text{ nm})$  and gap between nanoribbons  $g = (45 \text{ nm}, 53 \text{ nm})$ , respectively. Apart from the large modulation due to the single-, two- and three-photon transition resonances, there are some additional signal variations that can be explained by the excitations of plasmons in graphene.

some of the measurements it is possible to see that, apart from the single-, two- and three-photon resonances, the TH signal has some characteristic modulations. According to the simulations developed by the group of Frank Koppens at ICFO, these variations of the TH signals are explained by the excitation of plasmons. Although we would initially expect a plasmon excitation to enhance the TH signal, the short lifetime of these plasmons ( $\sim 25 \text{ fs}$ ) makes them manifest as a dip in the signal. A handwavy explanation of this phenomenon is that when a short lifetime plasmon is excited, the absorption increases because the input beam is resonant with this transition but the nonradiative decay channels are stronger than the lifetime of the plasmon. Therefore, the TH signal is not radiated and we observe a dip in the signal. More details on this matter can be found in our paper in Section 7.3.



# Chapter 7

## Publications

### Published

- **I. Alonso Calafell**, T. Strömberg, D. R. M. Arvidsson-Shukur, L. A. Rozema, V. Saggio, C. Greganti, N. C. Harris, M. Prabhu, J. Carolan, M Hochberg, T. Baehr-Jones, D. Englund, C. H. W. Barnes and P. Walther, Genuine Counterfactual Communication with a Nanophotonic Processor, *npj Quantum Information*, **5**, 61 (2019).
- **I. Alonso Calafell**, J. D. Cox, M. Radonjić, J. R. M. Saavedra, F. J. García de Abajo, L. A. Rozema and P. Walther, Quantum Computing with Graphene Plasmons, *npj Quantum Information*, **5**, 37 (2019).
- C. Greganti, P. Schiansky, **I. Alonso Calafell**, Lorenzo M. Procopio, Lee A. Rozema and Philip Walther, Tuning single-photon sources for telecom multi-photon experiments, *Optics Express*, **26(3)**, 3286-3302 (2018).
- L. M. Procopio, A. Moqanaki, M. Araújo, F. Costa, **I. Alonso Calafell**, E. G. Down, D. R. Hamel, L. A. Rozema, C. Brukner and P. Walther, Experimental superposition of orders of quantum gates, *Nature Communications*, **6**, 7913 (2015).

### Pending

- **I. Alonso Calafell**, L. A. Rozema , D. Alcaraz Iranzo , A. Trenti , J. D. Cox , A. Kumar , H. Bieliaiev , S. Nanot , C. Peng , D. Efetov , J. Y. Hong , J. Kong , D. R. Englund , F. J. García de Abajo , F. H. L. Koppens , P. Walther, *Giant enhancement of third-harmonic generation in graphene-metal heterostructures*, under review (2020).
- **I. Alonso Calafell**, L. A. Rozema, A. Trenti , P. Jenke, J. Bohn, D. Alcaraz Iranzo, J. D. Cox, F. J. García de Abajo , F. H. L. Koppens , P. Walther, *High-harmonic generation enhancement with graphene heterostructures*, in preparation (2020).

## 7.1 Quantum computing with graphene plasmons

Current photonic quantum computing faces two main drawbacks: the probabilistic nature of the available single-photon sources and logic gates. The lack of these deterministic processes limits the scalability and universality of photonic quantum computation. In this article, we introduce a square-root of SWAP gate, which, as discussed in Chapter 5, is a universal gate, based on a directional coupler built with graphene nanoribbons as waveguides and plasmons as qubits. In such devices, with two input and two output ports, when a single indistinguishable plasmon is inserted in each of the input ports, the Hong-Ou-Mandel (HOM) [39] effect leads to a bunching effect at the output ports, in a way that both plasmons are always found at the same output port.

Here we take advantage of the Zeno effect, which alters the evolution of the system when a loss channel is added to the system. More precisely, the strong third-order nonlinearity in graphene provides a strong two-plasmon absorption rate, which acts as the loss channel in the Zeno effect.

For further understanding this topic, I recommend reading Sections 3.1-Surface Plasmon Polaritons and 5-Fundamentals of Quantum Computing; in particular 5.2-Quantum logic gates and 5.4-The Zeno effect.

## ARTICLE OPEN

## Quantum computing with graphene plasmons

I. Alonso Calafell<sup>1</sup>, J. D. Cox<sup>2</sup>, M. Radonjić<sup>1,4</sup>, J. R. M. Saavedra<sup>2</sup>, F. J. García de Abajo<sup>1,2,3</sup>, L. A. Rozema<sup>1</sup> and P. Walther<sup>1</sup>

Among the various approaches to quantum computing, all-optical architectures are especially promising due to the robustness and mobility of single photons. However, the creation of the two-photon quantum logic gates required for universal quantum computing remains a challenge. Here we propose a universal two-qubit quantum logic gate, where qubits are encoded in surface plasmons in graphene nanostructures, that exploits graphene's strong third-order nonlinearity and long plasmon lifetimes to enable single-photon-level interactions. In particular, we utilize strong two-plasmon absorption in graphene nanoribbons, which can greatly exceed single-plasmon absorption to create a "square-root-of-swap" that is protected by the quantum Zeno effect against evolution into undesired failure modes. Our gate does not require any cryogenic or vacuum technology, has a footprint of a few hundred nanometers, and reaches fidelities and success rates well above the fault-tolerance threshold, suggesting that graphene plasmonics offers a route towards scalable quantum technologies.

npj Quantum Information (2019)5:37; <https://doi.org/10.1038/s41534-019-0150-2>

## INTRODUCTION

Quantum computing could efficiently solve many essential problems. However, building a quantum computer is not an easy task. One particularly promising approach is to use single-photons, whose weak interaction with the environment makes them perfectly suitable for encoding and transmitting quantum information. Nonetheless, this weak interaction strength makes the implementation of photon-photon interactions a significant challenge. While this can be overcome at the cost of extra photons,<sup>1</sup> the additional overhead makes purely linear-optical schemes difficult to scale up.<sup>2</sup> Alternatively, single-photon-level nonlinearities can be used to directly create deterministic gates.<sup>3</sup> However, this typically requires complex interactions with atomic systems that cannot readily be miniaturized. Recent work shows that graphene can provide a strong enough nonlinearity without the technical drawbacks of those atomic systems.

Our graphene-based two-qubit logic gate is centered on Franson's quantum Zeno gate,<sup>4</sup> which is a universal "square-root-of-swap" (SWAP<sup>1/2</sup>) gate.<sup>5</sup> If two separable single-qubit states  $|\phi\rangle$  and  $|\psi\rangle$  enter modes 1 and 2, respectively, the gate creates an entangled superposition of these states being swapped and not swapped, i.e.,

$$|\phi\rangle_1|\psi\rangle_2 \rightarrow \frac{1}{\sqrt{2}}(|\phi\rangle_1|\psi\rangle_2 + |\psi\rangle_1|\phi\rangle_2), \quad (1)$$

where the subscripts indicate the mode. As illustrated in Fig. 1a, such an operation can be achieved by sending two photons to a 50:50 beamsplitter (BS): The gate succeeds when the two photons exit in different modes, generating the state of Eq. (1), while, half of the time, the gate will fail by allowing both photons to exit the same mode (in reality, the situation is even more complicated because of two-particle interference effects and the logical qubit encoding).

If the SWAP process is made continuous by replacing the 50:50 beamsplitter with coupled waveguides, the quantum Zeno effect<sup>6</sup> (wherein continuous measurement prevents a quantum system from evolving), can boost the success probability of the gate to 100%.<sup>4</sup> In this scenario, however, the quantum Zeno effect requires nonlinear two-photon absorption to occur at the single-photon-level. To date, such a strong optical nonlinearity has only been achieved via complex interactions with atomic systems,<sup>7</sup> which lack scalability.

Plasmon-polaritons, formed when light hybridizes with the collective charge-carrier density oscillations in conducting materials, confine electromagnetic energy to deeply-subwavelength scales, and could potentially enable extremely strong optical nonlinearities in nanoscale photonic circuits<sup>8</sup>—an ideal situation for a scalable quantum logic gate. While plasmons supported by noble metals provide large nonlinear enhancements and are compatible with single-photon-level quantum experiments,<sup>9,10</sup> they suffer from intrinsically high ohmic losses, severely limiting their application to quantum technologies.

Graphene has recently arisen as a robust material platform for plasmonics, capable of sustaining plasmon resonances with extremely long lifetimes<sup>11,12</sup> that can be tuned actively via electrostatic gating.<sup>13</sup> Furthermore, its low-dimensionality provides unprecedented levels of optical field confinement,<sup>14</sup> boosting optical nonlinearities well above those in noble metals,<sup>15–18</sup> potentially enabling nonlinearities on the single- or few-plasmon level.<sup>19,20</sup> Here we propose that this system can be used to implement a two-qubit quantum logic gate using nanoplasmonic graphene waveguides.

We will use the so-called single-rail encoding, just as in the original Zeno-gate proposal,<sup>4</sup> where the absence of a particle represents a logical 0, and the presence of a particle a logical 1. In other words,  $|0\rangle$  ( $|1\rangle$ ) in the Fock basis represents a logical  $|0\rangle$  ( $|1\rangle$ )

<sup>1</sup>Vienna Center for Quantum Science and Technology (VCQ), Faculty of Physics, University of Vienna, Boltzmanngasse 5, Vienna A-1090, Austria; <sup>2</sup>ICFO-Institut de Ciències Fotòniques, The Barcelona Institute of Science and Technology, 08860 Castelldefels, Barcelona, Spain; <sup>3</sup>ICREA-Institució Catalana de Recerca i Estudis Avançats, Passeig Lluís Companys 23, 08010 Barcelona, Spain; <sup>4</sup>Present address: Scientific Computing Laboratory, Center for the Study of Complex Systems, Institute of Physics Belgrade, University of Belgrade, Belgrade, Serbia  
Correspondence: I. Alonso Calafell (irati.alonso.calafell@univie.ac.at)

Received: 11 October 2018 Accepted: 9 April 2019  
Published online: 02 May 2019

Published in partnership with The University of New South Wales

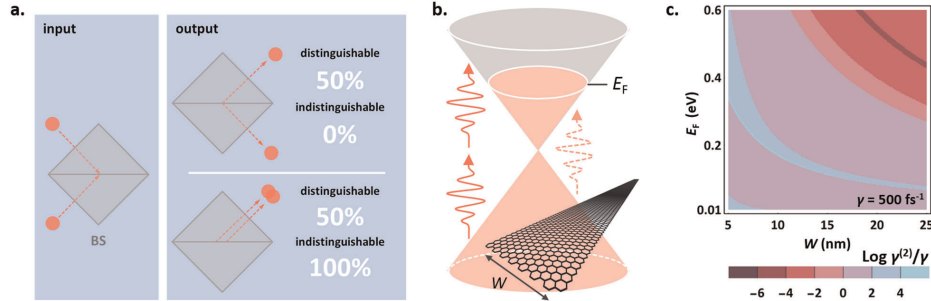


**Fig. 1** Basic operating principles of our nanoplasmonic quantum logic gate. **a** Simplest square-root-of-swap gate. Two photons are sent in the two ports of a 50:50 beamsplitter. If the photons are distinguishable, half of the times the photons exit from different ports and a square-root-of-swap gate is achieved. The other half of the times the two photons exit through the same port and the gate fails. If the photons are indistinguishable, they bunch and always exit from the same port, so the gate always fails. **b** Electronic band structure of graphene with a non-zero Fermi energy  $E_F$ . Two photons can produce an interband transition and be absorbed, whereas single-photon absorption is forbidden for photon energies below  $2E_F$ . **c** Ratios between the two-plasmon absorption rate,  $\gamma^{(2)}$  (at the plasmon resonance frequency), and the intrinsic damping rate,  $\gamma = 500 \text{ fs}^{-1}$ , for a range of nanoribbon widths,  $W$ , and Fermi energies,  $E_F$ . The blue areas are regions in which two-plasmon absorption is two to six orders of magnitude faster than linear absorption, providing a strong  $\gamma^{(2)} \gg \gamma$  condition that leads to extremely high success probabilities for the gate

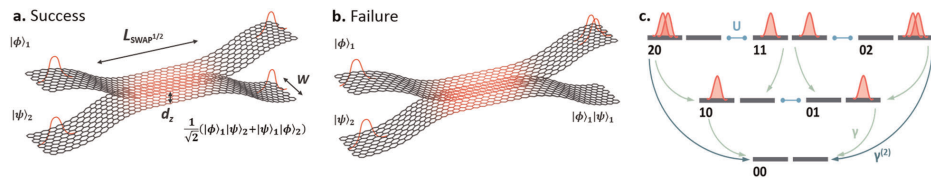


**Fig. 2** Surface-plasmon-based  $\text{SWAP}^{1/2}$  gate comprised of nonlinear graphene nanoribbons. Nanoribbons are brought together so that the plasmonic modes couple to each other via a Coulomb interaction. For a separation  $d_z$  between the ribbons, there is an interaction length  $L = L_{\text{SWAP}^{1/2}}$  after which the plasmon has 50-50% probability of remaining in the same mode or having swapped across ribbons. Thus, when a single plasmon is input in each mode,  $|1\rangle_1|1\rangle_2$ , we find the output state with **a** one plasmon in each mode,  $|1\rangle_1|1\rangle_2$ , in which case the gate succeeds, or **b** both plasmons in one of the modes,  $|2\rangle_1|0\rangle_2$  or  $|0\rangle_1|2\rangle_2$ , in which case the gate fails. When a separable single-qubit is input into each mode ( $|\phi\rangle, |\psi\rangle$ ), an entangled state is created,  $|\phi\rangle_1|\psi\rangle_2 \rightarrow \frac{1}{\sqrt{2}}(|\phi\rangle_1|\psi\rangle_2 + |\psi\rangle_1|\phi\rangle_2)$ . In the absence of nonlinearity in the waveguide and assuming indistinguishable plasmons, the HOM effect forces the plasmons to exit the gate in the same output mode, meaning that the gate always fails for  $|1\rangle_1|1\rangle_2$ . However, driven by the Zeno effect, the strong nonlinearity of the graphene waveguides reduces the probability that two plasmons are found in the same nanoribbon and increases the success probability. **c** We describe the  $\text{SWAP}^{1/2}$  gate as a six-state system where  $U$  is the coupling between ribbons, while  $\gamma$  and  $\gamma^{(2)}$  are the intrinsic damping and two-plasmon absorption rates, respectively

state of the qubit. Higher-order Fock states fall out of this logical subspace. Although the single-rail encoding has limitations,<sup>21</sup> it can be transformed into the more well-known dual-rail encoding with linear optical elements.<sup>22</sup>

Implementing the  $\text{SWAP}^{1/2}$  gate with a BS is not straightforward (Fig. 2a): If the logical input state is  $|00\rangle, |01\rangle$ , or  $|10\rangle$  (encoded by no particles in either mode, or one particle in the first or second, respectively), the gate functions perfectly. In contrast, when one particle is incident in each mode (a logical state  $|11\rangle$ ) the correct output is  $|11\rangle$ . Unfortunately, the Hong-Ou-Mandel (HOM) effect, already observed for single plasmons,<sup>9,10,23</sup> causes the particles to bunch and exit in the same mode, implying that the gate always fails. Since the HOM effect is independent of the relative phase between the two modes, this holds in general. Even if the particles are made indistinguishable, to circumvent HOM bunching, the gate fails 50% of the times (see Fig. 1a).

In a Zeno gate, the swap between the two modes has to be a continuous process, so that a “Zeno measurement” can be applied as the system evolves. Such a continuous swap can be achieved with a directional coupler (DC). To prevent the system from evolving into a state in which both particles are in the

same mode. In practice, the presence of a sufficiently strong two-photon absorber can perform this measurement.<sup>4</sup> At first glance, it appears that in such a DC, when the particles bunch into the same mode, they would be absorbed. However, when the swap probability is much smaller than the two-particle absorption, the Zeno effect does not even allow the particles to bunch in the first place.

In graphene, this Zeno condition can be easily achieved. When a single plasmon has less energy than the Fermi level, it is not absorbed via electron-hole pair excitation. At the same time, a mode containing two plasmon quanta can have enough energy to be absorbed via an interband transition (Fig. 1b). Since the two-plasmon absorption depends on the field strength while the single-plasmon absorption does not, confining the graphene plasmon field to a nanostructure enhances the two-plasmon absorption rate, while leaving the single-plasmon absorption rate unaffected<sup>20</sup> (Fig. 1c).

**RESULTS**

As a physical realization of such a graphene-based quantum gate, we envision a system of two graphene nanoribbons that support

propagating single plasmons (see Fig. 2). In this work we will assume that the single plasmons are already excited, which could, in principle, be achieved through the emission of a quantum light source.<sup>24–27</sup> The two nanoribbons are brought close to each other, so that the plasmons are coupled via Coulomb interaction, forming a graphene plasmon DC, whereby a plasmon starting in one ribbon can couple to the other ribbon. The interaction length, the ribbon width, and the ribbon spacing set the splitting ratio of the DC. At the same time, the ribbon width and the Fermi energy of the nanoribbons determine the two-plasmon absorption rate.

To model this system, we describe each ribbon as a two-level system with energy  $\hbar\omega$ , where  $\omega$  is the resonant plasmon frequency that depends on the nanoribbon width  $W$  and doping level (Fermi energy)  $E_F$ . As shown in Fig. 2c, we consider a maximum of two plasmons, limiting the Hilbert space to six states. States with an equal number of plasmons are coupled via a Coulomb interaction of strength  $U$ . Decay processes are governed by inelastic scattering rate  $\gamma$ , and  $\gamma^{(2)}$  denotes the two-plasmon absorption rate.

We quantify the Coulomb interaction by describing plasmons in semi-infinite graphene nanoribbons within the so-called plasmon wave function (PWF) formalism,<sup>28</sup> adapted here to include the effect of a non-vanishing optical wave vector  $k_{\parallel}$  in the direction of the ribbon transversal symmetry. Setting the nanoribbons to be aligned horizontally, and separated by a distance  $d_z$  in the  $z$ -direction (see Fig. 2a), the interaction between  $N$  plasmons in one ribbon and  $N'$  plasmons in the neighboring one, both of them propagating with parallel wave vector  $k_{\parallel}$ , is given by

$$U_{k_{\parallel}, NN'} = \frac{1}{2} \int d^2\mathbf{R} \int d^2\mathbf{R}' \frac{\left[ \rho_{k_{\parallel}, N}^{\text{ind}}(\mathbf{R}, \omega) \right]^* \rho_{k_{\parallel}, N'}^{\text{ind}}(\mathbf{R}', \omega)}{\sqrt{(\mathbf{R} - \mathbf{R}')^2 + d_z^2}}, \quad (2)$$

where the integrals are evaluated over the nanoribbons in a 2D space  $\mathbf{R} = (x, y)$  and  $\rho_{k_{\parallel}, N}^{\text{ind}}(\mathbf{R}, \omega)$  is the induced charge associated with  $N$  plasmons (see Methods and Fig. S1).

Next, we compute  $\gamma^{(2)}$  from the nonlinear conductivity  $\sigma_{\omega}^{(3)}$ , for which an analytical expression in the local and zero-temperature approximation is obtained quantum-mechanically in the Dirac cone approximation and reported in ref.<sup>29</sup> As shown in the Methods, the two-plasmon absorption rate is given by

$$\gamma^{(2)} = \frac{\hbar\omega\beta_{q,1}^{(4)}}{W\beta_{q,1}^{(2)}\Delta} \left( \frac{\gamma}{\text{Re}\{\sigma_{\omega}^{(1)}\}} \right)^2 \text{Re}\{\sigma_{\omega}^{(3)}\}, \quad (3)$$

where  $\beta_{q,1}^{(2)}$  and  $\beta_{q,1}^{(4)}$  are the momentum-dependent field normalizations, which we consider to be unity for low momentum values. Here  $\Delta$  characterizes the spatial extent of the propagating plasmon along the direction of transversal symmetry, which we set to be equal to the ribbon width. We set the single-plasmon lifetime to be  $\gamma = 500 \text{ fs}^{-1}$ , which is a realistic value, measured at room temperature.<sup>11</sup> Note that this lifetime can be extended by going to cryogenic temperatures; for which lifetimes up to 10 ps have recently been measured.<sup>12</sup>

We can now calculate the density matrix  $\rho(t)$  of the system by solving the time-dependent Lindblad master equation, which is the most general type of Markovian and time-homogeneous master equation describing an open-quantum-system evolution that is both trace-preserving and completely positive for any initial condition<sup>30</sup>

$$\dot{\rho} = -\frac{i}{\hbar} [H, \rho] + \sum_{n,m=1,2} \gamma^{(n)} \left( a_m^n \rho a_m^{\dagger n} - \frac{1}{2} \{ a_m^n a_m^n, \rho \} \right), \quad (4)$$

where  $\gamma^{(1)} \equiv \gamma$ ,  $a_m^{\dagger}$  ( $a_m$ ) denote plasmon creation (annihilation) operators,  $n$  is the number of absorbed plasmons and  $m$  is the nanoribbon mode. The Hamiltonian of the two-nanoribbon

system is

$$H = \hbar\omega \sum_{m=1,2} a_m^{\dagger} a_m + U(a_1^{\dagger} a_2 + a_2^{\dagger} a_1) \quad (5)$$

where  $U$  is the Coulomb interaction given in Eq. (2), while  $\omega$  is the plasmon frequency of each nanoribbon mode.

We numerically solve Eq. (4) using *Mathematica*, from which we obtain the required time  $t_{\text{SWAP}^{1/2}}$  at which a single plasmon incident in either nanoribbon is placed in an equal superposition of both nanoribbon modes at the output. This time is related to the Coulomb interaction  $U$  from Eq. (2) (i.e. stronger Coulomb interaction  $U$  resulting in shorter  $t_{\text{SWAP}^{1/2}}$ ). To calculate  $t_{\text{SWAP}^{1/2}}$  we define our initial state to be  $\rho(t=0) = |\psi_i\rangle\langle\psi_i|$ , where  $|\psi_i\rangle = |1\rangle_1 |0\rangle_2$ , and let it evolve until the probability of the plasmon being in either of the modes is equal:  $P_{10}(t_{\text{SWAP}^{1/2}}) = P_{01}(t_{\text{SWAP}^{1/2}})$ . We convert this time to a length  $L_{\text{SWAP}^{1/2}}$ , by computing the plasmon group velocity as shown in Fig. S2. The resulting  $L_{\text{SWAP}^{1/2}}$  is plotted in Fig. 3a. For  $E_F > 0.1 \text{ eV}$  the required  $L_{\text{SWAP}^{1/2}}$  is always less than the single-plasmon decay length, thus showing the potential of long-lived graphene plasmons: novel physical effects can manifest before the plasmon decays.

For all the results presented here, we set the spacing between the two nanoribbons to  $d_z = 1 \text{ nm}$ . With current technology, such atomically thin spacings can be realized by taking advantage of 2D materials like graphene.<sup>31</sup> This parameter only affects the Coulomb interaction strength, which will determine  $L_{\text{SWAP}^{1/2}}$ . The PWF used in our calculations is applicable for these scales, as discussed in detail in ref.<sup>28</sup>. Furthermore, for our parameter regime, the Coulomb interaction does not depend very strongly on  $d_z$  (see Fig. S4 of the Supplementary Information).

Once  $L_{\text{SWAP}^{1/2}}$  is determined, we proceed to analyze the system when a single plasmon is input in each mode; that is,  $\rho(t=0) = |\psi_i\rangle\langle\psi_i|$  where  $|\psi_i\rangle = |1\rangle_1 |1\rangle_2$ . For this input, the gate functions correctly if there is still one plasmon in each output mode, which occurs with probability  $P_{11}(t_{\text{SWAP}^{1/2}})$ .

## DISCUSSION

In Fig. 3a–c we show the success probability  $P_{11}(t_{\text{SWAP}^{1/2}})$ , the probability of the plasmons bunching in the same nanoribbon  $P_{20}(t_{\text{SWAP}^{1/2}}) + P_{02}(t_{\text{SWAP}^{1/2}})$ , and the probability for both plasmons to decay  $P_{00}(t_{\text{SWAP}^{1/2}})$ , for a range of nanoribbon widths  $W$  and Fermi energies  $E_F$ . Notice the similarity of the contour features between these figures and the  $\gamma^{(2)}/\gamma$  ratio shown in Fig. 1c. In the upper right corner the two-plasmon absorption is much weaker than the single-plasmon absorption, leading to a very weak Zeno effect, so the HOM effect prevails: that is,  $P_{20}(t_{\text{SWAP}^{1/2}}) + P_{02}(t_{\text{SWAP}^{1/2}}) \gg P_{11}(t_{\text{SWAP}^{1/2}})$ .

As we decrease both  $W$  and  $E_F$ ,  $\gamma^{(2)}$  increases, but not enough to drive a noticeable Zeno effect. Instead, both of the plasmons are likely to be absorbed, which is reflected in  $P_{00}(t_{\text{SWAP}^{1/2}}) \gg P_{20} + P_{02}(t_{\text{SWAP}^{1/2}})$ .

In the region where  $\gamma^{(2)}/\gamma \sim 10^4 - 10^6$ , a strong Zeno effect can be realized (light blue area of Fig. 1c). This leads to a large increase in the success probability  $P_{11}(t_{\text{SWAP}^{1/2}})$ , while  $P_{20} + P_{02}(t_{\text{SWAP}^{1/2}})$  becomes negligible, meaning that the Zeno effect completely suppresses the HOM effect. Despite the large  $\gamma^{(2)}$ ,  $P_{10}(t_{\text{SWAP}^{1/2}})$  shows a minimum when  $\gamma^{(2)} \gg \gamma$ . In this optimal region, we find a maximum success probability of 87.0% for  $W = 5 \text{ nm}$  and  $E_F = 0.335 \text{ eV}$ , which is an increase in the success probability of the SWAP<sup>1/2</sup> gate from 0 to 87.0%. This already places us well above the gate success probability rate required to generate universal cluster states for quantum computation.<sup>32</sup> This performance is limited by the single plasmon lifetime. In Fig. 3e we plot the success probability, maximized over the range of  $W$  and  $E_F$  shown in panels a–d, versus the plasmon lifetime given by  $1/\gamma$ . For lifetimes longer than 7.5 ps the success probability

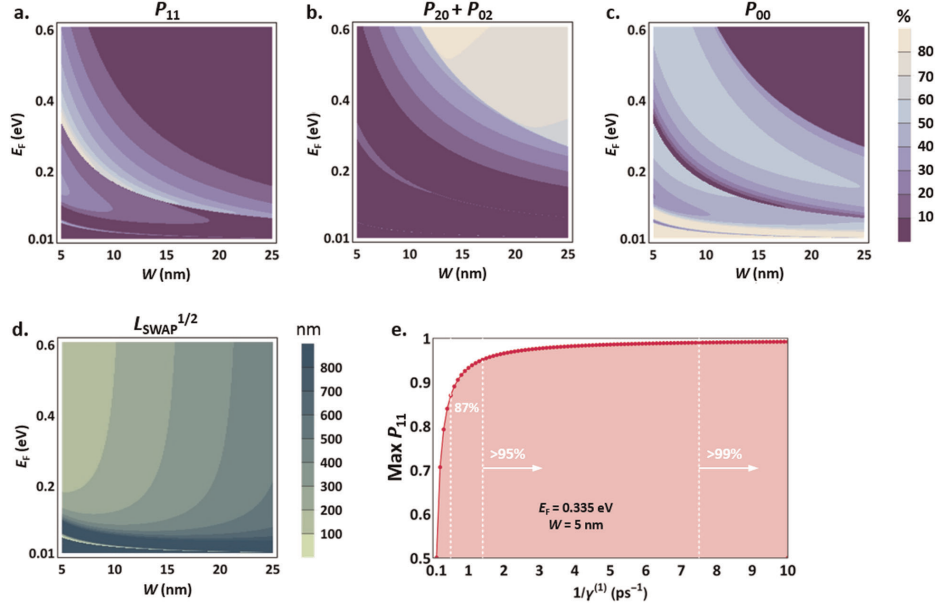


**Fig. 3** Performance of the graphene-based  $\text{SWAP}^{1/2}$  for different nanoribbon width  $W$  and Fermi energy  $E_F$ . Here the separation between the nanoribbons is set to  $d_z = 1$  nm, and the in plane momentum along the ribbon to  $k_{||}W = 0.4$ . **a** Probability of still having one plasmon in each mode when one plasmon is input into each mode after the input plasmons evolve along the interaction length  $L_{\text{SWAP}^{1/2}}$ . We find a range (shown in white) where the success probability is over 80% for reasonable physical parameters. **b** Probability of finding two plasmons in one nanoribbon after the interaction between the initial plasmons occurs. This is the “failure probability” of the gate, as it corresponds to events which take us out of the logical qubit subspace. As expected, these data show that in the region where  $P_{11}$  is maximized the failure probability is significantly suppressed. **c** Probability of losing both initial plasmons after they evolve along a distance  $L_{\text{SWAP}^{1/2}}$ . **d** Interaction length  $L_{\text{SWAP}^{1/2}}$  required to perform the  $\text{SWAP}^{1/2}$  logic gate. For the plotted range, we find that, above  $E_F = 0.1$  eV, the required interaction length is always shorter than the plasmon decay length (which is  $\approx 500$  nm for a 500 fs lifetime). **e** Success probability of the  $|11\rangle$  input state as a function of the plasmon lifetime  $1/\gamma$ , maximized over the same  $W$  and  $E_F$  range as in panels **a–c**

increases above 99%, reaching fault-tolerance regimes for surface codes.<sup>33</sup> Nevertheless, edge imperfections and structural defects would decrease the plasmon lifetime and thus the fidelity of the gate. The predicted nonlinearities, nevertheless, should persist in their presence.

Since single-plasmon decay can also result in logical states changing into other logical states, this process fidelity will be further decreased. To quantify this, we evaluated the process fidelity<sup>34,35</sup> of our gate by simulating process tomography for the complete range of  $W$  and  $E_F$  under consideration (see Methods). The resulting process matrix for  $W = 5$  nm and  $E_F = 0.335$  eV with a lifetime of 500 fs is plotted in Fig. 4, and has a fidelity of 93.3%. When the lifetime is increased to 10 ps, the fidelity is 99.6%.

Our proposed gate achieves process fidelities in the fault-tolerance regime for relatively reasonable physical parameters. Doping levels as high as 1–2 eV have been achieved,<sup>36,37</sup> nanoribbon widths in the range of 10–40 nm have been constructed using different means,<sup>31,38–40</sup> and separation distances  $\approx 1$  nm are routinely achieved through single-atomic hexagonal boron nitride spacers, which additionally guarantees the preservation of high-quality graphene optical response.<sup>31</sup> Furthermore, by combining ideas from quantum optics with nanoplasmonics, our work opens up an entirely new and promising avenue in the search for single-photon nonlinearities. While we have studied the application of graphene nanoplasmonics to a quantum logic gate, this could also be used for deterministic optical implementations

of quantum teleportation,<sup>41</sup> cluster state generation,<sup>42</sup> and single-photon sources,<sup>19</sup> underlining the applicability of this platform.

## METHODS

### Classical electrostatic description of plasmons in graphene nanoribbons

We consider a single graphene nanoribbon occupying the  $\mathbf{R} = (x, y)$  plane that has a finite width  $W$  in the  $x$ -direction and is infinitely-extended along the  $y$ -direction. In the linear approximation, following refs.,<sup>19,23</sup> the self-consistent electric field within the ribbon  $\mathbf{E}_q$  produced by an impinging field  $\mathbf{E}^{\text{ext}}(\mathbf{R}, t) = \mathbf{E}_q^{\text{ext}} e^{i(k_y y - \omega t)} + \text{c.c.}$ , i.e., having frequency  $\omega$  and momentum  $k_y \equiv q/W$  along  $y$ , is given by

$$\mathbf{E}_q(\mathbf{R}, \omega) = \mathbf{E}_q^{\text{ext}}(\mathbf{R}, \omega) - \frac{1}{\epsilon_{\text{ab}}} \nabla_{\mathbf{R}} \int \frac{d^2 \mathbf{R}'}{|\mathbf{R} - \mathbf{R}'|} \rho_q^{\text{ind}}(\mathbf{R}', \omega), \quad (6)$$

where  $\epsilon_{\text{ab}} = (\epsilon_{\text{a}}^{\text{ab}} + \epsilon_{\text{b}}^{\text{ab}})/2$  is the average of the dielectric functions describing media above ( $\epsilon_{\text{a}}^{\text{ab}}$ ) and below ( $\epsilon_{\text{b}}^{\text{ab}}$ ) the 2D layer and  $\rho_q^{\text{ind}}(\mathbf{R}, \omega)$  is the induced charge. From the continuity equation, we express  $\rho_q^{\text{ind}}$  in terms of the local, linear 2D graphene conductivity  $\sigma_{\text{a}}^{(1)}$  as

$$\rho_q^{\text{ind}}(\mathbf{R}, \omega) = -\frac{i}{\omega} \sigma_{\text{a}}^{(1)} \nabla_{\mathbf{R}} \cdot [\mathbf{f}_{\text{b}} \mathbf{E}_q(\mathbf{R}, \omega)], \quad (7)$$

where we have introduced the occupation factor  $\mathbf{f}_{\text{b}}$ , which is equal to one when  $-W/2 \leq x \leq W/2$  and is vanishingly small everywhere else. In practice, we employ the optical conductivity obtained for zero temperature in the local limit (i.e., for vanishing in-plane optical momentum) of the random-

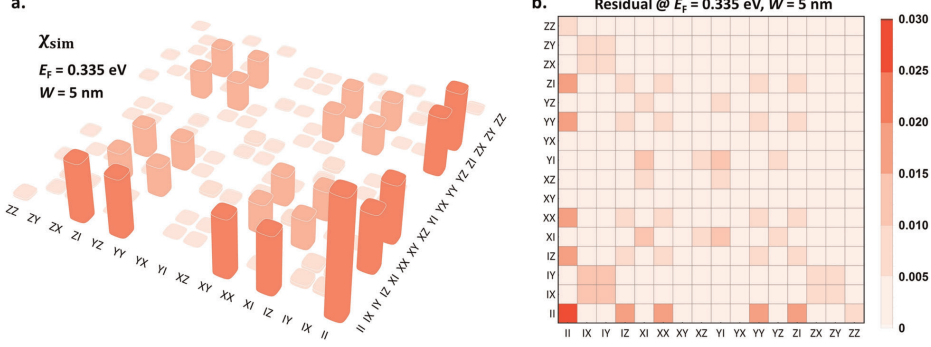


**Fig. 4** Process Matrix of the SWAP<sup>1/2</sup> gate based on graphene surface plasmons. **a** Simulated process matrix of the SWAP<sup>1/2</sup> gate at 93.3% process fidelity for  $W = 5$  nm and  $E_F = 0.335$  eV, with a lifetime of 500 fs. The axis label corresponds to the product of the Pauli operators used to construct the two-qubit basis, as defined in the Methods section. Note that we only plot the magnitude of the process matrix elements. **b** Residual between the simulated and ideal process matrices ( $\|X_{\text{ideal}} - X_{\text{sim}}\|$ ) at the point of maximum fidelity

phase approximation (RPA) as<sup>18</sup>

$$\sigma_{\omega}^{(1)} = \frac{ie^2}{\pi\hbar^2} \frac{E_F}{\omega + i\tau^{-1}} + \frac{e^2}{4\hbar} \left[ \Theta(\hbar\omega - 2E_F) + \frac{i}{\pi} \log \frac{\hbar\omega - 2E_F}{\hbar\omega + 2E_F} \right], \quad (8)$$

where the Fermi energy  $E_F$  is related to the graphene Fermi velocity  $v_F \approx c/300$ , doping charge-carrier density  $n$  according to  $E_F = \hbar v_F \sqrt{\pi n}$  and  $\tau = 1/\gamma$  is a phenomenological inelastic scattering rate. The first and second terms in Eq. (8) describe the optical response arising from intraband and interband electronic transitions, respectively, with the latter becoming unimportant when  $E_F \lesssim \omega$ .<sup>13</sup> Incidentally, we have neglected inelastic damping in the interband transitions. In terms of normalized coordinates  $\vec{\theta} \equiv \mathbf{R}/W$  and the normalized electric field  $\vec{\epsilon}_q(\vec{\theta}, \omega) \equiv W\sqrt{f_{\vec{\theta}}}\mathbf{E}_q(\vec{\theta}, \omega)$ , Eq. (6) can be expressed as

$$\vec{\epsilon}_q(\vec{\theta}, \omega) = \vec{\epsilon}_q^{\text{ext}}(\vec{\theta}, \omega) + \eta_{\omega}^{(1)} \int d^2\vec{\theta}' \mathbf{M}(\vec{\theta}, \vec{\theta}') \cdot \vec{\epsilon}_q(\vec{\theta}', \omega), \quad (9)$$

where  $\eta_{\omega}^{(1)} \equiv i\sigma_{\omega}^{(1)}/\epsilon_0^{\text{ab}}\omega W$  is a dimensionless parameter characterizing the intrinsic linear optical response of graphene, and

$$\mathbf{M}(\vec{\theta}, \vec{\theta}') = \sqrt{f_{\vec{\theta}}f_{\vec{\theta}'}} (\nabla_{\vec{\theta}} \otimes \nabla_{\vec{\theta}'}), \quad (10)$$

which we identify as a real, symmetric operator that admits a complete set of real eigenvalues. The electric field of Eq. (9) is expanded in eigenmodes of the matrix  $\mathbf{M}(\vec{\theta}, \vec{\theta}')$  as

$$\vec{\epsilon}_q(\vec{\theta}, \omega) = \sum_m a_m \vec{\epsilon}_{q,m}(\theta_x) e^{iq\theta_y}, \quad (11)$$

where the modes  $\vec{\epsilon}_{q,m}(\theta_x) e^{iq\theta_y}$  and their corresponding eigenvalues  $\eta_{q,m}$  satisfy

$$\vec{\epsilon}_{q,m}(\theta_x) e^{iq\theta_y} = \eta_{q,m} \int d^2\vec{\theta}' \mathbf{M}(\vec{\theta}, \vec{\theta}') \cdot \vec{\epsilon}_{q,m}(\theta'_x) e^{iq\theta'_y}, \quad (12)$$

and form an orthonormal set

$$\int d\theta_x \vec{\epsilon}_{q,m}^*(\theta_x) \cdot \vec{\epsilon}_{q,m}(\theta_x) = \delta_{mm'}. \quad (13)$$

Inserting Eq. (11) into Eq. (9), we make use of Eqs. (12 and 13) to write  $a_m = b_{q,m}(1 - \eta_{\omega}^{(1)}/\eta_{q,m})^{-1}$ , where

$$b_{q,m}(\theta_y) = \int d\theta_x \vec{\epsilon}_{q,m}^*(\theta_x) \vec{\epsilon}_q^{\text{ext}}(\vec{\theta}, \omega) \quad (14)$$

is a coefficient that depends on the form of the external field. In what follows we take  $\mathbf{E}_q^{\text{ext}}$  to be independent of  $x$ , so we may write  $b_{q,m}(\theta_y) = -W\mathbf{E}_q^{\text{ext}} \cdot \vec{\epsilon}_{q,m}^+ c_q(\theta_y)$ , where  $c_q(\theta_y)$  contains the  $y$ -dependence of the external field and  $\vec{\epsilon}_{q,m}^+ \equiv -\int d\theta_x \vec{\epsilon}_{q,m}(\theta_x)$ , so that the normalized

I. Alonso Calafell et al.

electric field in Eq. (11) becomes

$$\vec{\epsilon}_q(\vec{\theta}, \omega) = \sum_m \frac{-W\mathbf{E}_q^{\text{ext}} \cdot \vec{\epsilon}_{q,m}^+}{1 - \eta_{\omega}^{(1)}/\eta_{q,m}} \vec{\epsilon}_{q,m}(\theta_x) c_q(\theta_y). \quad (15)$$

Electrostatic energy in nanoribbons

The electrostatic energy for identical, parallel ribbons separated by a distance  $d_z$  in the  $z$ -direction is given by

$$U_{q,l,l'}(d_z) = \frac{W^3}{2} \int d^2\vec{\theta} \int d^2\vec{\theta}' \frac{[\rho_{q,l}^{\text{ind}}(\vec{\theta}, \omega)]^* \rho_{q,l'}^{\text{ind}}(\vec{\theta}', \omega)}{\sqrt{(\theta_x - \theta'_x)^2 + (\theta_y - \theta'_y)^2 + (d_z/W)^2}}, \quad (16)$$

where, from Eq. (7) (taking  $\epsilon_{\omega}^{\text{ab}} = 1$  for simplicity), we can express the induced charge in ribbon  $l$  as

$$\rho_{q,l}^{\text{ind}}(\vec{\theta}, \omega) = \frac{\eta_{\omega}^{(1)}}{W} \nabla_{\vec{\theta}} \cdot [\sqrt{f_{\vec{\theta}}}\vec{\epsilon}_{q,l}(\vec{\theta}, \omega)]. \quad (17)$$

Inserting the above expression into Eq. (16) and making use of Eq. (15), the electrostatic energy becomes

$$U_{q,l,l'}(d_z) = \frac{W^3}{2} \sum_{mm'} \left( \frac{E_{q,l}^{\text{ext}} \cdot \vec{\epsilon}_{q,m}^+}{1/\eta_{\omega}^{(1)} - 1/\eta_{q,m}} \right)^* \left( \frac{E_{q,l'}^{\text{ext}} \cdot \vec{\epsilon}_{q,m'}}{1/\eta_{\omega}^{(1)} - 1/\eta_{q,m'}} \right) I_{q,mm'}(d_z), \quad (18)$$

where

$$I_{q,mm'}(d_z) = \int_{-1/2}^{1/2} d\theta_x \int_{-L/2W}^{L/2W} d\theta_y \int_{-1/2}^{1/2} d\theta'_x \times \int_{-L/2W}^{L/2W} d\theta'_y \frac{[\nabla_{\vec{\theta}} \cdot \vec{\epsilon}_{q,m}(\theta_x, \theta_y)]^* [\nabla_{\vec{\theta}'} \cdot \vec{\epsilon}_{q,m'}(\theta'_x, \theta'_y)]}{\sqrt{(\theta_x - \theta'_x)^2 + (\theta_y - \theta'_y)^2 + (d_z/W)^2}} \quad (19)$$

and  $L \rightarrow \infty$  is the nanoribbon length.

Assuming a plane wave field profile along the  $y$ -direction corresponding to  $c_q(\theta_y) = e^{iq\theta_y}$ , in a single ribbon (i.e., taking  $l=l'$  and  $d_z=0$ ), the use of Eqs. (10) and (13) yields  $I_{q,mm}(0) = -L\delta_{mm'}/W\eta_{q,m}$  and so the electrostatic energy per unit length in ribbon  $l$  is

$$\tilde{U}_{q,l} = \frac{W^2}{2} \sum_m \frac{-1}{\eta_{q,m}} \left| \frac{E_{q,l}^{\text{ext}} \cdot \vec{\epsilon}_{q,m}^+}{1/\eta_{\omega}^{(1)} - 1/\eta_{q,m}} \right|^2. \quad (20)$$

In practice, we restrict our study to the lowest-order  $m=1$  mode, and fix the number of plasmon quanta in this mode using the condition  $\hbar\omega_p = 2\Delta\tilde{U}_{q,1}$ , where  $\Delta$  is an effective length for the plasmon mode along the ribbon (i.e., the characteristic spatial width of a pulse), leading to

$$\left| \frac{E_{q,1}^{\text{ext}} \cdot \vec{\epsilon}_{q,1}^+}{W^2\Delta} \right|^2 = -\frac{\hbar\omega\eta_{q,1}}{W^2\Delta} \left| \frac{1}{\eta_{\omega}^{(1)}} - \frac{1}{\eta_{q,1}} \right|^2, \quad (21)$$

where it is now understood that the indices  $l$  and  $l'$  denote the number of plasmons in the first and second ribbon, respectively. Using the above

condition, the coupling energy between ribbons containing  $l$  and  $l'$  plasmons is obtained directly from Eq. (18), again considering only the  $m = m' = 1$  contribution.

#### Plasmon normalization

We normalize the electric field amplitude of the plasmon mode by equating the absorbed and dissipated power at linear order, i.e.,

$$l\hbar\omega_p\gamma = \left\langle \int d^2\mathbf{R} \mathbf{j}_q^{(1)}(\mathbf{R}, t) \cdot \mathbf{E}_q(\mathbf{R}, t) \right\rangle, \quad (22)$$

where  $l$  is the number of plasmon quanta,  $\mathbf{j}_q^{(1)}(\mathbf{R}, \omega) = \sigma_\omega^{(1)} \mathbf{E}_q(\mathbf{R}, \omega)$ , and (...) denote the time-average. Using the result of Eq. (15) with only the  $m = 1$  mode, we obtain

$$l\hbar\omega_p\gamma = \frac{2W^2}{L} \text{Re}\{\sigma_\omega^{(1)}\} \left| \frac{\mathbf{E}_{q,l}^{\text{ext}} \cdot \bar{\mathbf{e}}_{q,1}^*}{1 - \eta_\omega^{(1)}/\eta_{q,1}} \right|^2 \int_{-L/2W}^{L/2W} d\theta_y |c_q(\theta_y)|^2, \quad (23)$$

where  $\beta_{q,1}^{(1)} = \int_{-1/2}^{1/2} d\theta_y \bar{\mathbf{e}}_{q,1}(\theta_y)$ . For a mode defined as a plane-wave along the ribbon, such that  $c_q(\theta_y) = e^{i\theta_y}$ , within an effective length  $\Delta$ , we write the normalization condition for  $N$  plasmons as

$$\left| \frac{\mathbf{E}_{q,l}^{\text{ext}} \cdot \bar{\mathbf{e}}_{q,1}^*}{\beta_{q,1}^{(1)}} \right|^2 = \frac{l\hbar\omega_p\gamma}{2W \text{Re}\{\sigma_\omega^{(1)}\} \beta_{q,1}^{(2)} \Delta} \quad (24)$$

#### Two-plasmon absorption rate

Power absorption in a nanoribbon via two-plasmon absorption arises from the nonlinear current  $\mathbf{j}^{(3)}(\mathbf{R}, t) = \hat{j}_q^{(3)}(\mathbf{R}, \omega) e^{i\theta_y - i\omega t} + \text{c.c.}$ , where  $\hat{j}_q^{(3)}(\mathbf{R}, \omega) = \sigma_\omega^{(3)} |\mathbf{E}_q(\mathbf{R}, \omega)|^2 \mathbf{E}_q(\mathbf{R}, \omega)$ , and is given by

$$P_{\text{TPA}} = \int d^2\mathbf{R} \hat{j}_q^{(3)}(\mathbf{R}, t) \cdot \mathbf{E}_q(\mathbf{R}, t), \quad (25)$$

where  $\hat{j}_q^{(3)}(\mathbf{R}, \omega) = \sigma_\omega^{(3)} |\mathbf{E}_q(\mathbf{R}, \omega)|^2 \mathbf{E}_q(\mathbf{R}, \omega)$  and  $\sigma_\omega^{(3)}$  is the local third-order conductivity of extended graphene, for which we adopt the analytical result obtained quantum-mechanically at zero temperature in the Dirac cone approximation, as reported in ref.<sup>29</sup> Using Eq. (15) we write the time-average of the absorbed power per unit length as

$$\langle P_{\text{TPA}} \rangle = \frac{2W^2}{L} \text{Re}\{\sigma_\omega^{(3)}\} \left| \frac{\mathbf{E}_{q,l}^{\text{ext}} \cdot \bar{\mathbf{e}}_{q,1}^*}{1 - \eta_\omega^{(1)}/\eta_{q,1}} \right|^4 \int_{-L/2W}^{L/2W} d\theta_y |c_q(\theta_y)|^4. \quad (26)$$

Equating  $\langle P_{\text{TPA}} \rangle$  with the power dissipated by two-plasmon absorption,  $2\hbar\omega\gamma^{(2)}$ , we make use of the field normalization condition in Eq. (24) to write the two-plasmon absorption rate for a ribbon containing  $l = 2$  plasmons in the  $m = 1$  mode as

$$\gamma^{(2)} = \frac{\hbar\omega\beta_{q,1}^{(4)}}{W\beta_{q,1}^{(2)}\Delta} \left( \frac{\gamma}{\text{Re}\{\sigma_\omega^{(1)}\}} \right)^2 \text{Re}\{\sigma_\omega^{(3)}\}. \quad (27)$$

In obtaining the above expression, we have again chosen the field along the ribbon to have the form of a plane-wave (i.e.,  $c_q(\theta_y) = e^{i\theta_y}$ ), and an effective length  $\Delta$ .

#### Process tomography

We send a complete set of 16 two-qubit states through our simulation and compute the output states at  $t_{\text{SWAP}^{1/2}}$ . To deal with failure events, when  $|2\rangle_1|0\rangle_2$  and  $|0\rangle_1|2\rangle_2$  terms arise in the output states, we truncate the output density matrix and renormalize the result. Such events only occur when states involving two plasmons are input. We also numerically correct for local single-qubit phases which arise in the output of the simulation. We feed these output states in a least-squares process tomography routine, generating a process matrix  $\chi_{\text{sim}}$ . This process matrix is defined as,

$$\rho_{\text{out}} = \sum_{m,n} \chi_{m,n} E_m^\dagger \rho_{\text{in}} E_m, \quad (28)$$

where  $\rho_{\text{in(out)}}$  is the input (output) density matrix, and  $E_i$  are the basis operators constructed from the Kronecker product of the Pauli matrices (labels of Fig. 4). We calculate the process fidelity between these, and the ideal process (given by Eq. (10) of ref.<sup>12</sup> as  $\text{Tr}\{\chi_{\text{sim}}\chi_{\text{ideal}}\}$ <sup>34,35</sup>

#### Numerical solution of the linblad master equation

We use the Lindblad equation introduced in Eq. (4) to describe and solve the density matrix of our system. The first term of the Lindblad equation contains the Hamiltonian given in Eq. (5). This Hamiltonian describes the two identical graphene nanoribbons as a two-level system, where the coupling between the levels is given by the Coulomb interaction  $U$ . We define a 6-state Hilbert space that contains a vacuum state  $(|0\rangle_1|0\rangle_2)$ , two single-plasmon states  $(|1\rangle_1|0\rangle_2, |0\rangle_1|1\rangle_2)$  and three two-plasmons states  $(|1\rangle_1|1\rangle_2, |2\rangle_1|0\rangle_2, |0\rangle_1|2\rangle_2)$ . In this basis, the matrix form of the Hamiltonian is

$$H = \begin{pmatrix} 0 & 0 & 0 & 0 & 0 & 0 \\ 0 & \hbar\omega & U & 0 & 0 & 0 \\ 0 & U & \hbar\omega & 0 & 0 & 0 \\ 0 & 0 & 0 & 2\hbar\omega & \sqrt{2}U & \sqrt{2}U \\ 0 & 0 & 0 & \sqrt{2}U & 2\hbar\omega & 0 \\ 0 & 0 & 0 & \sqrt{2}U & 0 & 2\hbar\omega \end{pmatrix}, \quad (29)$$

where  $\hbar\omega$  is the energy of the plasmon. The second term of the Lindblad equation contains the loss channels of the system; namely, the single-plasmon absorption  $\gamma^{(1)}$  and the two-plasmon absorption  $\gamma^{(2)}$ . In matrix form, this second term reduces to

$$H = \begin{pmatrix} \gamma^{(1)}(\rho_{0011} + \rho_{1010}) + \gamma^{(2)}(\rho_{0202} + \rho_{2020}) & \gamma^{(1)}(-\frac{1}{2}\rho_{0010} + \rho_{0111} + \sqrt{2}\rho_{1020}) & \gamma^{(1)}(-\frac{1}{2}\rho_{0001} + \rho_{0101} + \sqrt{2}\rho_{0102}) \\ \gamma^{(1)}(-\frac{1}{2}\rho_{1000} + \rho_{1101} + \sqrt{2}\rho_{2010}) & \gamma^{(1)}(-\rho_{0010} + \rho_{0111} + 2\rho_{2020}) & \gamma^{(1)}(-\rho_{0001} + \sqrt{2}(\rho_{1102} + \rho_{2011})) \\ \gamma^{(1)}(-\frac{1}{2}\rho_{0100} + \rho_{1110} + \sqrt{2}\rho_{2021}) & \gamma^{(1)}(-\rho_{0110} + \sqrt{2}(\rho_{0211} + \rho_{1120})) & \gamma^{(1)}(-\rho_{0101} + 2\rho_{0202} + \rho_{1111}) \\ -\gamma^{(1)}\rho_{1100} & -\frac{1}{2}\gamma^{(1)}\rho_{1110} & -\frac{3}{2}\gamma^{(1)}\rho_{1101} \\ -\frac{1}{2}(2\gamma^{(1)} + \gamma^{(2)})\rho_{2020} & -\frac{1}{2}(3\gamma^{(1)} + \gamma^{(2)})\rho_{2010} & -\frac{1}{2}(3\gamma^{(1)} + \gamma^{(2)})\rho_{2001} \\ -\frac{1}{2}(2\gamma^{(1)} + \gamma^{(2)})\rho_{0200} & -\frac{1}{2}(3\gamma^{(1)} + \gamma^{(2)})\rho_{0210} & -\frac{1}{2}(3\gamma^{(1)} + \gamma^{(2)})\rho_{0201} \end{pmatrix} \\ -\gamma^{(1)}\rho_{0011} & -\frac{1}{2}(2\gamma^{(1)} + \gamma^{(2)})\rho_{0020} & -\frac{1}{2}(2\gamma^{(1)} + \gamma^{(2)})\rho_{0002} \\ -\frac{3}{2}\gamma^{(1)}\rho_{1011} & -\frac{1}{2}(3\gamma^{(1)} + \gamma^{(2)})\rho_{1020} & -\frac{1}{2}(3\gamma^{(1)} + \gamma^{(2)})\rho_{1002} \\ -\frac{3}{2}\gamma^{(1)}\rho_{0111} & -\frac{1}{2}(3\gamma^{(1)} + \gamma^{(2)})\rho_{0120} & -\frac{1}{2}(3\gamma^{(1)} + \gamma^{(2)})\rho_{0102} \\ -2\gamma^{(1)}\rho_{1111} & -\frac{1}{2}(4\gamma^{(1)} + \gamma^{(2)})\rho_{1120} & -\frac{1}{2}(4\gamma^{(1)} + \gamma^{(2)})\rho_{1102} \\ -\frac{1}{2}(4\gamma^{(1)} + \gamma^{(2)})\rho_{2011} & -(2\gamma^{(1)} + \gamma^{(2)})\rho_{2020} & -(2\gamma^{(1)} + \gamma^{(2)})\rho_{2002} \\ -\frac{1}{2}(4\gamma^{(1)} + \gamma^{(2)})\rho_{0211} & -(2\gamma^{(1)} + \gamma^{(2)})\rho_{0220} & -(2\gamma^{(1)} + \gamma^{(2)})\rho_{0202} \end{pmatrix} \quad (30)$$

where  $\rho_{ijkl} = |\langle i|_1 \langle j|_2 \rho |k\rangle_1 |l\rangle_2\rangle$ . So as to obtain the time-dependent density matrix of the system, we numerically solve the system of ordinary differential equations in *Wolfram Mathematica*. We employ the variable stepsize implicit Backward Differentiation Formulas (BDF) or order 5. The *WorkingPrecision* used in this algorithm was set to the *MachinePrecision*, which, in our case, corresponds to 16 digits. In addition, the *AccuracyGoal* and *PrecisionGoal* options are set to 10. The diagonal elements of this density matrix exactly correspond to the probability of the plasmons being in different modes. For example,  $\rho_{1111}(t)$  is the probability that one plasmon is found in each nanoribbon at a given time,  $\rho_{2020}(t) + \rho_{0202}(t)$  is the probability that two plasmons are found in a single nanoribbon at a given time, and  $\rho_{0000}(t)$  is the probability of not having any plasmon in the system at a given time.

Once the density matrix of our system is found, we proceed to find the required interaction time between the nanoribbons to implement a  $\text{SWAP}^{1/2}$ . To do so, we set our initial state to be  $\rho(t=0) = |\psi\rangle\langle\psi|$ , where  $|\psi\rangle = |1\rangle_1|0\rangle_2$ , let it evolve in time and find  $t_{\text{SWAP}^{1/2}}$  by looking for the time at which the probability of the plasmon being in either of the modes is equal; i.e.,  $P_{110}(t_{\text{SWAP}^{1/2}}) = P_{011}(t_{\text{SWAP}^{1/2}})$ . The solution to this condition was found numerically using *Wolfram Mathematica* with a minimum accuracy and precision of 10 digits. Once  $t_{\text{SWAP}^{1/2}}$  is determined, we define our initial state to be  $\rho(t=0) = |\psi\rangle\langle\psi|$ , where  $|\psi\rangle = |1\rangle_1|1\rangle_2$ , and find the success probability of the gate  $P_{11}$  at time  $t_{\text{SWAP}^{1/2}}$ . Representative time-dependent density-matrix elements are plotted in Fig. S6 in the Supplementary Information.

#### DATA AVAILABILITY

The datasets generated and analysed during the current study are available from the corresponding author if you ask nicely.

#### ACKNOWLEDGEMENTS

I.A.C. acknowledges support from the University of Vienna via the Vienna Doctoral School. L.A.R. acknowledges support from the Templeton World Charity Foundation (fellowship no. TWCF0194). M.R. acknowledges support from the European Commission through the project QUCHIP (grant no. 641039). P.W. acknowledges support from the European Commission through ERBeSta (No. 800942), the Austrian

Research Promotion Agency (FFG) through the QuantERA ERA-NET Cofund project HiPhoP (no. 731473), from the Austrian Science Fund (FWF) through CoQuS (W 1210-N25), NaMuG (P 30067-N36) and BeyondC (F 7113-N38), the U.S. Air Force Office of Scientific Research (FA2386-233 17-1-4011), and Red Bull GmbH. J.D.C., J.R.M.S., and F. J.G.A., acknowledge support from the European Research Council (Advanced Grant No. 789104-eNANO), the Spanish MINECO (MAT2017-88492-R and SEV2015-0522), the European Commission (Graphene Flagship 696656), the Catalan CERCA, and Fundació Privada Cellex. We thank T. Rögelsperger for his artistic input.

#### AUTHOR CONTRIBUTIONS

I.A.C., L.A.R., and P.W. proposed the design of the coupled nanoribbons and performed the numerical calculations. I.A.C., and M.R. derived the master equation for our system. J.D.C., J.R.M.S., and F.J.G.A. derived analytical expressions for the graphene parameters. I.A.C., J.D.C., M.R., and J.R.M.S. wrote the simulation code. I.A.C., J.D.C., and L.A.R. wrote the manuscript. All authors read and commented on the manuscript.

#### ADDITIONAL INFORMATION

**Supplementary Information** accompanies the paper on the *npj Quantum Information* website (<https://doi.org/10.1038/s41534-019-0150-2>).

**Competing interests:** The authors declare no competing interests.

**Publisher's note:** Springer Nature remains neutral with regard to jurisdictional claims in published maps and institutional affiliations.

#### REFERENCES

- Knill, E., Laflamme, R. & Milburn, G. J. A scheme for efficient quantum computation with linear optics. *Nature* **409**, 46–52 (2001).
- Neville, A. et al. Classical boson sampling algorithms with superior performance to near-term experiments. *Nat. Phys.* **13**, 1153–1157 (2017).
- O'Shea, D., Junge, C., Volz, J. & Rauschenbeutel, A. Fiber-optical switch controlled by a single atom. *Phys. Rev. Lett.* **110**, 193601 (2013).
- Franson, J. D., Jacobs, B. C. & Pittman, T. B. Quantum computing using single photons and the Zeno effect. *Phys. Rev. A* **70**, 062302 (2004).
- Nielsen, M. A. & Chuang, I. L. *Quantum Computation and Quantum Information* (Cambridge University Press, United Kingdom, 2013).
- Misra, B. & Sudarshan, E. C. G. The Zeno's paradox in quantum theory. *J. Math. Phys.* **18**, 756 (1977).
- Haroche, S. Nobel lecture: Controlling photons in a box and exploring the quantum to classical boundary. *Rev. Mod. Phys.* **85**, 1083–1102 (2013).
- Fang, Y. & Sun, M. Nanoplasmonic waveguides: towards applications in integrated nanophotonic circuits. *Light Sci. Appl.* **4**, e294 (2015).
- Fakonas, J. S., Lee, H., Kelaita, Y. A. & Atwater, H. A. Two-plasmon quantum interference. *Nat. Photonics* **8**, 317–320 (2014).
- Heeres, R. W., Kouwenhoven, L. P. & Zwiller, V. Quantum interference in plasmonic circuits. *Nat. Nanotechnol.* **8**, 719–722 (2013).
- Woessner, A. et al. Highly confined low-loss plasmons in graphene-boron nitride heterostructures. *Nat. Mater.* **14**, 421–425 (2015).
- Ni, G. X. et al. Fundamental limits to graphene plasmonics. *Nature* **557**, 530–533 (2018).
- García de Abajo, F. J. Graphene plasmonics: Challenges and opportunities. *ACS Photonics* **1**, 135–152 (2014).
- Rivera, N., Kaminer, I., Zhen, B., Joannopoulos, J. D. & Soljačić, M. Shrinking light to allow forbidden transitions on the atomic scale. *Science* **353**, 263–269 (2016).
- Hendry, E., Hale, P. J., Moger, J., Savchenko, A. K. & Mikhailov, S. A. Coherent nonlinear optical response of graphene. *Phys. Rev. Lett.* **105**, 097401 (2010).
- Constant, T. J., Hornett, S. M., Chang, D. E. & Hendry, E. All-optical generation of surface plasmons in graphene. *Nat. Phys.* **12**, 124–127 (2016).
- Cox, J. D. & García de Abajo, F. J. Electrically tunable nonlinear plasmonics in graphene nanoislands. *Nat. Comm.* **6**, 725, 5725 (2014).
- Koppens, F. H., Chang, D. E. & García de Abajo, F. J. Graphene plasmonics: A platform for strong light-matter interactions. *Nano Lett.* **11**, 3370–3377 (2011).

- Gullans, M., Chang, D. E., Koppens, F. H. L., García de Abajo, F. J. & Lukin, M. D. Single-photon nonlinear optics with graphene plasmons. *Phys. Rev. Lett.* **111**, 247401 (2013).
- Jablan, M. & Chang, D. E. Multiplasmon absorption in graphene. *Phys. Rev. Lett.* **114**, 236801 (2015).
- Wu, L.-A., Walther, P. & Lidar, D. A. No-go theorem for passive single-rail linear optical quantum computing. *Sci. Rep.* **3**, 1394 (2013).
- Leung, P. M. & Ralph, T. C. Optical Zeno gate: bounds for fault tolerant operation. *New J. Phys.* **9**, 224 (2007).
- Martino, G. D. et al. Observation of quantum interference in the plasmonic Hongou-mandel effect. *Phys. Rev. Appl.* **1**, 034004 (2014).
- Akimov, A. V. et al. Generation of single optical plasmons in metallic nanowires coupled to quantum dots. *Nature* **450**, 402–406 (2007).
- Tame, M. S. et al. Quantum plasmonics. *Nat. Phys.* **9**, 329–340 (2013).
- Zhang, Y.-X., Zhang, Y. & Molmer, K. Directional launching of surface plasmons by polariton superradiance. *ArXiv* 1807.03682 (2018).
- Hanson, G. W., Gangaraj, S. A. H., Lee, C., Angelakis, D. G. & Tame, M. Quantum plasmonic excitation in graphene and loss-insensitive propagation. *Phys. Rev. A* **92**, 013828 (2015).
- Yu, R., Cox, J. D., Saavedra, J. R. M. & Garca de Abajo, F. J. Analytical modeling of graphene plasmons. *ACS Photon.* **4**, 3106–3114 (2017).
- Mikhailov, S. A. Quantum theory of the third-order nonlinear electrodynamic effects of graphene. *Phys. Rev. B* **93**, 085403 (2016).
- Breuer, H.-P. & Petruccione, F. *The theory of open quantum systems.* (Oxford University Press, United Kingdom, 2007).
- Iranzo, D. A. et al. Probing the ultimate plasmon confinement limits with a van der Waals heterostructure. *Science* **360**, 291–295 (2018).
- Zaidi, H. A., Dawson, C., van Loock, P. & Rudolph, T. Near-deterministic creation of universal cluster states with probabilistic Bell measurements and three-qubit resource states. *Phys. Rev. A* **91**, 042301 (2015).
- Wang, D. S., Fowler, A. G. & Hollenberg, L. C. L. Surface code quantum computing with error rates over 1%. *Phys. Rev. A* **83**, 020302 (2011).
- O'Brien, J. L. et al. Quantum process tomography of a controlled-not gate. *Phys. Rev. Lett.* **93**, 080502 (2004).
- Gilchrist, A., Langford, N. K. & Nielsen, M. A. Distance measures to compare real and ideal quantum processes. *Phys. Rev. A* **71**, 062310 (2005).
- Chen, C.-F. et al. Controlling inelastic light scattering quantum pathways in graphene. *Nature* **471**, 617–620 (2011).
- Efetov, D. K. & Kim, P. Controlling electron-phonon interactions in graphene at ultrahigh carrier densities. *Phys. Rev. Lett.* **105**, 256805 (2010).
- Kimouche, A. et al. Ultra-narrow metallic armchair graphene nanoribbons. *Nat. Comm.* **6**, 10177 (2015).
- Brar, V. W., Jang, M. S., Sherrott, M., Lopez, J. J. & Atwater, H. A. Highly confined tunable mid-infrared plasmonics in graphene nanoresonators. *Nano Lett.* **13**, 2541–2547 (2013).
- Brar, V. W. et al. Hybrid surface-phonon-plasmon polariton modes in graphene/monolayer h-bn heterostructures. *Nano Lett.* **14**, 3876–3880 (2014).
- Bouwmeester, D. et al. Experimental quantum teleportation. *Nature* **390**, 575–579 (1997).
- Walther, P. et al. Experimental one-way quantum computing. *Nature* **434**, 169–176 (2005).

 **Open Access** This article is licensed under a Creative Commons Attribution 4.0 International License, which permits use, sharing, adaptation, distribution and reproduction in any medium or format, as long as you give appropriate credit to the original author(s) and the source, provide a link to the Creative Commons license, and indicate if changes were made. The images or other third party material in this article are included in the article's Creative Commons license, unless indicated otherwise in a credit line to the material. If material is not included in the article's Creative Commons license and your intended use is not permitted by statutory regulation or exceeds the permitted use, you will need to obtain permission directly from the copyright holder. To view a copy of this license, visit <http://creativecommons.org/licenses/by/4.0/>.

© The Author(s) 2019

**Quantum Computing with Graphene Plasmons**  
- Supplementary Figures -

I. Alonso Calafell,<sup>1</sup> J. D. Cox,<sup>2</sup> M. Radonjić,<sup>1</sup> J. R. M. Saavedra,<sup>2</sup>  
F. J. García de Abajo,<sup>2,3</sup> L. A. Rozema,<sup>1</sup> and P. Walther<sup>1</sup>

<sup>1</sup>Vienna Center for Quantum Science and Technology (VCQ), Faculty of Physics,  
University of Vienna, Boltzmannngasse 5, Vienna A-1090, Austria

<sup>2</sup>ICFO-Institut de Ciències Fotoniques, The Barcelona Institute of  
Science and Technology, 08860 Castelldefels (Barcelona), Spain

<sup>3</sup>ICREA-Institució Catalana de Recerca i Estudis Avançats,  
Passeig Lluís Companys, 23, 08010 Barcelona, Spain

(Dated: April 5, 2019)

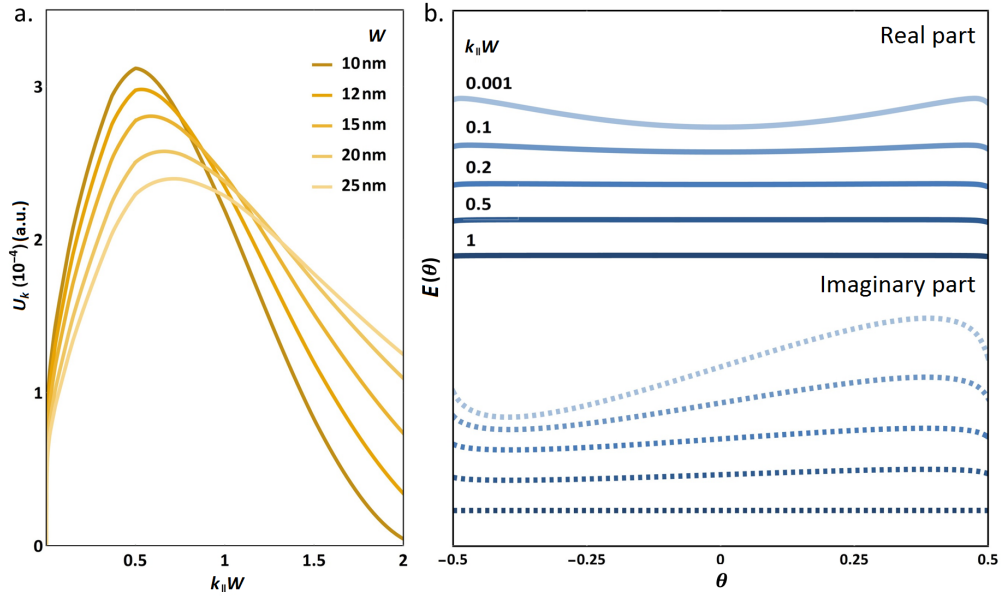


FIG. S1: **Study of the coupling between graphene nanoribbons.** **a.** Coupling energy between adjacent nanoribbons ( $d_z = 1 \text{ nm}$ ) given by the Coulomb interaction as a function of wave vector parallel to ribbons,  $k_{\parallel} W$ . **b.** Plasmon field distribution across the graphene nanoribbon for different parallel wave vectors  $k_{\parallel} W$ , plotted as a function of normalized transverse coordinate  $\theta = x/W$ .

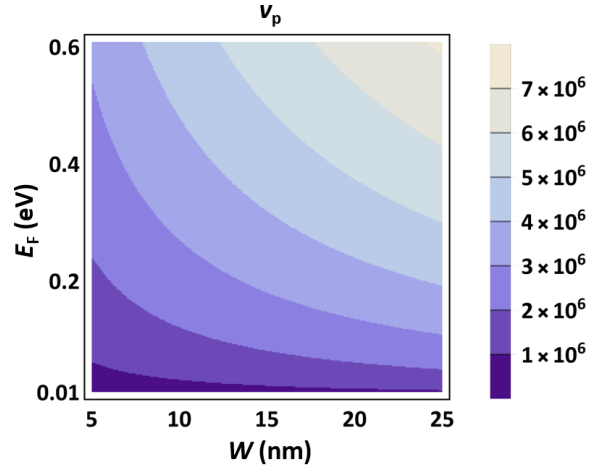


FIG. S2: Group velocity of graphene plasmon-polaritons for different nanoribbon widths  $W$  and Fermi energies  $E_F$ . This velocity is calculated from the dispersion relation as  $v_p = \frac{d\omega}{dk_{\parallel}}$ , where  $\omega$  is the plasmon frequency plotted in Fig. S3 and  $k_{\parallel}$  is the plasmon wave vector [1].

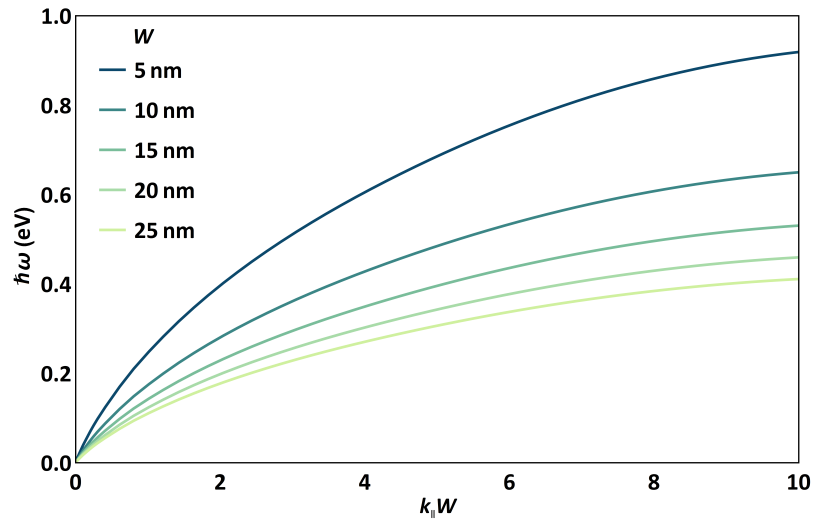


FIG. S3: Plasmon dispersion relation. We show the dispersion relation of graphene plasmons for different nanoribbon widths  $W$  [1].

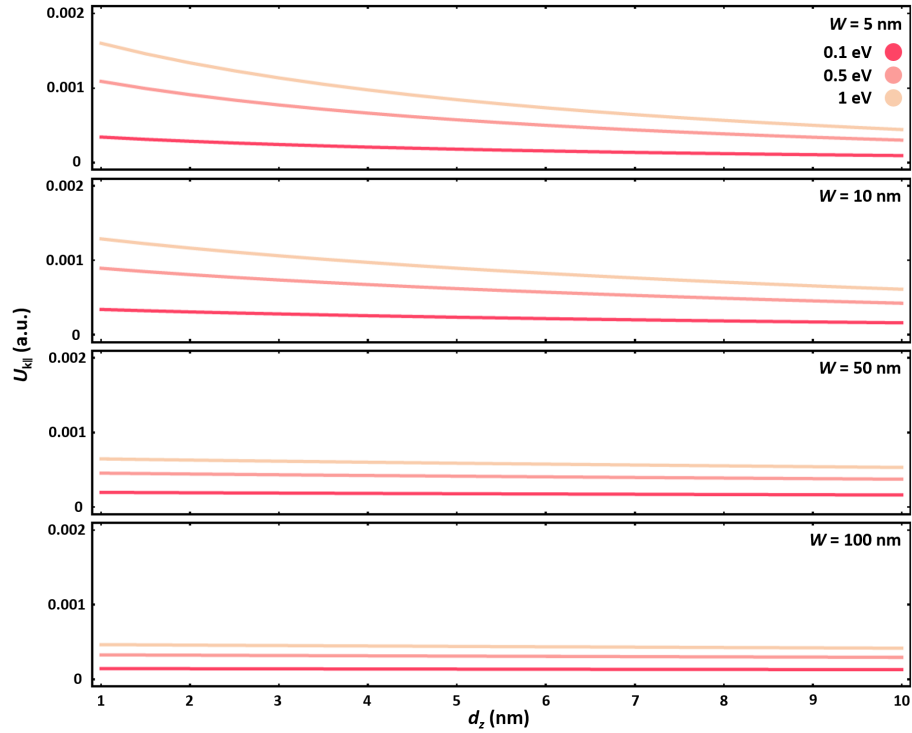


FIG. S4: Coulomb interaction as a function of spacing between nanoribbons  $d_z$  for different nanoribbon widths  $W$  and Fermi energies  $E_F$ . For the results presented in the main text we set  $d_z = 1$  nm. For smaller  $d_z$  the interaction strength increases, which results in shorter interaction lengths  $L_{\text{SWAP}}^{1/2}$ . This could thus improve the success probability of the gate in the presence of shorter plasmon lifetimes. In contrast, if  $d_z$  is too large, depending on the plasmon lifetime, the plasmons could decay before the root-SWAP condition is achieved.

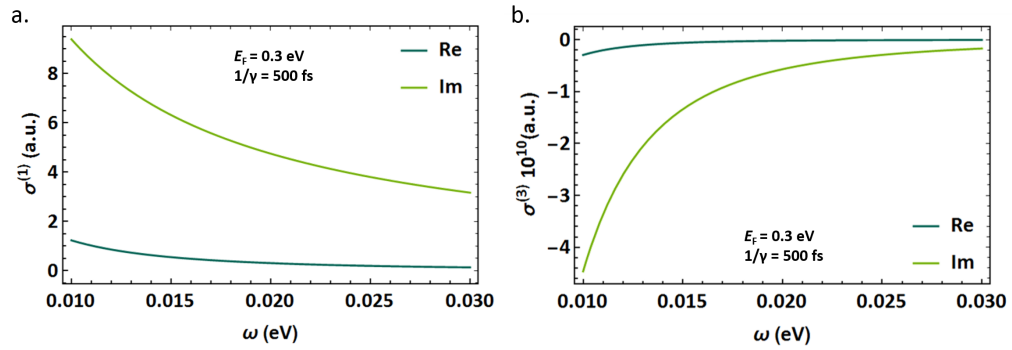


FIG. S5: **Linear and nonlinear conductivities.** We plot the real and imaginary parts of **a.** the linear conductivity  $\sigma^{(1)}$  and **b.** the third-order conductivity  $\sigma^{(3)}$  as a function of the plasmon frequency, at  $E_F = 0.3$  eV and plasmon lifetime  $1/\gamma = 500$  fs.

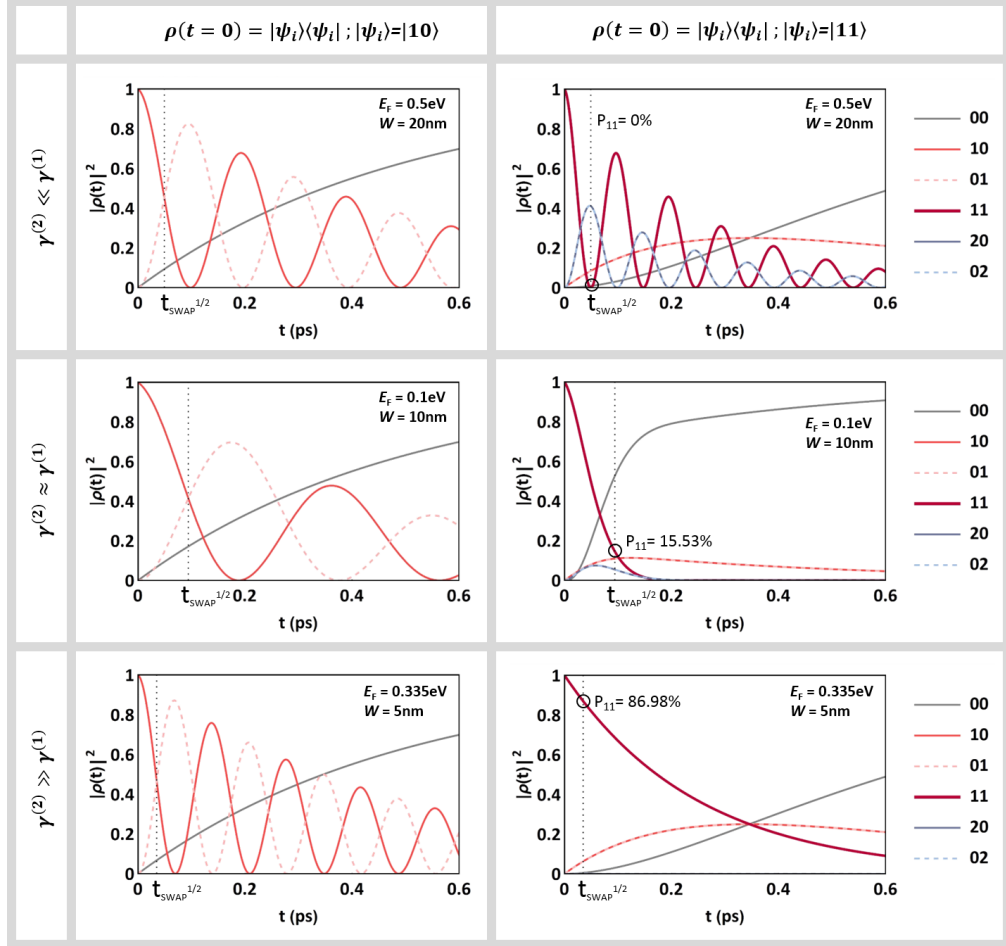


FIG. S6: **Time evolution of the density matrix elements.** We study the time evolution of the elements of the calculated density matrix for three different cases:  $\gamma^{(2)} \ll \gamma^{(1)}$ ,  $\gamma^{(2)} \approx \gamma^{(1)}$  and  $\gamma^{(2)} \gg \gamma^{(1)}$ , corresponding to the 1st, 2nd and 3rd row of the table, respectively. In the first column, we set our initial state to be  $\rho(t=0) = |\psi_i\rangle\langle\psi_i|$ , where  $|\psi_i\rangle = |1\rangle_1 |0\rangle_2$ , let it evolve in time and find  $t_{\text{SWAP}}^{1/2}$  by looking for the time at which the probability of the plasmon being in either of the modes is equal; *i.e.*  $P_{10}(t_{\text{SWAP}}^{1/2}) = P_{01}(t_{\text{SWAP}}^{1/2})$ . Once  $t_{\text{SWAP}}^{1/2}$  is determined, in the second column, we define our initial state to be  $\rho(t=0) = |\psi_i\rangle\langle\psi_i|$ , where  $|\psi_i\rangle = |1\rangle_1 |1\rangle_2$ , and find the success probability of the gate  $P_{11}$  at time  $t_{\text{SWAP}}^{1/2}$ . As expected, when  $\gamma^{(2)} \ll \gamma^{(1)}$ , the absence of two-plasmon absorption leads to a strong Hong-Ou-Mandel effect. As the strength of the two-plasmon absorption increases,  $\gamma^{(2)} \approx \gamma^{(1)}$ , the losses start increasing as the Zeno effect is not yet significant and this leads to a high population of the vacuum state. Finally, when two-plasmon absorption prevails,  $\gamma^{(2)} \gg \gamma^{(1)}$ , the strong Zeno effect prevents the system from evolving into those undesired states in which the plasmons are found in the same mode and the success probability of the gate increases largely, reaching up to 87% for  $E_F = 0.335$  eV and  $W = 5$  nm.

- 
- [1] García de Abajo, F. J. Graphene plasmonics: Challenges and opportunities. *ACS Photonics* **1**, 135–152 (2014).

## 7.2 Trace-free counterfactual communication with a nanophotonic processor

In standard communication, the transmission of a message is always associated with a particle or entity travelling in the same direction. In this paper we present an experiment performed in a silicon-on-insulator nanophotonic processor, where we demonstrate the transmission of a message from Bob to Alice, while single-photons travel in the opposite direction, from Alice to Bob. We do this without any weak trace of the photon travelling in the same direction as the message, while simultaneously achieving a bit error rate below 1%.

For further understanding this topic, I recommend reading Sections 2-Fundamentals of Photonics and 5.4.1-The Elitzur-Vaidman Bomb experiment.

ARTICLE OPEN

## Trace-free counterfactual communication with a nanophotonic processor

I. Alonso Calafell<sup>1</sup>, T. Strömberg<sup>1</sup>, D. R. M. Arvidsson-Shukur<sup>2,3</sup>, L. A. Rozema<sup>1</sup>, V. Saggio<sup>1</sup>, C. Greganti<sup>1</sup>, N. C. Harris<sup>4</sup>, M. Prabhu<sup>4</sup>, J. Carolan<sup>4</sup>, M. Hochberg<sup>5</sup>, T. Baehr-Jones<sup>5</sup>, D. Englund<sup>6</sup>, C. H. W. Barnes<sup>2</sup> and P. Walther<sup>6</sup>

In standard communication information is carried by particles or waves. Counterintuitively, in counterfactual communication particles and information can travel in opposite directions. The quantum Zeno effect allows Bob to transmit a message to Alice by encoding information in particles he never interacts with. A first remarkable protocol for counterfactual communication relied on thousands of ideal optical operations for high success rate performance. Experimental realizations of that protocol have thus employed post-selection to demonstrate counterfactuality. This post-selection, together with arguments concerning a so-called “weak trace” of the particles traveling from Bob to Alice, have led to a discussion regarding the counterfactual nature of the protocol. Here we circumvent these controversies, implementing a new, and fundamentally different, protocol in a programmable nanophotonic processor, based on reconfigurable silicon-on-insulator waveguides that operate at telecom wavelengths. This, together with our telecom single-photon source and highly efficient superconducting nanowire single-photon detectors, provides a versatile and stable platform for a high-fidelity implementation of counterfactual communication with single photons, allowing us to actively tune the number of steps in the Zeno measurement, and achieve a bit error probability below 1%, without post-selection and with a vanishing weak trace. Our demonstration shows how our programmable nanophotonic processor could be applied to more complex counterfactual tasks and quantum information protocols.

npj Quantum Information (2019)5:61; <https://doi.org/10.1038/s41534-019-0179-2>

## INTRODUCTION

Interaction-free measurements allow one to measure whether or not an object is present without ever interacting with it.<sup>1</sup> This is made clear in Elitzur and Vaidman’s well-known bomb-testing gedanken experiment.<sup>2</sup> In this experiment, a single photon used in a Mach-Zehnder interferometer (MZI) sometimes reveals whether or not an absorbing object (e.g., a bomb) had been placed in one of the interferometer arms, without any interaction between the photon and the bomb. It was later shown that the quantum Zeno effect, wherein repeated observations prevent the system from evolving,<sup>3,4</sup> can be used to bring the success probability of this protocol arbitrarily close to unity.<sup>3–6</sup> Such protocols are often referred to as “counterfactual”, and have now been applied to quantum computing,<sup>7</sup> quantum key distribution<sup>8–10</sup> and communication.<sup>11,12</sup> Here, we experimentally implement a counterfactual communication (CFC) protocol where information can propagate without being carried by physical particles.

The first suggested protocol for CFC was developed by Salih et al., and it is based on a chain of nested MZIs.<sup>11,13</sup> Following its publication, this fascinating protocol has been subject to both intense criticism and vigorous defense. There are four main points of discussion: (1) Achieving a high success probability (say > 95%) requires thousands of optical elements.<sup>11,12,14</sup> (2) An analysis of the Fisher information flow indicates that to retain

counterfactuality in Salih’s protocol, perfect quantum channels are needed.<sup>15</sup> (3) If one performs a weak measurement in Bob’s lab, one can detect the presence of photons that are later found in Alice’s laboratory. Some authors have argued that the presence of the “weak trace” renders the counterfactuality of the protocol invalid,<sup>16–19</sup> but others have dismissed the weak trace as a consequence of the unwanted weak measurement’s disturbance.<sup>20–22</sup> (4) Unless operated in the theoretical limit of infinite optical operations, this scheme requires post-selection to remove the CFC violations.<sup>13,21,23</sup> It has recently been shown that also a classical communication protocol can be counterfactual if post-selection is allowed.<sup>14</sup>

To circumvent these issues, we implement a novel CFC protocol<sup>12</sup> that does not need post-selection and requires orders of magnitude fewer optical elements than nested MZI protocols. In our scheme single photons travel from Alice to Bob but information from Bob to Alice; this has been dubbed type-II CFC, in contrast to type-I schemes, where the photon should remain with Alice throughout the protocol.<sup>15</sup> In both types the particles and the information never co-propagate, thereby making the communication counterfactual. Note that the very recent proposals<sup>23,24</sup> discussing means of making the Salih scheme trace-free still require the post-selected removal of non-counterfactual events, as well as thousands of ideal optical operations.

<sup>1</sup>Faculty of Physics, Vienna Center for Quantum Science and Technology (VCQ), University of Vienna, Boltzmanngasse 5, A-1090 Vienna, Austria; <sup>2</sup>Department of Physics, Cavendish Laboratory, University of Cambridge, Cambridge CB3 0HE, UK; <sup>3</sup>Department of Mechanical Engineering, Massachusetts Institute of Technology, Cambridge, MA 02139, USA; <sup>4</sup>Quantum Photonics Group, RLE, Massachusetts Institute of Technology, Cambridge, MA 02139, USA and <sup>5</sup>Elenion Technologies, New York, NY 10016, USA  
Correspondence: I. Alonso Calafell ([irati.alonso.calafell@univie.ac.at](mailto:irati.alonso.calafell@univie.ac.at)) or T. Strömberg ([teodor.stroemberg@univie.ac.at](mailto:teodor.stroemberg@univie.ac.at))  
These authors contributed equally: I. Alonso Calafell, T. Strömberg

Received: 4 October 2018 Accepted: 27 June 2019  
Published online: 23 July 2019

Published in partnership with The University of New South Wales

## RESULTS

We perform our experiment using telecom single-photons in a state-of-the-art programmable nanophotonic processor (PNP),<sup>25</sup> which is orders of magnitude more precise and stable than previous bulk-optic approaches.<sup>5,6</sup> Our PNP also provides unprecedented tunability, which we use to investigate the scaling of the protocol by changing the number of chained interferometers. By combining the novel CFC protocol with our advanced photonic technology, we are able to implement counterfactual communication with a bit success probability above 99%, without post-selection. As in previous CFC protocols, the interferometer implementing the quantum Zeno effect is shared between Bob's laboratory and the fully passive transmission channel. In contrast to these protocols, ours protocol allows for Alice's laboratory to be situated outside the interferometer. As a result, even our proof-of-principle demonstration would allow for counterfactual communication over arbitrary distances, even if the region in which the non-local information transfer takes place is bounded by the size of the PNP.

Our protocol uses a series of  $N$  beamsplitters with reflectivity  $R = \cos^2(\pi/2N)$ , which, together with mirrors, form a circuit of  $N - 1$  chained MZIs. As shown in Fig. 1, the communication protocol begins with Alice injecting a single photon into her input port. If Bob wants to send a logic 0 he leaves his mirrors in place, causing the photon to self interfere such that it exits in  $D_B$  with unit probability (Fig. 1a). To send a logic 1 Bob *locally* modifies the circuit to have the upper paths open (Fig. 1b). In this case the photon will successfully reflect off of all the beamsplitters and exit in  $D_A$  with probability  $R^M$ . Removing the mirrors effectively collapses the wavefunction after every beamsplitter, suppressing interference and implementing the Zeno effect. The probability that the photon remains in the lower arm after  $N$  beamsplitters can be made arbitrarily high by increasing  $N$  (and changing the reflectivities accordingly).

Since any implementation is restricted to a finite number of beamsplitters, there will be a probability for a photon to exit the wrong port when Bob tries to send a logic 1. This error probability is a function that decreases with  $N$  as  $P_{1, \text{err}} = 1 - R(N)^M$ . In the non-ideal case, optical losses in the system will increase this probability further. The errors associated with Bob's attempt to transmit a logic 0 are of a different nature. In theory, he can always perfectly transmit a logic 0, independent of  $N$ ; that is,  $P_{0, \text{err}} = 0$ . In practice,

however, imperfections in the interferometers will lead to cases in which the photon re-enters Alice's laboratory and she incorrectly records a logic 1. This leads to a rare counterfactual violation, as the wavefunction "leaks" from Bob's to Alice's laboratory,<sup>15</sup> leaving a weak trace in Bob's lab, while the photon is detected in Alice's laboratory. The high-fidelity operations enabled by our PNP allows us to make the probability of such violations vanishingly small. Although they do not contribute to a counterfactual violation, dark counts in Alice's detector will also increase this error rate.

We can overcome the bit errors by encoding each logical bit into  $M$  single photons, at the cost of slightly increasing the CFC violation. If Alice sends  $M$  photons into the transmission channel without detecting any at  $D_A$ , she will record a logic 0. On the other hand, if she detects one or more photons in her laboratory, she will record a logic 1. Assuming messages with a balanced number of 0s and 1s, the average bit error probability is given by:

$$\bar{P}_{\text{err}}(M) = \frac{1}{2}[(P_{1, \text{err}})^M + MP_{0, \text{err}}] \quad (1)$$

where the second term is an approximation of  $1 - P_0^M$  valid for small values of  $MP_{0, \text{err}}$ . By increasing  $M$  we can thus decrease the contributions of  $P_{1, \text{err}}$  exponentially while only increasing those of  $P_{0, \text{err}}$  linearly. The counterfactual violation probability for a random bit is given by

$$\bar{P}_{\text{CFC}}(M) = \frac{1}{2\eta} MP_{0, \text{err}}, \quad (2)$$

where  $\eta$  is the detector efficiency. We can thus find an  $M$  that minimizes the average bit error, while also maintaining a low counterfactual violation probability. In our experiment this expression slightly overestimates the violation probability, as it includes the detector dark counts.

As illustrated in Fig. 2, we implement a series of chained MZIs using a PNP. At the intersections of each of the modes shown in the figure there are smaller MZIs that act as beamsplitters with tunable reflectivities and phases. Since each of the MZIs is completely tunable, we were able to implement our CFC protocol using two to six concatenated beamsplitters on the same photonic chip. Given the layout of our chip, six is the maximum number of beamsplitter that we can concatenate. In addition, the high interferometric visibility of the PNP, which we measure to be 99.94% on average, allows us to keep the rate of counterfactual violations low, without post-selection. The single photons are generated in a spontaneous parametric down conversion process and detected using superconducting nanowire single-photon detectors with detection efficiencies  $\eta \sim 90\%$  (see Methods).

## DISCUSSION

To study the performance of this CFC protocol we measure the average bit error, as a function of the number of photons in which the bit is encoded,  $M$ , for five different values of  $N$  number of BSs. For the logic 0, we configure the MZIs in Bob's laboratory as mirrors (see Fig. 2), while for the logic 1 we let the MZIs in Bob's laboratory act as SWAP gates, routing the light out of the interferometer chain. Since Alice cannot access detector  $D_B$ , she assumes that a photon is injected in the transmission channel every time she detects a heralding photon in  $D_H$ . We thus run the measurement until we have  $M$  recorded single-photon events in  $D_H$  (typical rates were 1.1 MHz) and look for the coincidences that these events have with  $D_A$  within a set coincidence window  $\Delta\tau = 2.5$  ns that is shorter than the pulse separation. Our heralding efficiency was  $\sim 3\%$  through the PNP.

Figure 3a shows the experimental average error probability of our CFC protocol as a function of  $M$  for different  $N$ . We also include a theoretical calculation of the expected error probabilities, which considers the heralding efficiency of the single photons and the success probability of the interferometer that is in good

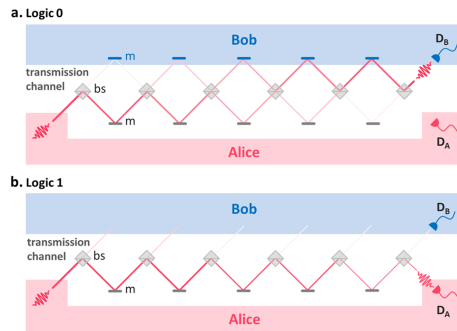


**Fig. 1** Architecture of the chained MZI protocol. Alice inputs a photon into the transmission channel, consisting of a row of beamsplitters (BSs) and the lower row of mirrors (marked with an 'm'). **a** If Bob intends to send a logic 0, he places mirrors in his laboratory to form MZIs that span his lab and the transmission channel, creating constructive interference in Bob's port ( $D_B$ ). **b** If he intends to send a logic 1, he removes the mirrors, causing the photons to arrive back in Alice's laboratory ( $D_A$ ) with high probability

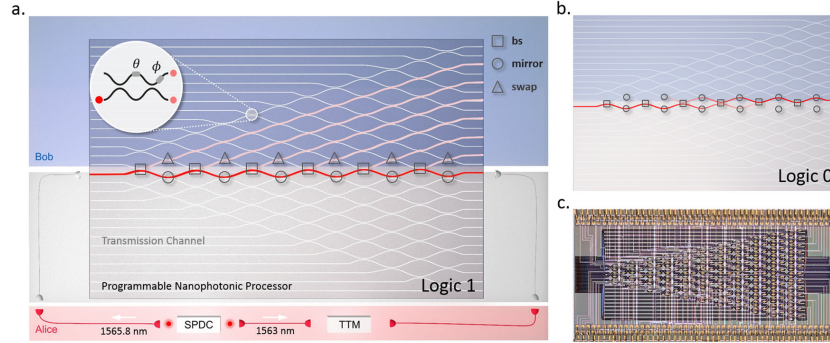


**Fig. 2** Experimental setup. **a** Our experiment is implemented in a programmable nanophotonic processor (PNP), which is composed of 26 interconnected waveguides. The waveguides are coupled by 88 Mach-Zehnder interferometers (MZIs), as indicated by the top-left inset. Each MZI is equipped with a pair of thermo-optic phase shifters, which allows us to treat them as beamsplitters with fully tunable reflectivities (set via  $\theta \in [0, 2\pi]$ ) and phases ( $\phi \in [0, 2\pi]$ ). In our work, we set  $\theta$  to  $\pi$ , 0 or  $\pi/2N$ , to implement mirrors (circles), SWAPs (triangles) or beamsplitters (squares), respectively. In Alice's laboratory (the pink shaded region) a spontaneous parametric down-conversion source creates a frequency non-degenerate photon pair at  $\lambda_H = 1563$  nm and  $\lambda_T = 1565.8$  nm. Detection of the  $\lambda_H$  photon in detector H heralds the  $\lambda_T$  photon that is injected into the transmission channel. This channel is comprised of the lower half of the PNP, in which MZIs are set to act as mirrors, as well as the MZIs that couple the upper and lower half of the waveguide. The latter of these MZIs are configured to act as beamsplitters, whose reflectivity varies with  $N$  (the number of beamsplitters used in the protocol) as  $R(N) = \cos^2(\pi/2N)$ . Bob's laboratory consists of the upper set of MZIs (blue shaded area), which he can set as mode swaps to send a logic 1 or **b** as mirrors to send a logic 0. Thus in total we used 48 MZIs: 6 to implement the tunable beamsplitters, 30 to implement the loss channels, 6 for the mirrors in the transmission channel, and 6 for the mode swaps/mirrors in Bob's laboratory. The photons are detected in Alice's laboratory by superconducting nanowire single-photon detectors with detection efficiencies of approximately 90%. Coincident detection events are recorded with a custom-made Time Tagging Module (TTM). **c** Micrograph of the PNP with dimensions  $4.9 \times 2.4$  mm

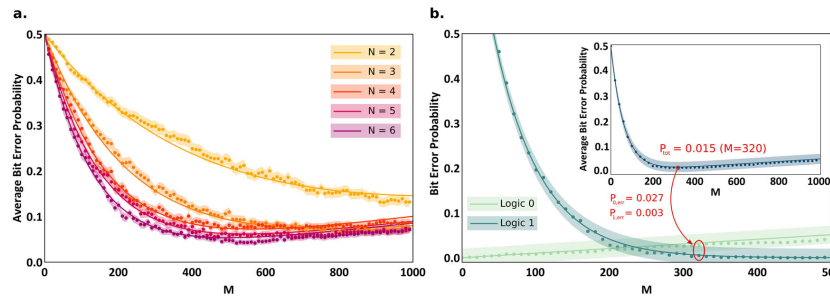


**Fig. 3** Success probabilities of the CFC communication. The curves are theoretical models of our experiment with no free parameters, and the points are experimental data. **a** Measured average bit error (as defined in the main text) of the protocol for different number of beamsplitters ( $N$ ) as a function of the number of photons ( $M$ ) used to encode each bit. For small  $M$  the  $\cos^{2N}(\pi/2N)$  dependence of the logic 1 error dominates the average error, making the latter decrease with  $M$  as expected. As  $M$  is increased more, the linearly growing error in the logic 0, caused by imperfect destructive interference in Alice's port ( $D_A$ ), starts to dominate. **b** In the  $N = 6$  case, the optimization of the interferometer fidelity and heralding efficiency leads to an average bit error rate of 1.5% for  $M = 320$ , where the average CFC violation probability is 2.4%

agreement with the experimental data. Note that these are not fits to the data, but rather models with no free parameters. As theoretically predicted, the error rate of the logic 1 decreases exponentially with increasing  $M$  and the error rate of the logic 0 increases linearly with  $M$ . We observe that higher  $N$  requires smaller  $M$ , and also results in lower bit error probabilities.

The success probability of this CFC scheme is highly sensitive to the fidelity of the interferometers and the overall heralding efficiency, which depends on the single-photon source and the coupling efficiency throughout the system. Hence, we optimized the setup for the  $N = 6$  case. Figure 3b shows the corresponding

error probability of the logic 1 and the logic 0. The inset in Fig. 3b shows the average error probability, where we find a minimum of 1.5% for  $M = 320$ , while the average counterfactual violation is kept at 2.4%. Owing to backscattering in Bob's laboratory (i.e., imperfect SWAP operations) small "amounts" of wavefunction amplitude leak back into the transmission line in the 1 bit process. Although these do not all lead to detection events in Alice's laboratory, the sum of their squares provides an upper bound on the probability of a counterfactual violation. We estimate that the probability for a photon to reflect off of a SWAP operation is at most 1%. Hence, in our experiment (Fig. 4) with  $M = 320$  and  $N =$

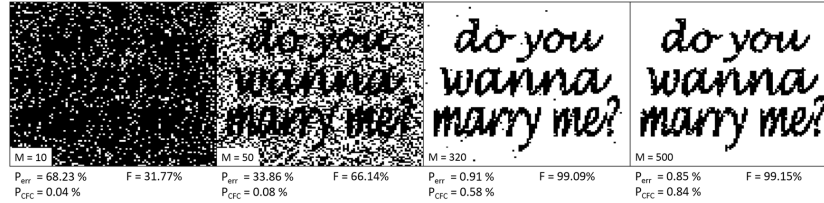


**Fig. 4** Image sent from Bob to Alice. The bits are encoded in different numbers of single photons  $M = \{10, 50, 320, 500\}$ . The white and black pixels are defined to correspond to logic 1 and logic 0, respectively. The success probability increases with increasing  $M$ , reaching 99% for  $M = 320$ . The CFC violation probability ( $P_{CFC}$ ) also increases with increasing  $M$ , but it remains as low as 0.6% for  $M = 320$ . Note that this CFC violation comes only from the logic 0 errors, which we can directly measure; the total CFC violation would include a small portion of successful logic 1 events, as discussed in the main text. Increasing  $M$  beyond 320 increases the success probability at the expense of increasing the CFC violation. As it can be observed, these probabilities are directly related to the transmission fidelity ( $F$ ) of the white pixels, which increases with  $M$ , and the transmission fidelity of the black pixels, which decreases with  $M$

6, the weak trace is vanishingly small and the contribution from the logic 1 to a CFC violation is less than 1.1%. Note that this violation probability decreases with  $N$ , even if the errors remain the same.

To demonstrate the performance of the communication protocol we proceed to analyze the quality of a message in the form of a black and white image, sent from Bob to Alice, for  $N = 6$  and  $M = \{10, 50, 320, 500\}$ . We arbitrarily define the white and black pixels of the image as logic 1 and logic 0, respectively.

Figure 4 shows the message transmitted from Bob to Alice for different numbers of encoding photons. We define the image fidelity as

$$F = \sum_{i=1}^T \frac{1 + (-1)^{A_i+B_i}}{2T} \quad (3)$$

where  $B_i$  is the bit that Bob intended to send,  $A_i$  is the bit that Alice recorded, and  $T$  is the total number of bits in the image. In this case we define the CFC violation probability as the number of incorrectly transmitted logic 0s (black pixels) over  $T$ . The encoding using  $M = 10$  is clearly not enough to overcome the losses of the system, with a very low image fidelity of 31.77%. As we increase  $M$ , the success probability and legibility of the message increases (the individual fidelities are listed below each panel). The image fidelity reaches 99.09% at  $M = 320$ , at which point the CFC violation probability from 0 bit errors remains as low as 0.6%. For  $M = 500$  the image fidelity does not noticeably change; however, the CFC violation increases slightly. If the CFC violation of the 1 bit (caused by on-chip beamsplitter imperfections) is accounted for, the CFC violation at  $M = 320$  increases to 2.3%. Note that these values are lower than the value in Fig. 3b due to the unbalanced distribution of black and white pixels in the image.

Our high-fidelity implementation of a counterfactual communication protocol without post-selection was enabled by a programmable nano-photon processor. The high (99.94%) average visibility of the individual integrated interferometers allowed bit error probabilities as low as 1.5%, while, at the same time, keeping the probability for the transmission of a single bit to result in a counterfactual violation below 2.4%. By combining our state-of-the-art photonic technology with a novel theoretical proposal we contradicted a crucial premise of communication theory:<sup>26</sup> that a message is carried by physical particles or waves. In fact, our work shows that “interaction-free non-locality”, first described by Elitzur and Vaidman,<sup>2</sup> can be utilized to send information that is not necessarily bound to the trajectory of a wavefunction or to a physical particle. In addition to enabling further high-fidelity demonstrations of counterfactual protocols, our work highlights the important role that technological advancements can play in experimental investigations of fundamentals of quantum mechanics and information theory. We thus

anticipate nanophotonic processors, such as ours, to be central to future photonic quantum information experiments all the way from the foundational level to commercialized products.

## METHODS

### Telecom photon source

We use a pulsed Ti:Sapphire laser with a repetition rate of 76 MHz, an average power of 0.2 W, a central wavelength of 782.2 nm, and a pulse duration of 2.1 ps. The repetition rate is doubled via a passive temporal multiplexing stage.<sup>27,28</sup> This beam pumps a periodically poled KTP crystal phase matched for collinear type-II spontaneous parametric down conversion, generating frequency non-degenerate photon pairs at  $\lambda_H = 1563$  nm,  $\lambda_V = 1565.8$  nm. Registering the shorter wavelength photon at the detector  $D_H$  heralds the presence of the longer wavelength one, which is sent to the waveguide.

### Programmable nanophotonic processor

Our chained Mach-Zehnder interferometers (MZIs) are implemented in a silicon-on-insulator (SOI) programmable waveguide, developed by the Quantum Photonics Laboratory at the Massachusetts Institute of Technology.<sup>29</sup> The device consists of 88 MZIs, each accompanied by a pair of thermo-optic phase shifters that facilitate full control over the internal and external phases of the MZIs. The phase shifters are controlled by a 240-channel, 16-bit precision voltage supply, allowing for a phase precision higher than 250  $\mu$ rad. The switching frequency of these phase shifters is 130 kHz. The coupling of the single photons in/out of the chip is performed using two  $\text{Si}_3\text{N}_4$ - $\text{SiO}_2$  waveguides manufactured by Lionix International, that adiabatically taper the  $10 \times 10$   $\mu$ m mode from the single mode fiber down to  $2 \times 2$   $\mu$ m, matching the mode field diameter of the programmable waveguide at the input facet. The total insertion loss per facet was measured as low as 3 dB.

### Superconducting nanowire single-photon detectors

The photons are detected using superconducting nanowire single-photon detectors.<sup>29,30</sup> These detectors are produced by photonSpot and are optimized to reach detection efficiencies  $\sim 90\%$  at telecom wavelengths.

## DATA AVAILABILITY

The datasets generated and analyzed during the current study are available from the corresponding author if you ask nicely.

## ACKNOWLEDGEMENTS

I.A.C. and T.S. acknowledge support from the University of Vienna via the Vienna Doctoral School. L.A.R. acknowledges support from the Templeton World Charity Foundation (fellowship no. TWCFO194). P.W. acknowledges support from the European Commission through ErBeSta (No. 800942), the Austrian Research Promotion Agency (FFG) through the QuantERA ERA-NET Cofund project HiPhoP, from the Austrian Science Fund (FWF) through CoQuS (W1210-N25), BeyondC (F7113-N38) and NaMuG (P30067-N36), the U.S. Air Force Office of Scientific Research

(FA2386-233 17-1-4011), and Red Bull GmbH. D.R.M.A.S. acknowledges support from the EPSRC, Hitachi Cambridge, Lars Hierta's Memorial Foundation and the Sweden-America Foundation. N.H. was supported in part by the Air Force Research Laboratory RITA program (FA8750-14-2-0120); Research program FA9550-16-1-0391, supervised by Gernot Pomrenke; and D.E. acknowledges partial support from the Office of Naval Research CONQUEST program. The authors would like to express their gratitude towards J. Zeuner for helpful discussions and T. Rögelsperger for the artistic input. They furthermore thank LioniX International BV for the manufacturing of the interposer waveguides used in the experiment.

#### AUTHOR CONTRIBUTIONS

I.A.C., T.S., D.R.M.A.-S., L.A.R. and P.W. designed the experiment, analyzed the results, and wrote the paper. I.A.C., T.S., and L.A.R. performed the measurements. D.R.M.A.-S. and C.H.W.B. provided theoretical support. V.S. and C.G. built the telecom photon pair source. N.C.H., J.C., M.H., T.B.-J., and D.E. fabricated and characterized the nanophotonic processor. All authors read and commented on the paper.

#### ADDITIONAL INFORMATION

**Competing interests:** The authors declare no competing interests.

**Publisher's note:** Springer Nature remains neutral with regard to jurisdictional claims in published maps and institutional affiliations.

#### REFERENCES

- Dicke, R. H. Interaction-free quantum measurements: a paradox? *Am. J. Phys.* **49**, 925–930 (1981).
- Elitzur, A. C. & Vaidman, L. Quantum mechanical interaction-free measurements. *Found. Phys.* **23**, 987–997 (1993).
- Degasperis, A., Fonda, L. & Ghirardi, G. C. Does the lifetime of an unstable system depend on the measuring apparatus? *Il Nuovo Cim. A (1965–1970)* **21**, 471–484 (1974).
- Mista, B. & Sudarshan, E. C. G. The zeno's paradox in quantum theory. *J. Math. Phys.* **18**, 756–763 (1977).
- Kwiat, P., Weinfurter, H., Herzog, T., Zeilinger, A. & Kasevich, M. A. Interaction-free measurement. *Phys. Rev. Lett.* **74**, 4763–4766 (1995).
- Kwiat, P. G. et al. High-efficiency quantum interrogation measurements via the quantum zeno effect. *Phys. Rev. Lett.* **83**, 4725–4728 (1999).
- Hosten, O., Rakher, M. T., Barreiro, J. T., Peters, N. A. & Kwiat, P. G. Counterfactual quantum computation through quantum interrogation. *Nature* **439**, 949–952 (2006).
- Noh, T.-G. Counterfactual quantum cryptography. *Phys. Rev. Lett.* **103**, 230501 (2009).
- Yin, Z.-Q., Li, H.-W., Chen, W., Han, Z.-F. & Guo, G.-C. Security of counterfactual quantum cryptography. *Phys. Rev. A* **82**, 042335 (2010).
- Liu, X. et al. Eavesdropping on counterfactual quantum key distribution with finite resources. *Phys. Rev. A* **90**, 022318 (2014).
- Salih, H., Li, Z.-H., Al-Amri, M. & Zubairy, M. S. Protocol for direct counterfactual quantum communication. *Phys. Rev. Lett.* **110**, 170502 (2013).
- Arvidsson-Shukur, D. R. M. & Barnes, C. H. W. Quantum counterfactual communication without a weak trace. *Phys. Rev. A* **94**, 062303 (2016).
- Gao, Y. et al. Direct counterfactual communication via quantum zeno effect. *Proc. Natl Acad. Sci.* **114**, 4920–4924 (2017).
- Arvidsson-Shukur, D. R. & Barnes, C. H. Postselection and counterfactual communication. *Phys. Rev. A* **99**, 060102 (2019).
- Arvidsson-Shukur, D. R. M., Gottfrieds, A. N. O. & Barnes, C. H. W. Evaluation of counterfactuality in counterfactual communication protocols. *Phys. Rev. A* **96**, 062316 (2017).
- Danan, A., Farfurnik, D., Bar-Ad, S. & Vaidman, L. Asking photons where they have been. *Phys. Rev. Lett.* **111**, 240402 (2013).
- Vaidman, L. Past of a quantum particle. *Phys. Rev. A* **87**, 052104 (2013).
- Vaidman, L. Reply to comment on 'past of a quantum particle'. *Phys. Rev. A* **88**, 046103 (2013).
- Vaidman, L. Comment on protocol for direct counterfactual quantum communication. *Phys. Rev. Lett.* **112**, 208901 (2014).
- Li, Z.-H., Al-Amri, M. & Zubairy, M. S. Comment on past of a quantum particle. *Phys. Rev. A* **88**, 046102 (2013).
- Salih, H., Li, Z.-H., Al-Amri, M. & Zubairy, M. S. Salih et al. reply. *Phys. Rev. Lett.* **112**, 208902 (2014).
- Li, Z.-H., Al-Amri, M. & Zubairy, M. S. Direct counterfactual transmission of a quantum state. *Phys. Rev. A* **92**, 052315 (2015).
- Aharonov, Y. & Vaidman, L. Modification of counterfactual communication protocols that eliminates weak particle traces. *Phys. Rev. A* **99**, 010103 (2019).
- Salih, H., McCutcheon, W. & Rarity, J. Do the laws of physics prohibit counterfactual communication? Preprint at arXiv: 1806.01257 (2018).
- Harris, N. C. et al. Quantum transport simulations in a programmable nanophotonic processor. *Nat. Photonics* **11**, 447 (2017).
- Shannon, C. A mathematical theory of communication. *Bell Syst. Tech. J.* **27**, 379–423 (1948).
- Greganti, C. et al. Tuning single-photon sources for telecom multi-photon experiments. *Opt. Express* **26**, 3286–3302 (2018).
- Broome, M. A., Almeida, M. P., Fedrizzi, A. & White, A. G. Reducing multi-photon rates in pulsed down-conversion by temporal multiplexing. *Opt. Express* **19**, 22698–22708 (2011).
- Natarajan, C. M., Tanner, M. G. & Hadfield, R. H. Superconducting nanowire single-photon detectors: physics and applications. *IOPscience* **25**, 063001 (2012).
- Marsili, F. et al. Detecting single infrared photons with 93% system efficiency. *Nat. Photon.* **7**, 210–214 (2013).



**Open Access** This article is licensed under a Creative Commons Attribution 4.0 International License, which permits use, sharing, adaptation, distribution and reproduction in any medium or format, as long as you give appropriate credit to the original author(s) and the source, provide a link to the Creative Commons license, and indicate if changes were made. The images or other third party material in this article are included in the article's Creative Commons license, unless indicated otherwise in a credit line to the material. If material is not included in the article's Creative Commons license and your intended use is not permitted by statutory regulation or exceeds the permitted use, you will need to obtain permission directly from the copyright holder. To view a copy of this license, visit <http://creativecommons.org/licenses/by/4.0/>.

© The Author(s) 2019

### 7.3 Giant enhancement of third-harmonic generation in graphene-metal heterostructures

We have seen that currently photonic quantum computing is limited by the probabilistic nature of available single-photon sources and quantum logic gates. However, we also know that these drawbacks could be overcome with strong nonlinear effects at the single-photon level. As an alternative to standard nonlinear crystals mostly used in spontaneous parametric down-conversion (SPDC) systems, here we study the optical nonlinear enhancement in graphene heterostructures. These devices consist of gold nanoribbons deposited on top of planar graphene. We find that the excitation of metallic plasmons in the nanoribbons leads to a large field confinement that, at the same time, interacts with the graphene nonlinearity, providing a THG signal enhancement three orders of magnitude stronger than that measured in bare planar graphene.

In this paper we also change the Fermi energy of the system via electrical doping and observe a THG signal, which according to the theoretical model, could be explained by the excitation of graphene plasmons.

For further understanding this topic, I recommend reading Sections 4.2-Optical properties of graphene, 2.2-Nonlinear Optics and 3-Fundamentals of Plasmonics.

## Giant enhancement of third-harmonic generation in graphene-metal heterostructures

I. Alonso Calafell\*,<sup>1</sup> L. A. Rozema,<sup>1</sup> D. Alcaraz Iranzo,<sup>2</sup> A. Trenti,<sup>1</sup> J. D. Cox,<sup>3,4</sup>  
 A. Kumar,<sup>2</sup> H. Bieliaiev,<sup>1</sup> S. Nanot,<sup>2,5</sup> C. Peng,<sup>6</sup> D. K. Efetov,<sup>6</sup> J. Y. Hong,<sup>6</sup> J.  
 Kong,<sup>6</sup> D. Englund,<sup>6</sup> F. J. García de Abajo,<sup>2,7</sup> F. H. L. Koppens,<sup>2</sup> and P. Walthers<sup>1</sup>

<sup>1</sup>Vienna Center for Quantum Science and Technology (VCQ), Faculty of Physics,  
 University of Vienna, Boltzmannngasse 5, Vienna A-1090, Austria

<sup>2</sup>ICFO-Institut de Ciències Fotoniques, The Barcelona Institute of  
 Science and Technology, 08860 Castelldefels (Barcelona), Spain

<sup>3</sup>Center for Nano Optics, University of Southern Denmark, Campusvej 55, DK-5230 Odense M, Denmark

<sup>4</sup>Danish Institute for Advanced Study, University of Southern Denmark, Campusvej 55, DK-5230 Odense M, Denmark

<sup>5</sup>Laboratoire Charles Coulomb (L2C), Université de Montpellier, CNRS, 34095 Montpellier Cedex, France

<sup>6</sup>Quantum Photonics Group, RLE, Massachusetts Institute of Technology, Cambridge, Massachusetts 02139, USA

<sup>7</sup>ICREA-Institució Catalana de Recerca i Estudis Avançats,

Passeig Lluís Companys 23, 08010 Barcelona, Spain

(Dated: May 4, 2020)

Nonlinear nanophotonics leverages the spectral and spatial control of optical fields achieved through engineered nanostructures to funnel light into small volumes and enhance its intensity in nonlinear materials. The intrinsically large and electrically tunable nonlinear optical response of graphene, together with its ability to strongly concentrate optical fields, make it a promising candidate for nonlinear optoelectronic applications such as switches and frequency converters. Here we report unprecedentedly strong optical nonlinearities in graphene-insulator-metal heterostructures, demonstrating an enhancement of three orders of magnitude in the third-harmonic signal compared to bare graphene. Furthermore, by increasing the graphene Fermi energy through an external gate voltage, we find multiple peaks and dips in the nonlinear signal that are consistent with the mediation of graphene plasmons in the nonlinear signal. Our findings demonstrate that graphene-insulator-metal heterostructures are a promising building block for optically-controlled ultra-fast miniaturised nano-optoelectronic components enabled by tunable and ultra-strong nonlinear light-matter interactions.

The ability to concentrate light into nanometric volumes enables access to an ultrastrong light-matter coupling regime that opens applications in fields ranging from optical sensing<sup>1</sup> to quantum information processing.<sup>2</sup> In this context, metallic nanostructures supporting plasmons - the collective electron oscillations - can concentrate electromagnetic fields, and they have even been demonstrated to enhance nonlinear optical processes.<sup>3</sup> While the properties of plasmons can be tailored by the shape, size, and composition of their supporting conductive media,<sup>4</sup> these properties are notoriously difficult to actively tune in noble metals.<sup>5-9</sup> Furthermore, noble metals suffer from large intrinsic ohmic losses that limit their nonlinear optical response and coherence lifetime.<sup>10</sup> Over the last decade, graphene has been shown to have an intrinsically large and tunable optical nonlinearity associated with third-harmonic generation (THG),<sup>11-14</sup> four-wave mixing,<sup>12,15,16</sup> the optical Kerr effect,<sup>17,18</sup> and high-harmonic generation.<sup>19,20</sup> While the nonlinear optical response of graphene is comparatively intense when normalized per carbon atom, its atomic thickness presents an inherent limitation to the light-matter interaction volume.

Here we use a heterostructure consisting of graphene, an insulator spacer, and nanometer-thick gold nanoribbons to concentrate the electric field of a far-field pump beam into graphene. We experimentally find that the gold structures act as antennas that increase the THG by three orders of magnitude above that of bare graphene.

We confirm that the THG originates entirely in the graphene layer, which enables us to actively tune the enhanced nonlinear signal by simply controlling the Fermi energy of graphene via an externally applied voltage.

In addition to its intrinsic nonlinearity, graphene supports highly-confined and long-lived plasmonic excitations that can be electrically tuned over a wide spectral range.<sup>21-32</sup> Graphene-insulator-metal heterostructures have been used to demonstrate strong optical confinement, down to the scale of one atom,<sup>6</sup> and nearly perfect absorption of the incident field.<sup>33-35</sup> It has also been argued that such systems can reach a strong-coupling quantum regime.<sup>36-38</sup> Nonetheless, despite numerous theoretical predictions of an intense coherent nonlinear plasmonic response in graphene,<sup>36,37,39-46</sup> there are currently few experimental demonstrations of plasmon-assisted optical nonlinearities in extended<sup>47</sup> and structured<sup>48,49</sup> graphene. Our experiments display an intriguing peaks and dips in the third-harmonic signal as a function of the carrier concentration. We find that a model wherein graphene surface plasmon polaritons are excited by the gold nanoribbons is consistent with the experimental observations, whereas elimination of plasmons from the model results in poor agreement. These signatures of plasmon-enhanced and -suppressed third-harmonic generation provide a new route toward the amplification and control of light at strong subwavelength dimensions.

*Experiment*– Our samples consist of a graphene sheet

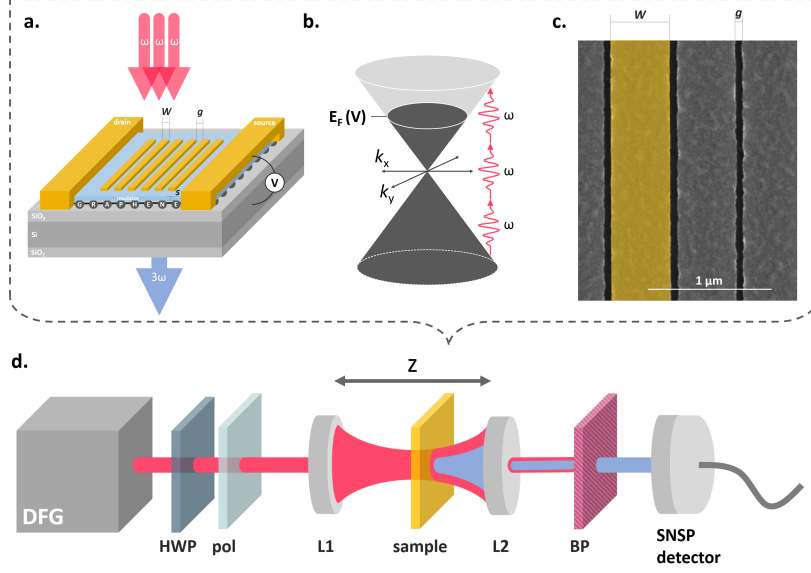


Figure 1. **Gate-tunable graphene heterostructures.** **a.** Graphene is encapsulated by a few-nm-thick  $\text{Al}_2\text{O}_3$  or a monolayer h-BN film, setting the space  $s$  between the graphene and the gold nanoribbons. The nanoribbons are characterized by their width  $W$  and gap  $g$ . Normally-incident pump light at a frequency  $\omega$  undergoes third-harmonic generation in the sample, and is collected in transmission. A gate voltage ( $V$ ) tunes the Fermi energy of the graphene  $E_F$ . **b.** The conical electron dispersion relation of graphene can be tuned in resonance with one, two, or three pump photons. **c.** Scanning electron microscopy image of one of our high-quality nanoribbon arrays. **d.** Sketch of our experimental setup. Difference-frequency generation (DFG) between signal and idler beams of an optical parametric oscillator (not shown) provides mid-IR  $\approx 260$  fs pulses. A half-wave plate (HWP), together with a polarizer (pol), selectively rotate the polarization of the pump, which is then focused onto the sample. A second lens collimates the pump and the third harmonic. A band-pass filter (BP) isolates the third-harmonic signal, which is coupled into a multimode fiber and sent to a superconducting nanowire single-photon detector (SNSPD). The sample is moved in the  $z$  direction, in and out of the focal point of the beam.

with a metallic nanoribbon array separated by an insulating  $\text{Al}_2\text{O}_3$  or h-BN spacer, as depicted in Fig. 1a,b,c. In order to isolate the nonlinear signal from the heterostructure, we use a modified  $z$ -scan setup with a tight depth of focus (Fig. 1d). In our configuration, the sample is moved through the focal point of a fs-pulsed mid-IR pump beam (with a wavelength of 5500 nm or 3900 nm), and a third-harmonic signal (at 1833 nm or 1300 nm, respectively) is measured in transmission (as detailed in the Methods section). All the measurements in this work are performed under normal conditions. A set of representative  $z$ -scan measurements is presented in Fig. 2a, showing that we only observe signals from bare *graphene*, and *gold+graphene* heterostructures (see Supplementary Figure S2 for more detail). The spectrum of the nonlinear signal (with a 3900 nm pump beam) is presented in Fig. 2e, showing a clear peak at the third-harmonic wavelength. The wavelength of the THG signal with a

5500 nm pump is confirmed in supplementary Fig. S1.

Our data clearly shows that the THG signals from the heterostructures are greatly enhanced compared to bare graphene, and additional control experiments (see Supplementary Figure S2) show that the metal structures alone do not produce a measurable THG signal. Moreover, the THG signal is maximized when the polarization is perpendicular to the direction of the nanoribbons (blue squares in Fig. 2c,d). Additionally, as shown in Fig. 2d, the THG signal of bare graphene is co-polarized with the incoming light (red triangles), and the THG signal of the heterostructures is perpendicular to the nanoribbons (blue squares). In both cases, the strongly polarized signal indicates a coherent nonlinear process.

We quantify the enhancement and verify the third-order nature of our signal by measuring the power dependence of bare *graphene* (red triangles) and the *gold+graphene* heterostructures (squares), shown in Fig.

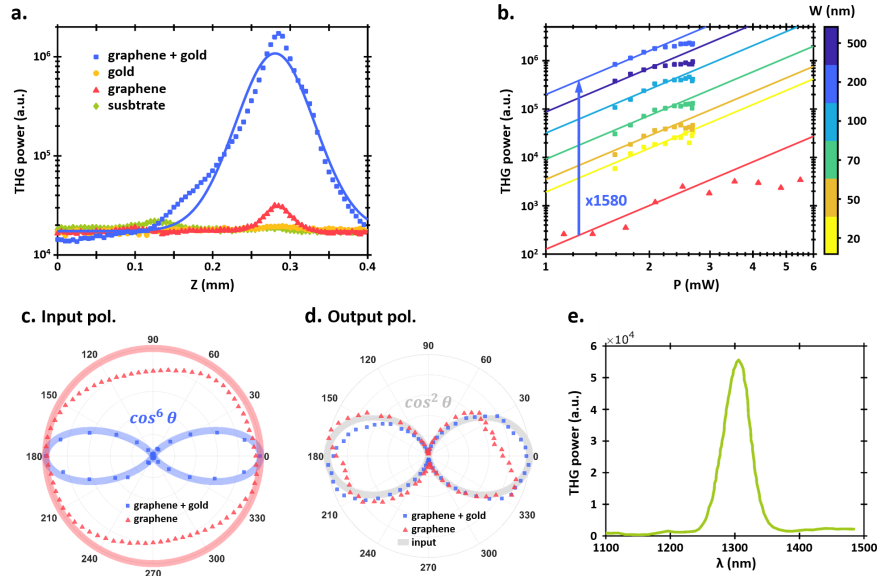
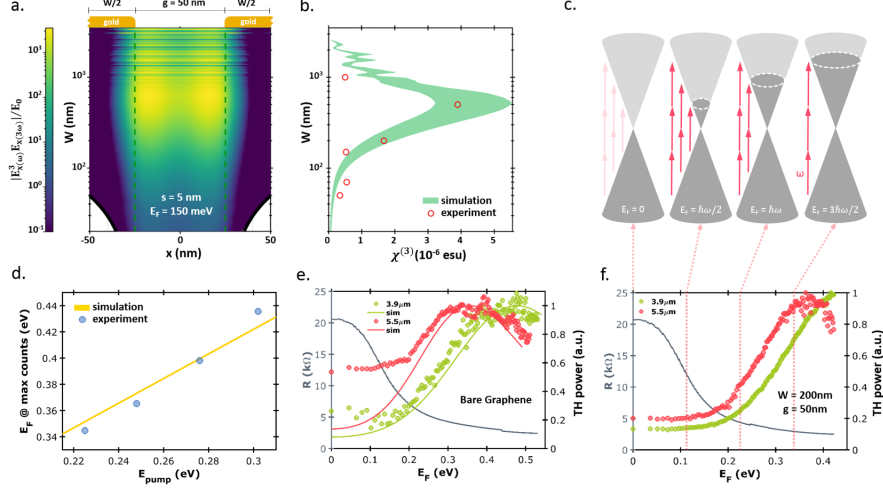


Figure 2. **Characterization of the third-harmonic signal.** **a.** Z-scan measurements on four different regions of the sample. The Gaussian fits to the data provide visual guides. **b.** Power scaling of the measured third-harmonic signal (symbols) in bare graphene and in gold-graphene heterostructures for different nanoribbon widths with a monolayer h-BN spacer. The pump wavelength for this data is 3900 nm and the Fermi energy is  $E_F \approx 150$  meV. The linear fits (lines) to these data are used to calculate the enhancement of the heterostructure over bare graphene. **c.** Third-harmonic signal of bare graphene and heterostructures when the input polarization is rotated. Bare graphene is isotropic with respect to the incident polarization, while the gold nanoribbons result in a  $\cos^6 \theta$  dependence with polarization angle  $\theta$  relative to the direction perpendicular to the ribbons (*i.e.*, as expected from a third-order power scaling). **d.** Third-harmonic emission when the input polarization is fixed, and a polarizer after the sample is rotated. For bare graphene, the third-harmonic signal is co-polarized with the input pump light, while for the heterostructures the third-harmonic polarization is always orthogonal to the nanoribbons. In both cases, the polarization of the third-harmonic signal is coherent. For the data presented in panels c and d, the pump wavelength is 5500 nm and the Fermi energy is  $E_F \approx 150$  meV. The studied heterostructure has dimensions  $s = 5$  nm,  $W = 200$  nm, and  $g = 50$  nm. **e.** Spectrum of third-harmonic generation from bare graphene, measured with a 3900 nm pump beam.

2b. The slope of the linear fits on a log-log scale is fixed to 3 and the  $y$ -intercepts are free parameters, which we use to calculate the enhancement of the heterostructures over bare graphene. Although at higher powers a small saturation effect can be observed in the *gold+graphene* data, a clear third-order power scaling is supported by the data. We experimentally find the maximum enhancement for a 3900 nm pump with a monolayer h-BN spacer and a ribbon width of  $W = 200$  nm. Under these conditions, the heterostructures produce a THG signal that is 1580 times larger than that of bare graphene.

To understand the enhancement mechanism and the role of the metal, we perform finite-difference time-domain (FDTD) simulations that are presented in Fig. 3a. These show a strong concentration of the electric field in the gap between the nanoribbons only when the polarization of the incident field is perpendicular to the

ribbons. In contrast, the bare graphene signal is independent of the incident polarization (red triangles Fig. 2c). Note that the slight asymmetry is caused by a polarization-dependent detection efficiency of our superconducting detector.<sup>50</sup> Therefore, we conclude that the enhancement is mediated by the gold nanoribbons, which amplify the electric near-field in the graphene layer. The simulations in Fig. 3a also show that the field strength in the gap depends on the width of the nanoribbons. To verify this experimentally, we performed a series of THG measurements for different nanoribbon widths, with a spacer thickness of  $s = 3$  nm and an input pump at 5500 nm (results for other spacers are shown in Fig. S4). From the THG signals we estimate an effective third-order susceptibility  $\chi^{(3)}$  as described in the Methods section. The result is shown in Fig 3b. The experimental data agree well with our FDTD simulations, which as-



**Figure 3. Third-order nonlinear susceptibility and electrical gating dependence.** **a.** Field confinement in the gap between the gold nanoribbons plotted for different nanoribbon widths. The width of the nanoribbons increases along the vertical axis from bottom to top, while the horizontal axis represents the transverse coordinate. The color plot indicates the calculated product of electric fields of the third harmonic and the pump  $E_x^3(\omega)E_x(3\omega)$ , relevant for third-harmonic generation. **b.** Effective  $\chi^{(3)}$  versus nanoribbon width. The measured  $\chi^{(3)}$  for different nanoribbon widths (red circles) is compared with the one theoretically calculated from  $|E_x^3(\omega)E_x(3\omega)|/E_0$  (solid green curve). The thickness of the theory curve shows the associated uncertainty in the estimate. The pump wavelength is 5500 nm, while we take  $E_F \approx 150$  meV,  $s = 5$  nm, and  $g = 50$  nm. In the simulations, the electron relaxation time is set to  $\tau_e = 25$  fs. **c.** Dirac cone representation of several different resonant conditions for third-harmonic generation. When  $E_F = 0$ , all three transitions are allowed but they almost cancel out, resulting in a very small THG signal. **d.** Dependence of the optimal Fermi energy on the pump wavelength. We plot the Fermi energy at which the third-harmonic signal is maximized versus the input pump energy. **e-f.** Gate dependence of the third-harmonic signal for 3900 nm and 5500 nm pump wavelengths. Panel **e** corresponds to bare graphene without nanoribbons, while **f** stands for the heterostructure with  $W = 200$  nm,  $g = 50$  nm, and  $s = 5$  nm. The red and green curves stand for the third-harmonic signals versus Fermi energy. The gray curves are the measured resistances of the sample. The peak in the resistance indicates the charge neutrality point. The red dashed lines in panel **f** indicate the one-, two-, and three-photon transitions for 5500 nm pump.

sume an uncertainty of  $\pm 20\%$  on the gap size (nominally set to 50 nm) caused by experimental imperfections.

While using gold nanribbons of the appropriate width can greatly enhance the nonlinear response of the system, this width cannot be actively changed. In contrast, the optical nonlinearity in graphene can be electrically tuned, thus providing a practical way of achieving active control. This is because the optical response in graphene depends on the strength of the intraband and interband transitions,<sup>12,14,45,51</sup> which in turn depend on the ratio of the impinging light energy  $\hbar\omega_0$  to the graphene Fermi energy  $E_F$ . The latter can be tuned in-situ by applying an external voltage to the graphene layer relative to the silicon substrate.

Conceptually, we can understand the effect of  $E_F$ -tuning on THG as illustrated in Fig. 3c. By sweeping the gate voltage, one can match the Fermi energy to be resonant to an interband transition for one, two

or three incident photons. This results in three different resonances in the third-order nonlinear susceptibility  $\chi^{(3)}$  for THG.<sup>52,53</sup> For small Fermi energies compared to the photon energy  $2E_F < \hbar\omega_0$ , all three transitions can occur; however, because they contribute to  $\chi^{(3)}$  with different signs, they nearly cancel out.<sup>12</sup> For large Fermi energies compared to the photon energy,  $2E_F > 3\hbar\omega_0$ , all three of these transitions are Pauli-blocked and there is only a non-resonant intraband contribution. As a result  $\chi^{(3)}$  becomes very small (theoretically it vanishes at zero temperature).<sup>12,14</sup> At intermediate Fermi energies  $\hbar\omega_0 < 2E_F < 3\hbar\omega_0$ , it is possible to increase THG by, for example, Pauli blocking the one-photon and two-photon transitions, so that only the three-photon transitions are allowed and the other two transitions no longer cancel it out. For low electron temperatures the gate response is expected to result in several sharp features as the system is tuned in and out of resonance. However, thermal

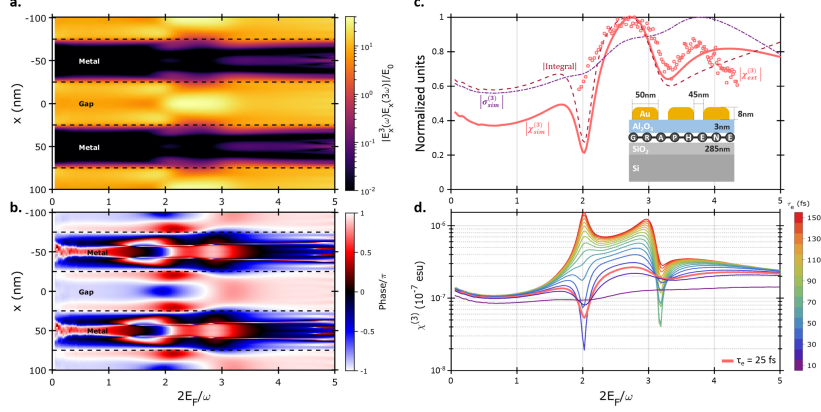


Figure 4. **The role of graphene plasmons in THG.** The third-order susceptibility  $\chi_{\text{sim}}^{(3)}$  is calculated from the integral of the simulated gate dependent spatial distribution of the nonlinear in-plane field at graphene, which is shown in **a** and **b** as amplitude and phase, respectively, for 2 periods of the structure in the inset of **c**. The electron relaxation time is set to  $\tau_e = 25$  fs and the fundamental wavelength is  $\lambda = 5.5 \mu\text{m}$ . **c**. Gate-dependent relevant response functions, normalized to their maxima: experimental (red squares) and simulated (solid green curve) third-order nonlinear susceptibility  $\chi_{\text{sim}}^{(3)}$ , third-order nonlinear conductivity  $\sigma_{\text{sim}}^{(3)}$  (dashed-dotted violet curve), and nonlinear in-plane field integral result (dashed fuchsia curve). The complex multiplication of the last two of them (see integral in Eq. 4) provides the key signatures (peaks and dips) of  $\chi_{\text{exp}}^{(3)}$  for a relaxation time  $\tau_e = 25$  fs in the model. **d**. Simulated gate-dependent third-order nonlinear susceptibility  $\chi_{\text{sim}}^{(3)}$  for various electron relaxation times  $\tau_e$ , showing stronger features for larger  $\tau_e$ , and demonstrating that our measurements are not explained by effectively excluding plasmons from the model as  $\tau_e$  is reduced down to 10 fs.

broadening turns these features into broad shoulders.

The observed THG signal as a function of  $E_F$  is shown in Fig. 3e, in this case for bare graphene, for two different pump wavelengths, 5500 nm (0.225 eV) and 3900 nm (0.318 eV).

A clear peak is observed that shifts to larger  $E_F$  for shorter wavelengths and thus larger  $\hbar\omega_0$ . In order to better visualize this wavelength shift, we normalize both curves to the same maximum. This is more clearly revealed in Fig. 3d, where we plot the Fermi energy at which the THG is maximized versus the pump wavelength. As we show in the Supplementary Information, the exact location of the maximum Fermi energy is affected by the electron temperature, which depends on the pump fluence. Importantly, these gating data show that we can actively modulate the THG signal in bare graphene. While the electron temperature and electron relaxation time affect the degree to which the THG signal can be modulated, we can change the intensity of the THG by a factor  $\approx 5$  for bare graphene.

Similar gating measurements on the heterostructure are shown in Fig. 3f, for the geometry in which we obtain a maximum field enhancement ( $W = 200$  nm,  $g = 50$  nm). Once again, we observe the expected shift as a function of the energy of the incident photons. We can modulate the THG by a factor of  $7.4 \pm 0.2$  with a

3900 nm pump, and by a factor of  $4.7 \pm 0.2$  with a 5500 nm pump. We stress that this active tunability comes from the unique combination of atomic thickness and linear electronic dispersion in graphene, which cannot be achieved in standard noble metal plasmonics.<sup>3</sup>

Interestingly, the THG signal for a much larger range of  $E_F$  reveals two peaks and a dip in the gate response as shown in Fig. 4c for a heterostructure with parameters  $W = 55$  nm,  $g = 45$  nm. To provide a possible interpretation, we note that the graphene third-order nonlinearity associated with THG is determined by the interplay between the third-order nonlinear graphene conductivity  $\sigma_{3\omega}^{(3)}$  and the nonlinear field integral  $\int_L E_x(\omega)^3 E_x(3\omega) dx$  (*i.e.*, the cubic of the linear field is associated with the THG current amplitude, while the field at  $3\omega$  represents the enhancement in the emission produced by the heterostructure at the THG frequency). We also note that tuning the Fermi level to higher energies can lead to the excitation of (acoustic) graphene plasmons<sup>6</sup> that can affect the non-linear response. The third-order conductivity  $\sigma_{3\omega}^{(3)}$  depends on the excitation frequency  $\omega$ , Fermi energy  $E_F$ , the electron relaxation time  $\tau_e$ , and electron temperature  $T_e$  associated with the pump absorption. The latter can reach high values relative to the ambient room temperature and can cause anomalous behavior

such as shifts in the features of the optical conductivity as a function of doping, compared to constant  $T_e$  (see Supplementary Figure 4). The second contribution (fields integral) depends only on the spatial field distribution, which is a consequence of varying the linear graphene conductivity with  $E_F$ . This in turn modifies the plasmon wavelength differently in the gap and below the metal regions (see simulations in Fig 4 a,b). Obviously, different spatial regions can produce contributions of different sign that cancel each other, thus affecting the overall nonlinear performance.

It is thus important to stress that, as we show in the Fig. 4c, the third-order conductivity alone, despite its rich dependence on these parameters, cannot fully explain the observed THG signal. However, the peaks and dips appearing in the response at specific values of  $2E_F/h\nu$  correlate well with the integral of the electric fields, stemming in part from plasmonic interferences, and driving the nonlinear response. This integral, shown as a dashed line in Fig. 4c, is found to exhibit the same trend as the data. The situation is further complicated by absorption from the pump, which increases the electron temperature  $T_e$ , leading to the shifts noted above (see Supplementary Information).

From our simulations, we conclude that the nonlinear response in our experiment is mainly driven by the field in the gap region where it takes comparatively larger values (see Fig 4a). In particular, at  $\lambda = 5500$  nm, for  $W = 55$  nm,  $g = 45$  nm, and  $s = 3$  nm, we find a dip at  $\sim 3 \times 2E_F/h\nu$  and a peak at slightly larger  $E_F$ . The dip in the data can then be interpreted as the partial cancellation of positive and negative complex field components throughout the whole period, which produces a reduction of the observed  $\chi^{(3)}$ . More precisely, it appears that at the dip the acoustic plasmon field partially cancels out the field in the gap. This is modeled well in our simulations with  $\tau_e = 25$  fs. However, for larger values of  $\tau_e$ , the acoustic plasmon field seems to overcome the field in the gap, thus turning the dips in the THG signal into peaks (Fig 4d).

A quantitative comparison of the calculated and measured  $\chi^{(3)}$  is shown in Fig. 4c, and the main features are clearly reproduced by the model. An alternative simulation in which graphene plasmons are explicitly suppressed by decreasing the plasmon lifetime  $\tau_e$  is unable to reproduce the dips and peaks in our data (see the purple curve in Figure 4d), thus suggesting the excitation of plasmons in our graphene heterostructures as a mechanism assisting THG. Nevertheless, further studies are needed to rigorously confirm the effect of these surface plasmon polaritons on the graphene optical nonlinearity.

*Conclusion*—Recent studies have reported a wide range in the estimate of  $\chi^{(3)}$  using third-harmonic generation.<sup>11–13,54–56</sup> In our experiment, we find an effective third-order susceptibility of  $\chi^{(3)} \approx 10^{-7}$  esu in bare graphene, consistent with the highest values reported in the literature. Moreover, our experimental measurements agree well with simulations based on the third-

order nonlinear conductivity taken from Refs. [45,57]. Remarkably, by calculating an effective nonlinearity for the 200 nm heterostructure with a monolayer h-BN spacer we find  $\chi_{\text{exp}}^{(3)} \approx 5.6 \times 10^{-6}$  esu, which is larger than any value ever reported for THG in graphene.<sup>54</sup>

Unlike in metal plasmonics, we can actively modulate the nonlinearity of our graphene heterostructures by controlling  $E_F$  with an external gate voltage. Graphene-based linear optical devices have already been shown to operate at GHz speeds<sup>58</sup> and hence, our system provides a new route toward ultrafast nonlinear optoelectronic switches and frequency converters. Additionally, our measurements reveal intriguing plasmonic effects supported by simulations in which graphene surface plasmon polaritons appear to directly modify the nonlinear optical response of our structures. These plasmonic excitations potentially provide a novel approach to the manipulation and amplification of light at subwavelength scales. In particular, our simulations suggest that improving the plasmon lifetime by a factor of five would increase the nonlinear response by an order of magnitude. This suggests that graphene plasmonic devices could provide unprecedentedly strong nonlinearities, potentially resulting in nonlinear optical effects at the single-photon level.<sup>2,36,38</sup>

#### DATA AVAILABILITY

The datasets generated and analysed during the current study are available from the corresponding author if you ask nicely.

#### CODE AVAILABILITY

The simulations codes generated for the current study are available from the corresponding author if you ask nicely.

#### AUTHOR'S CONTRIBUTIONS

I.A.C., L.A.R., F.H.L.K. and A.T. designed the experiment, performed the measurements and analysed the results. I.A.C., L.A.R., D.A.I., F.H.L.K. and J.D.C. wrote the manuscript. D.A.I., S.N., A.K. and F.H.L.K. fabricated and characterized the samples. D.A.I., J.D.C., H.B. and F.J.G.A. provided theoretical support and simulations. P.W., F.H.L.K. and F.J.G.A. supervised the project. All authors read and commented on the manuscript.

#### ACKNOWLEDGMENTS

The authors thank Simone Zanotto for assistance with the Matlab code. We acknowledge support from the Eu-

ropean Commission through ErBeSta (No. 800942), the Austrian Research Promotion Agency (FFG) through the QuantERA ERA-NET Cofund project HiPhoP, from the Austrian Science Fund (FWF) through CoQuS (W 1210-N25), NaMuG (P30067-N36) and BeyondC (F 7113-N38), the U.S. Air Force Office of Scientific Research (FA2386-233 17-1-4011), Red Bull GmbH, the University of Southern Denmark (SDU 2020 funding), the ERC (Advanced Grant 789104-eNANO), the Spanish MINECO (MAT2017-88492-R and SEV2015-0522), the European Commission (Graphene Flagship 696656), the Catalan CERCA, Fundació Privada Cellex, the Government of Catalonia through the SGR grant, and from the Spanish Ministry of Economy and Competitiveness, through the “Severo Ochoa” Programme for Centres of Excellence in R&D (SEV-2015-0522), support by Fundació Cellex Barcelona, Generalitat de Catalunya through the CERCA program, and the Mineco grants Plan Nacional (FIS2016-81044-P) and the Agency for Management of University and Research Grants (AGAUR) 2017 SGR 1656. Furthermore, the research leading to these results has received funding from the European Union Seventh Framework Programme under grant agreement no.785219 Graphene Flagship, and project Grasp (GA:613024). I.A.C. acknowledges support from the University of Vienna via the Vienna Doctoral School. L.A.R. acknowledges support from the Templeton World Charity Foundation (fellowship no. TWCF0194). D.A.I. acknowledges support from the Spanish MINECO FPI Grant (BES-2014-068504). A.T. acknowledges support from the European Union’s Horizon 2020 research and innovation programme under the Marie Skłodowska-Curie grant agreement No 801110 and the Austrian Federal Ministry of Education, Science and Research (BMBWF). J.D.C. was supported by VILLUM Fonden (grant No. 16498). It reflects only the author’s view, the EU Agency is not responsible for any use that may be made of the information it contains.

## METHODS

**Experimental details**— We carry out our THG measurements using a modified z-scan setup, where the TH signal is measured while the sample is moved along the z axis through the focus of the laser beam (see Fig. 1d). Our pump beam consists of linearly-polarized pulses of  $\sim 260$  fs duration with a tunable carrier wavelength of  $5.5 \mu\text{m}$  (0.225 eV) at a 80 MHz repetition rate, which we create by performing Difference-Frequency Generation (DFG) between the signal and the idler beams of an Optical Parametric Oscillator (OPO). We use a Half-Wave Plate (HWP) to tune the polarization of the incoming beam to that set by the polarizer (pol). By rotating the HWP and the polarizer together we can rotate the pump polarization relative to the orientation of the nanoribbons. Then, a lens with a 5.26 mm focal length focuses the pump down to a waist of  $\approx 20 \mu\text{m}$  for the

5500 nm pump and  $\approx 13 \mu\text{m}$  for the 3900 nm pump. When the sample is moved parallel to the pump beam (along the z axis), the nonlinear emission occurs most efficiently where the fluence is maximum, i.e. at the focal point. Afterwards, a lens with a 11 mm focal length collimates the beam, which is then sent through a bandpass filter (BP) to separate the THG signal from the excitation beam. Finally, the signal is coupled into a multimode fiber and sent to a large-area Superconducting Nanowire Single-Photon (SNSP) detector, with a  $\approx 20\%$  detection efficiency at the third-harmonic wavelength,  $5500/3 \text{ nm} = 1833 \text{ nm}$ .

We verify the wavelength of this signal by removing all spectral filters, keeping the sample in the focus, and using a NIREOS GEMINI interferometer to perform Fourier transform spectroscopy on the signal.

**Extracting the third-order susceptibility**— Experimentally we estimate  $\chi_{exp}^{(3)}$  starting with the expression of the input (*i*) and output (*o*) average power as a function of the field as,

$$P(\omega_{i,o}) = \frac{1}{8} \left( \frac{\pi}{\ln 2} \right)^{3/2} f \tau W^2 n_{\omega_{i,o}} \epsilon_0 c \frac{|E(\omega_{i,o})|^2}{2} \quad (1)$$

where we assume laser pulses with repetition rate  $f$ , duration  $\tau$ , waist  $W$  on the sample and Gaussian profile, and  $n_{\omega_{i,o}} = 2.4$  is the refraction index, and  $\epsilon_0$  and  $c$  are the permittivity and speed of light in vacuum.<sup>12</sup> Additionally, we can write the THG process as a function of the input and output fields as follows and solve for  $\chi_{exp}^{(3)}$ :

$$E(\omega_o) = \frac{1}{4} \frac{i\omega_i}{2\pi c} \chi_{exp}^{(3)} d_{gr} E(\omega_i)^3 \quad (2)$$

where  $\omega_i = \omega_o/3$  and  $d_{gr} = 0.33 \text{ nm}$  is the effective thickness of graphene.

**Simulating the third-order susceptibility**— To simulate the third-order susceptibility we begin with the expression

$$\chi_{sim}^{(3)} = \left| \frac{\alpha^{(3)}}{d_{gr} L} \right| \quad (3)$$

where  $\alpha^{(3)}$  is third-order polarizability given by

$$\alpha^{(3)} = \frac{i\sigma_\omega^{(3)}}{3\omega_i} \int_L E_x(\omega)^3 E_x(3\omega) dx \quad (4)$$

and  $\sigma_\omega^{(3)}$  is the analytical third-order conductivity in graphene derived by Mikhailov in Ref.<sup>57</sup>, and  $L$  is the length of the simulated region used for integration along the direction perpendicular to the nanoribbon width. Eq. (4) represents the contribution of the THG current to the far field. In particular, the  $E_x^3(\omega)$  factor times  $\sigma_\omega^{(3)}$  is the THG current, which we represent as a polarization density at the emission frequency  $3\omega$  by multiplying by  $i/3\omega$ . Also, the factor  $E_x(3\omega)$  represents the enhancement in the emission from such polarization density depending

on the position  $x$  along the graphene film. Indeed, because of reciprocity, the latter is exactly given by the enhancement amplitude in the near field relative to free space when the structure is illuminated with  $3\omega$  radiation. More precisely, we calculate  $E_x(3\omega)$  as the complex factor of enhancement relative to the incident field in the field acting on the graphene layer when it is illuminated by a  $3\omega$  plane wave impinging from the detector direction. The electric fields  $E_x(\omega)$  entering the above expression are obtained using a RCWA (Rigorous Coupled Wave Analysis) Ref.<sup>59–61</sup> Matlab script Ref.<sup>62,63</sup> and adapted to include graphene as an interface material adopting the nonlocal 2D optical conductivity of graphene  $\sigma(Q, \omega)$  that depends on the chemical potential  $\mu$  and electronic temperature  $T_e$ . It requires periodicity of the structure perpendicular to the layered dimension. Here we consider the influence of electronic heating by the pump pulse in the optical response of the graphene-metal hybrid system. In particular, following the procedure in Ref.,<sup>64</sup> we make use of the implicit relation between  $E_F$ ,  $T_e$ , and  $\mu$

obtained from conservation of doping charge,

$$\left(\frac{E_F}{k_B T_e}\right)^2 = 2 \int_0^\infty dx x \left[ \left(e^{x-\mu/k_B T_e} + 1\right)^{-1} - \left(e^{x+\mu/k_B T_e} + 1\right)^{-1} \right], \quad (5)$$

along with the graphene heat capacity

$$F = \beta \frac{(k_B T)^3}{(\hbar v_F)^3}, \quad (6)$$

where  $F$  is the energy of the pulse absorbed (i.e.,  $F = \eta F_0$  where  $\eta$  is the absorbed fraction of power as obtained from the linear RCWA simulations) and

$$\beta = \frac{2}{\pi} \left\{ \int_0^\infty dx x^2 \left[ \left(e^{x+\mu/k_B T_e} + 1\right)^{-1} + \left(e^{x-\mu/k_B T_e} + 1\right)^{-1} \right] - \frac{1}{3} \left(\frac{E_F}{k_B T_e}\right)^3 \right\}, \quad (7)$$

to obtain the  $\mu$  and  $T_e$  satisfying the above relations simultaneously; these values are then inserted into the graphene linear conductivity directly, and for the non-linear conductivity we compute the temperature dependence using Maldague's identity:<sup>65</sup>

$$\sigma^{(3)}(\omega, \tau, \mu, T) = \frac{1}{4k_B T} \int_{-\infty}^\infty dE \frac{\sigma^{(3)}(\omega, \tau, \mu, 0)}{\cosh^2\left(\frac{E-\mu}{2k_B T}\right)}. \quad (8)$$

- 
- <sup>1</sup> Choi, I. & Choi, Y. Plasmonic nanosensors: review and prospect. *IEEE Journal of Selected Topics in Quantum Electronics* **18**, 1110–1121 (2011).
- <sup>2</sup> Tame, M. S. *et al.* Quantum plasmonics. *Nature Physics* **9**, 329–340 (2013).
- <sup>3</sup> Kauranen, M. & Zayats, A. V. Nonlinear plasmonics. *Nat. Photon.* **6**, 737–748 (2012).
- <sup>4</sup> Stockman, M. I. Nanoplasmonics: The physics behind the applications. *Phys. Today* **64**, 39–44 (2011).
- <sup>5</sup> Chikkaraddy, R. *et al.* Single-molecule strong coupling at room temperature in plasmonic nanocavities. *Nature* **535**, 127 (2016).
- <sup>6</sup> Iranzo, D. A. *et al.* Probing the ultimate plasmon confinement limits with a van der Waals heterostructure. *Science* **360**, 291–295 (2018).
- <sup>7</sup> Sando, G. M., Berry, A. D., Campbell, P. M., Baronavski, A. P. & Owrutsky, J. C. Surface plasmon dynamics of high-aspect-ratio gold nanorods. *Plasmonics* **2**, 23–29 (2007).
- <sup>8</sup> Abd El-Fattah, Z. M. *et al.* Plasmonics in atomically thin crystalline silver films. *ACS Nano* **13**, 7771–7779 (2019).
- <sup>9</sup> Echarri, A. R., Cox, J. D. & de Abajo, F. J. G. Quantum effects in the acoustic plasmons of atomically thin heterostructures. *Optica* **6**, 630–641 (2019).
- <sup>10</sup> Maier, S. A. *Plasmonics: fundamentals and applications* (Springer Science & Business Media, 2007).
- <sup>11</sup> Kumar, N. *et al.* Third harmonic generation in graphene and few-layer graphite films. *Physical Review B* **87**, 121406 (2013).
- <sup>12</sup> Jiang, T. *et al.* Gate-tunable third-order nonlinear optical response of massless Dirac fermions in graphene. *Nature Photonics* (2018).
- <sup>13</sup> Hong, S.-Y. *et al.* Optical third-harmonic generation in graphene. *Physical Review X* **3**, 021014 (2013).
- <sup>14</sup> Soavi, G. *et al.* Broadband, electrically tunable third-harmonic generation in graphene. *Nature nanotechnology* **1** (2018).
- <sup>15</sup> Hendry, E., Hale, P. J., Moger, J., Savchenko, A. K. & Mikhailov, S. A. Coherent nonlinear optical response of graphene. *Phys. Rev. Lett.* **105**, 097401 (2010).
- <sup>16</sup> Ciesielski, R. *et al.* Graphene near-degenerate four-wave mixing for phase characterization of broadband pulses in ultrafast microscopy. *Nano Letters* **15**, 4968–4972 (2015).
- <sup>17</sup> Zhang, Y.-X., Zhang, Y. & Mølmer, K. Directional launching of surface plasmons by polariton superradiance. *ArXiv* **1807.03682** (2018).
- <sup>18</sup> Dremetsika, E. *et al.* Measuring the nonlinear refractive index of graphene using the optical Kerr effect method. *Optics Letters* **41**, 3281–3284 (2016).
- <sup>19</sup> Yoshikawa, N., Tamaya, T. & Tanaka, K. High-harmonic generation in graphene enhanced by elliptically polarized

- light excitation. *Science* **356**, 736–738 (2017).
- <sup>20</sup> Baudisch, M. *et al.* Ultrafast nonlinear optical response of dirac fermions in graphene. *Nat. Commun.* **9**, 1018 (2018).
- <sup>21</sup> Hwang, E. & Sarma, S. D. Dielectric function, screening, and plasmons in two-dimensional graphene. *Physical Review B* **75**, 205418 (2007).
- <sup>22</sup> Wunsch, B., Stauber, T., Sols, F. & Guinea, F. Dynamical polarization of graphene at finite doping. *New Journal of Physics* **8**, 318 (2006).
- <sup>23</sup> Jablan, M., Soljačić, M. & Buljan, H. Plasmons in graphene: fundamental properties and potential applications. *Proceedings of the IEEE* **101**, 1689–1704 (2013).
- <sup>24</sup> Ju, L. *et al.* Graphene plasmonics for tunable terahertz metamaterials. *Nature nanotechnology* **6**, 630 (2011).
- <sup>25</sup> Koppens, F. H., Chang, D. E. & García de Abajo, F. J. Graphene plasmonics: A platform for strong light-matter interactions. *Nano Lett.* **11**, 3370–3377 (2011).
- <sup>26</sup> Grigorenko, A., Polini, M. & Novoselov, K. Graphene plasmonics. *Nature photonics* **6**, 749 (2012).
- <sup>27</sup> García de Abajo, F. J. Graphene plasmonics: challenges and opportunities. *Acs Photonics* **1**, 135–152 (2014).
- <sup>28</sup> Yan, H. *et al.* Infrared spectroscopy of tunable dirac terahertz magneto-plasmons in graphene. *Nano letters* **12**, 3766–3771 (2012).
- <sup>29</sup> Fei, Z. *et al.* Infrared nanoscopy of dirac plasmons at the graphene-sio2 interface. *Nano letters* **11**, 4701–4705 (2011).
- <sup>30</sup> Yan, H. *et al.* Tunable infrared plasmonic devices using graphene/insulator stacks. *Nature nanotechnology* **7**, 330 (2012).
- <sup>31</sup> Chen, J. *et al.* Optical nano-imaging of gate-tunable graphene plasmons. *Nature* **487**, 77–81 (2012).
- <sup>32</sup> Fei, Z. *et al.* Gate-tuning of graphene plasmons revealed by infrared nano-imaging. *Nature* **487**, 82 (2012).
- <sup>33</sup> Lee, I.-H., Yoo, D., Avouris, P., Low, T. & Oh, S.-H. Graphene acoustic plasmon resonator for ultrasensitive infrared spectroscopy. *Nature nanotechnology* **14**, 313 (2019).
- <sup>34</sup> Thongrattanasiri, S., Koppens, F. H. & De Abajo, F. J. G. Complete optical absorption in periodically patterned graphene. *Physical review letters* **108**, 047401 (2012).
- <sup>35</sup> Kim, S. *et al.* Electronically tunable perfect absorption in graphene **18**, 971–979 (2018).
- <sup>36</sup> Gullans, M., Chang, D. E., Koppens, F. H. L., García de Abajo, F. J. & Lukin, M. D. Single-photon nonlinear optics with graphene plasmons. *Phys. Rev. Lett.* **111**, 247401 (2013).
- <sup>37</sup> Jablan, M. & Chang, D. E. Multiplasmon absorption in graphene. *Phys. Rev. Lett.* **114**, 236801 (2015).
- <sup>38</sup> Alonso Calafell, I. *et al.* Quantum computing with graphene plasmons. *npj Quantum Information* **5**, 37 (2019).
- <sup>39</sup> Mikhailov, S. A. Theory of the giant plasmon-enhanced second-harmonic generation in graphene and semiconductor two-dimensional electron systems. *Phys. Rev. B* **84**, 045432 (2011).
- <sup>40</sup> Gorbach, A. V. Nonlinear graphene plasmonics: Amplitude equation for surface plasmons. *Phys. Rev. A* **87**, 013830 (2013).
- <sup>41</sup> Yao, X., Tokman, M. & Belyanin, A. Efficient nonlinear generation of thz plasmons in graphene and topological insulators. *Phys. Rev. Lett.* **112**, 055501 (2014).
- <sup>42</sup> Cox, J. D. & García de Abajo, F. J. Electrically tunable nonlinear plasmonics in graphene nanoislands. *Nat. Comm.* **6725**, 5725 (2014).
- <sup>43</sup> Manzoni, M. T., Silveiro, I., García de Abajo, F. J. & Chang, D. E. Second-order quantum nonlinear optical processes in single graphene nanostructures and arrays. *New J. Phys.* **17**, 083031 (2015).
- <sup>44</sup> Cox, J. D., Marini, A. & García de Abajo, F. J. Plasmon-assisted high-harmonic generation in graphene. *Nat. Commun.* **8**, 14380 (2017).
- <sup>45</sup> Rostami, H., Katsnelson, M. I. & Polini, M. Theory of plasmonic effects in nonlinear optics: The case of graphene. *Phys. Rev. B* **95**, 035416 (2017).
- <sup>46</sup> Hafez, H. A. *et al.* Extremely efficient terahertz high-harmonic generation in graphene by hot dirac fermions. *Nature* **561**, 507 (2018).
- <sup>47</sup> Constant, T. J., Hornett, S. M., Chang, D. E. & Hendry, E. All-optical generation of surface plasmons in graphene. *Nat. Phys.* **12**, 124–127 (2016).
- <sup>48</sup> Jadidi, M. M. *et al.* Nonlinear terahertz absorption of graphene plasmons. *Nano Lett.* **16**, 2734–2738 (2016).
- <sup>49</sup> Kundys, D. *et al.* Nonlinear light mixing by graphene plasmons. *Nano Lett.* **18**, 282–287 (2018).
- <sup>50</sup> Natarajan, C. M., Tanner, M. G. & Hadfield, R. H. Superconducting nanowire single-photon detectors: physics and applications. *Superconductor science and technology* **25**, 063001 (2012).
- <sup>51</sup> Mikhailov, S. A. Quantum theory of the third-order nonlinear electrodynamic effects of graphene. *Phys. Rev. B* **93**, 085403 (2016).
- <sup>52</sup> Cheng, J., Vermeulen, N. & Sipe, J. Third order optical nonlinearity of graphene. *New Journal of Physics* **16**, 053014 (2014).
- <sup>53</sup> Cheng, J. L., Vermeulen, N. & Sipe, J. Third-order nonlinearity of graphene: Effects of phenomenological relaxation and finite temperature. *Physical Review B* **91**, 235320 (2015).
- <sup>54</sup> Saynatjoki, A. *et al.* Rapid large-area multiphoton microscopy for characterization of graphene. *ACS nano* **7**, 8441–8446 (2013).
- <sup>55</sup> Woodward, R. *et al.* Characterization of the second- and third-order nonlinear optical susceptibilities of monolayer mos<sub>2</sub> using multiphoton microscopy. *arXiv preprint arXiv:1606.08093* (2016).
- <sup>56</sup> Soavi, G. *et al.* Broadband, electrically tunable third-harmonic generation in graphene. *Nature nanotechnology* **13**, 583 (2018).
- <sup>57</sup> Mikhailov, S. A. Quantum theory of the third-order nonlinear electrodynamic effects of graphene. *Physical Review B* **93**, 085403 (2016).
- <sup>58</sup> Phare, C. T., Lee, Y.-H. D., Cardenas, J. & Lipson, M. Graphene electro-optic modulator with 30 ghz bandwidth. *Nature Photonics* **9**, 511 (2015).
- <sup>59</sup> Whittaker, D. & Culshaw, I. Scattering-matrix treatment of patterned multilayer photonic structures. *Physical Review B* **60**, 2610 (1999).
- <sup>60</sup> Li, L. Use of fourier series in the analysis of discontinuous periodic structures. *JOSA A* **13**, 1870–1876 (1996).
- <sup>61</sup> Lalanne, P. & Morris, G. M. Highly improved convergence of the coupled-wave method for tm polarization. *JOSA A* **13**, 779–784 (1996).
- <sup>62</sup> <https://es.mathworks.com/matlabcentral/fileexchange/55401-ppml-periodically-patterned-multi-layer> (31.10.2019).
- <sup>63</sup> Manceau, J.-M., Zanutto, S., Sagnes, I., Beaudoin, G. & Colombelli, R. Optical critical coupling into highly con-

Giant enhancement of third-harmonic generation in graphene-metal heterostructures

I. Alonso Calafell\*,<sup>1</sup> L. A. Rozema,<sup>1</sup> D. Alcaraz Iranzo,<sup>2</sup> A. Trenti,<sup>1</sup> J. D. Cox,<sup>3,4</sup>  
 A. Kumar,<sup>2</sup> H. Bieliaiev,<sup>1</sup> S. Nanot,<sup>2,5</sup> C. Peng,<sup>6</sup> D. K. Efetov,<sup>6</sup> J. Y. Hong,<sup>6</sup> J.  
 Kong,<sup>6</sup> D. Englund,<sup>6</sup> F. J. García de Abajo,<sup>2,7</sup> F. H. L. Koppens,<sup>2</sup> and P. Walther<sup>1</sup>

<sup>1</sup>Vienna Center for Quantum Science and Technology (VCQ), Faculty of Physics,  
 University of Vienna, Boltzmannngasse 5, Vienna A-1090, Austria

<sup>2</sup>ICFO-Institut de Ciències Fotoniques, The Barcelona Institute of  
 Science and Technology, 08860 Castelldefels (Barcelona), Spain

<sup>3</sup>Center for Nano Optics, University of Southern Denmark, Campusvej 55, DK-5230 Odense M, Denmark

<sup>4</sup>Danish Institute for Advanced Study, University of Southern Denmark, Campusvej 55, DK-5230 Odense M, Denmark

<sup>5</sup>Laboratoire Charles Coulomb (L2C), Université de Montpellier, CNRS, 34095 Montpellier Cedex, France

<sup>6</sup>Quantum Photonics Group, RLE, Massachusetts Institute of Technology, Cambridge, Massachusetts 02139, USA

<sup>7</sup>ICREA-Institució Catalana de Recerca i Estudis Avançats,  
 Passeig Lluís Companys 23, 08010 Barcelona, Spain

(Dated: January 8, 2020)

SUPPLEMENTARY INFORMATION

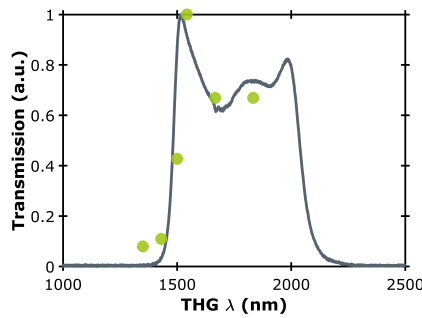


Figure 1. **Confirmation of the third-harmonic signal wavelength with a 5500 nm pump beam.** The transmission of the third-harmonic signal through a bandpass filter at 1750 nm with a 500 nm bandwidth as the pump wavelength is changed. The points are the measured transmission of the third-harmonic signal and the solid curve is the transmission of the filter measured with standard FTIR.

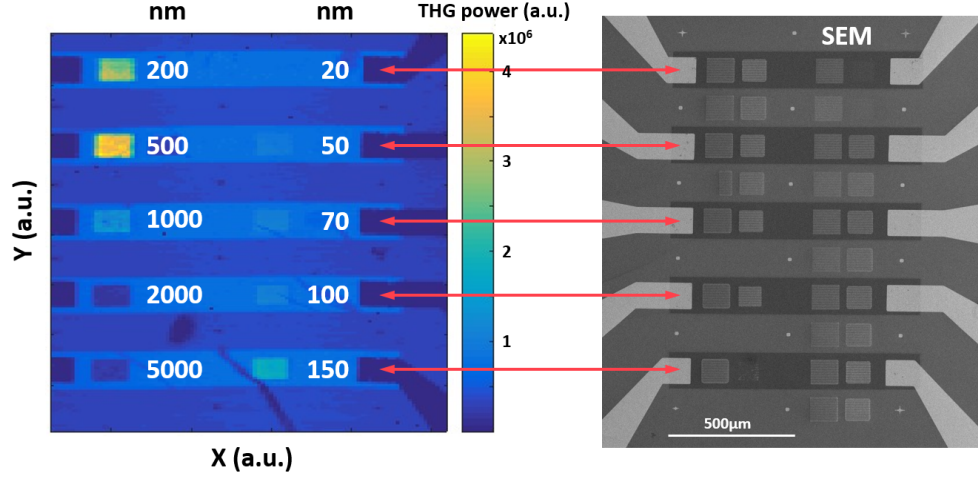


Figure 2. Comparison of the third-harmonic signal with an SEM image of the sample. The left panel shows the third-harmonic signal as the entire sample is moved transversely through the pump beam. The corresponding SEM image of the sample is shown on the right. Strong third-harmonic signals can be distinguished in the regions with both graphene and golden nanoribbons, as well as a weaker signals from the strips of bare graphene surrounding the nanoribbons. There is no discernable signal from the nanoribbons without graphene. The darker areas indicating the contacts are also evident. As a reference, the SEM image on the right hand side confirms the structure of the sample, where the dark horizontal bands indicate the presence of bare graphene. The brighter squares on top of these bands are different arrays of golden nanoribbons with widths  $W$  ranging from 20 – 5000 nm. Note that some of the arrays noticeable on the SEM image do not show any THG signal. This is due to experimental imperfections of the golden nanoribbons during the fabrication process.

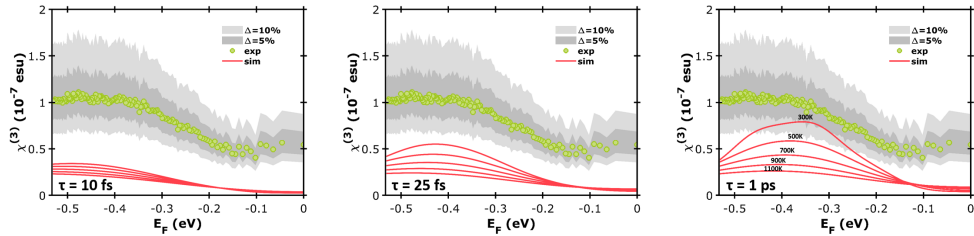


Figure 3. Comparison of the magnitude of the experimentally estimated  $\chi^{(3)}$  with the calculated value. The shaded areas around the green points represent the experimental uncertainty in our estimation of  $\chi^{(3)}$ . We calculate the error bars of the experimental data (green dots) with an uncertainty of 5% and 10% on the experimentally measured parameters, defined by the dark and light grey areas, respectively. The red solid lines show the theoretically calculated  $\chi^{(3)}$  at different electron temperatures for 10 fs, 25 fs and 1 ps, from left to right.

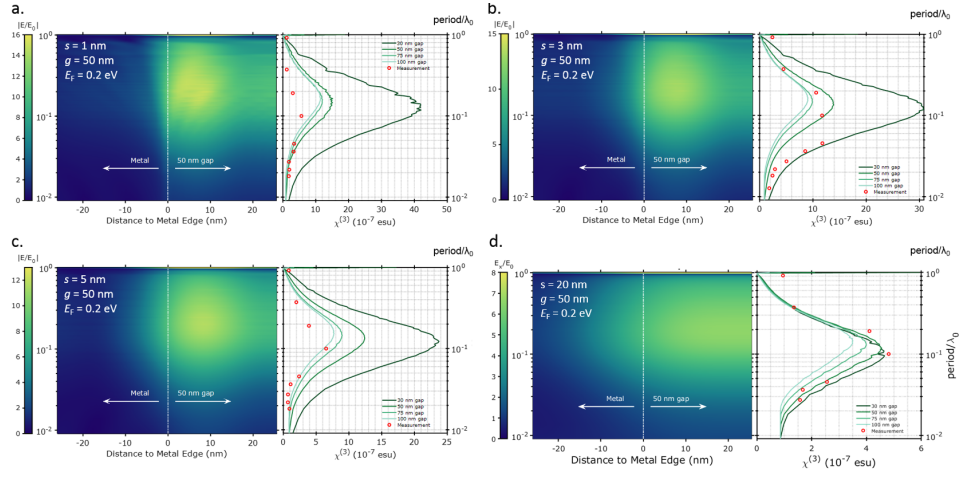


Figure 4. Field confinement in the gap between the nanoribbons and  $\chi^{(3)}$  as a function of the nanoribbon width. Each panel corresponds to a different  $\text{Al}_2\text{O}_3$  spacing  $s = [1, 3, 5, 20]$  nm.

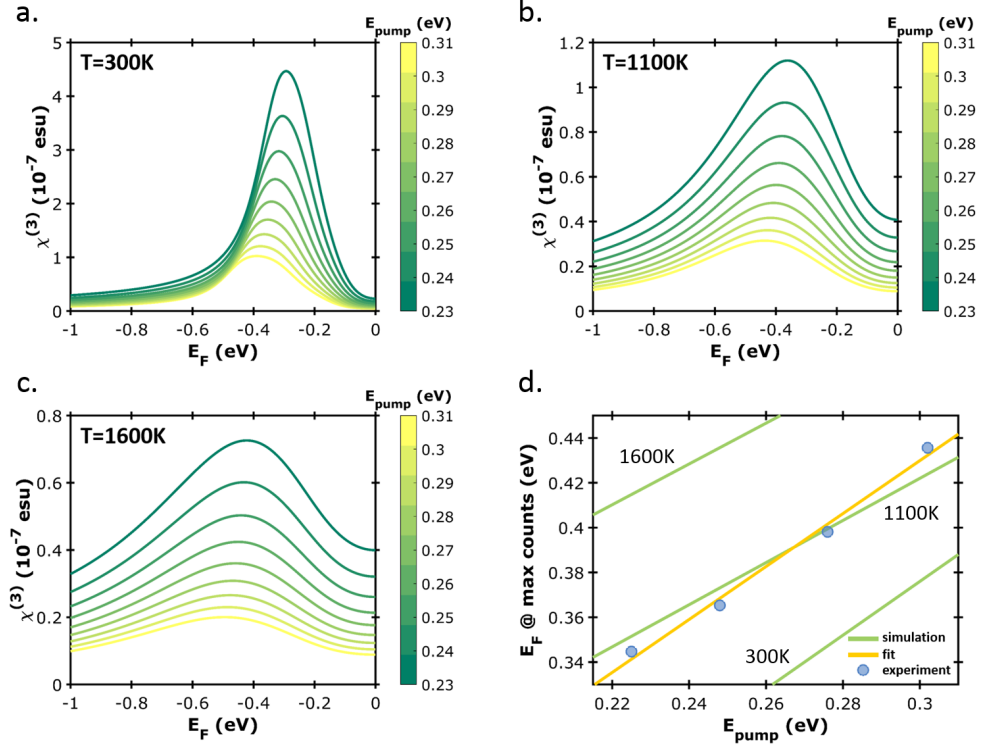


Figure 5. **Effect of the electron temperature on the optimum Fermi energy.** a-c. Simulations of the third-order susceptibility  $\chi^{(3)}$  as a function of the Fermi energy  $E_F$  for pump wavelengths in the  $\lambda_{pump} = 4000 - 5510$  nm ( $E_{pump} = 0.23 - 0.31$  eV) range and electron temperatures of 300 K, 1100 K and 1600 K, respectively. d. Blue dots show the experimental values of the  $E_F$  at which the maximum  $\chi^{(3)}$  are found in the gate measurement, for  $\lambda_{pump} = [5510, 5000, 4500, 4100]$  nm ( $E_{pump} = [0.225, 0.248, 0.276, 0.302]$  eV). The green solid lines are simulations at  $T_e = [300, 1100, 1600]$  K and the solid yellow line is a linear fit of the data points.

# Chapter 8

## Outlook

### 8.1 Superconducting Nanowire Single-Photon detectors (SNSP)

As previously mentioned in Section 6.2.3, we used SNSP detectors for the THG measurements. Here we will go through the basics of this detection system, as part of this thesis involved the installation, troubleshoot and characterization of a large cryogenic system containing 20 of these detectors. However, these detectors can only detect wavelengths up to  $2 \mu\text{m}$ , which is limiting the THG experiments to observe plasmons at longer wavelengths.

As its name indicates, this technology is based on a superconducting nanowire [63]. Currently there are two main superconducting materials that are used: niobium nitride (NbNi) and tungsten-silicide (WSi). The former is a crystalline material, which hinders the fabrication of smooth nanowires on a large area, but it also has a slightly higher critical temperature around  $T_c \sim 10.5 \text{ }^\circ\text{K}$  [86]. The latter, on the other hand, is an amorphous material, which facilitates the production of smooth and narrow nanoribbons. However, the critical temperature of this material is slightly lower,  $T_c \sim 3.7 \text{ }^\circ\text{K}$  [58]. Our detectors, built by PhotonSpot Inc., are WSi-based.

Superconducting materials only superconduct ( $R = 0 \Omega$ ) when they are cooled down below a certain critical temperature,  $T < T_c$ , and the bias current driven through is below a certain critical current,  $I < I_c$ . As shown in Fig. 8.1, under these conditions, when a photon strikes the nanowire, if it is absorbed, the photon energy is converted into heat energy that warms up a spot in the nanowire. In this so-called *hotspot*, the temperature surpasses the critical temperature,  $T > T_c$ , and the superconductivity is broken. This causes the resistance on this spot to increase rapidly. As a consequence, the current is forced to flow around this hotspot, leading to a current density larger than the critical current density,  $I > I_c$ , which also leads to a break of the superconductivity. As a result, the superconductivity breaks across the entire nanowire and this manifests as a drop in the bias current driven through it, which is actively monitored.

Due to the nanometric absorption cross section of a  $\sim 100 \text{ nm}$  wire, there are some tricks that one needs to engineer in order to reach high detection efficiencies. On one hand, as shown in Fig. 8.2a, one can shape the nanowire as a meander, so as to cover an area as large as the photon mode. With this method, the detection efficiency can be as high as  $\sim 30\%$ . Additionally, as shown in Fig. 8.2b, one can add a gold layer and upper mirror (anti-reflecting

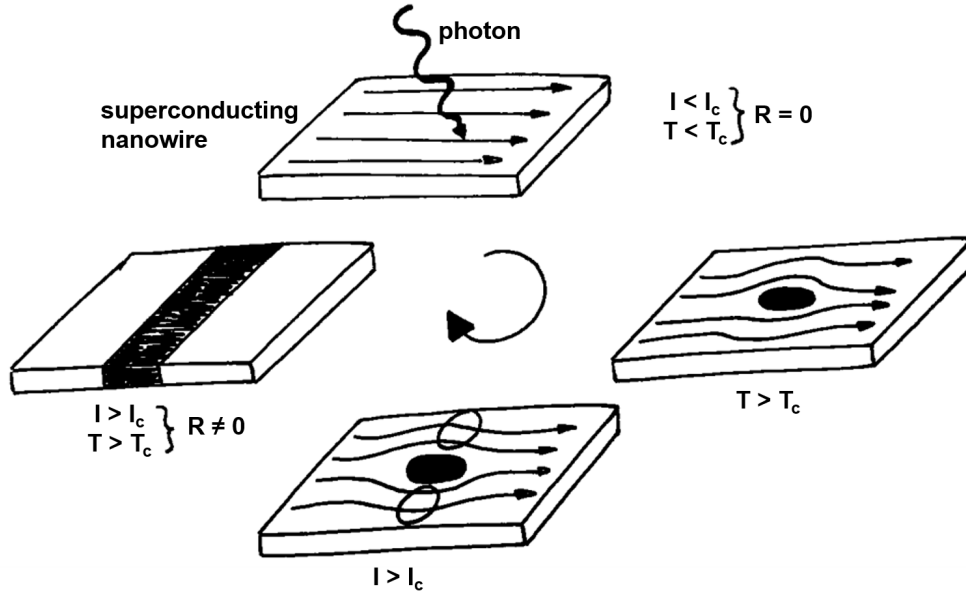


**Figure 8.1.** Conceptual sketch of the mechanism of SNSP detectors. The superconducting nanowire only shows this property ( $R = 0\Omega$ ) when it is cooled down below certain critical temperature  $T < T_c$  and the bias current driven through is below certain critical current  $I < I_c$ . When a photon is absorbed, its energy creates a *hotspot*, where the temperature raises above  $T_c$  and the superconductivity breaks. The current bunches around this hotspot, increasing the current density above  $I_c$ , which also breaks the superconductivity. Therefore, the absorption of a photon breaks the superconductivity throughout the entire nanowire and this can be monitored by the bias current.

coating) that acts as a cavity resonant to the incident photon. This method increases the number of times that the photon crosses the nanowire and can reach detection efficiencies as high as 98% [77]. In our case, this cavity was designed to resonantly enhance the detection of photons in the telecom range ( $\sim 1550$  nm). Nevertheless, due to the low quality factor of this cavity, as shown in Fig. 8.2c, the linewidth is very broad, allowing us to measure photons even at 1850 nm with up to 10% total detection efficiency, which is the longest wavelength at which we measured the THG signal in the work presented in Section 7.3.

In principle, there is no wavelength limitation inherent to this SNSP detectors. Longer wavelengths require narrower nanowires, due to their lower energy and consequently smaller hotspot. Furthermore, the cavity can also be designed to be resonant at longer wavelengths. Nevertheless, current SNSP detectors have only been demonstrated to work up to  $5\ \mu\text{m}$  with extremely low detection efficiency [57]. Apart from the decreased quality of narrower nanowires, the main current limitation is set by the silica fibers that bring the single photons to the detectors in the cryostat. The transmission of these fibers plummets above  $2.1\ \mu\text{m}$ , due to the absorption of silica.

Since the plasmon resonances in graphene are around  $8 - 10\ \mu\text{m}$ , we have a great interest in developing single-photon detectors with high efficiencies at these wavelengths, or more

realistically, at the third-harmonic wavelengths of these resonances ( $\sim 2 - 3 \mu\text{m}$ ). To do so, our collaborators at PhotonSpot Inc. grew thinner nanowire detectors with cavities resonant at  $\sim 3 \mu\text{m}$ . As for the optical fiber limitation, we tried two different fibers: chalcogenide fibers, which are available without any protective jacket but are extremely expensive and fragile, and fluoride fibers, which are affordable but always have a protective polymer jacket. In both cases, the main challenge was the feedthrough connecting the fiber from the outside to the inside of the cryostat. We first opted for chalcogenide fibers, as we needed to minimize the heat load in the cryostat. However, these turned out to be too fragile and expensive in order to pursue many trials, so we discarded these fibers as a feasible solution. We then switched to fluoride fibers (Single-mode  $\text{ZrF}_4$  fiber, Thorlabs P1-23Z-FC, with  $> 97.5\%$  transmission for  $2.3 - 3.6 \mu\text{m}$  and single-mode  $\text{InF}_3$  fiber, Thorlabs P1-32F-FC, with  $> 95\%$  transmission for  $3.2 - 4.6 \mu\text{m}$ ). The main challenge of these fibers was dealing with their protective jacket. Aside from the heat load that this jacket brings into the cryostat, this also requires a different method to feed the fiber into the cryostat. As a preliminary solution, we have designed the feedthrough shown in Fig. 8.3. The idea is to use a fiber mating sleeve to couple a fiber in the inside to a fiber in the outside. This sleeve is glued to a swagelok-type feedthrough, where we match the hole in the teflon part, which squeezes the mating sleeve and keeps it vacuum-tight. This design was tested to hold vacuum down to  $10^{-5}$  mbar and we also characterized its optical transmission to be  $\sim 85\%$  in the  $2.2 - 3.8 \mu\text{m}$  range. Unfortunately, the first tests showed detection efficiencies of  $< 10^{-3}\%$  at  $3 \mu\text{m}$ . We believe that this was associated to the mismatch between the field mode of the fiber and the nanowire itself, and the possible higher temperature of the nanowire due to the heatload provided by the fluoride fiber. Unfortunately, in order to debug and optimize this system, one would need to constantly warm up and cool down the cryostat, which leads to very long down times of all the detectors. This was not possible at that moment, as many people in the group rely on the SNSP detectors. We plan to pursue the development of a long wavelength detector system in the near future, as we will have a new cryostat that will contain most of the detectors used by other projects. This will enable us to debug the problem without interrupting other experiments.

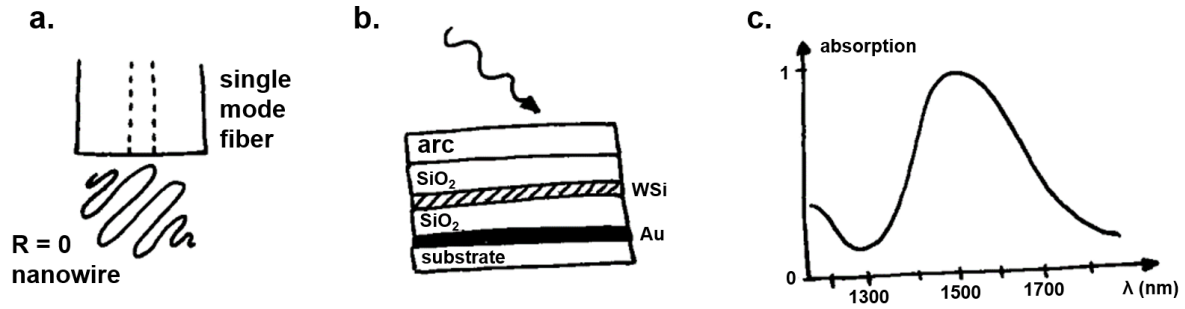


**Figure 8.2. SNSP detector fabrication details.** **a.** The nanowire can be designed as a meander to cover the entire optical mode of the photon coming out of the optical fiber. **b.** On the growing process, one can add a layer of gold, creating a cavity around the nanowire, which will increase the number of times the photon crosses it and thus the detection efficiency. **c.** Absorption of our cavities optimized at 1550 nm.

## 8.2 Looking for the first quantum signatures

Although we successfully observed a *giant* enhancement of the THG signal with graphene-metal heterostructures, all the measurements performed until now are classical and show no quantum features. The most straightforward way to move towards a quantum third-order nonlinear process, is spontaneous FWM. In Section 2.2.3 we introduced the FWM process, where two photons with the same frequency  $\omega_1$  mix together with a third photon with  $\omega_2$  to give rise to a new photon with energy  $\omega_{\text{FWM}} = 2\omega_1 - \omega_2$ . This process is conventionally known as FWM, and refers to a stimulated FWM process, where  $\omega_2$  stimulates the system to decay into that  $\omega_{\text{FWM}}$  determined by energy conservation. Specially in graphene, where the atomic thickness of the nonlinear medium discards any phase-matching condition, the absence of this stimulation photon  $\omega_2$  would allow the system to freely decay into any two photons that obey energy conservation. This process without any stimulating photon is spontaneous FWM and it does correspond to a quantum process, where the heralded decay photons would be antibunched and show strong spectral correlations [69].

However, the lack of phase matching conditions or any other constrain would make the process extremely inefficient at any specific wavelength. Note that, although one could simply not constrain the wavelengths, experimental devices are usually optimized for a narrow range of wavelengths, which would limit the collection of these photon pairs over the entire wavelength regime. Hence, we need some external stimulation that would keep the quantum nature of the process but yet guide the system into certain specific decay wavelengths. For this goal we have two approaches in mind that we will start testing in the near future.

The first idea is to place a monolayer graphene in a microcavity [93], which would act as the stimulation for the nonlinear process, forcing the system to decay into the resonance of the cavity and its corresponding energy-conservation photon pair. To be more precise, with the MIRA set at 780 nm, we would pump the system with  $\omega_1 = 1454$  nm (signal), and

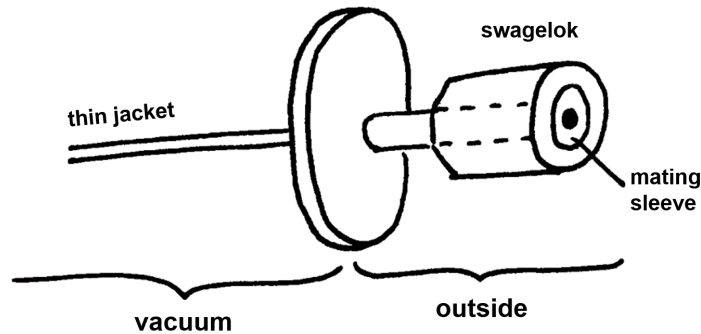


**Figure 8.3. Designed optical feedthrough.** We use a swagelok-type feedthrough with a mating sleeve to couple a fiber outside the cryostat to a fiber inside the cryostat. All the parts are glued using vacuum-friendly epoxy.

collect the photon pairs at the cavity resonance  $\omega_c = 1280$  nm and the corresponding energy-conserved pair  $\omega_{\text{FWM}} = 1683$  nm (idler). Together with the group of Michael Trupke at the University of Vienna, we have already designed and built microcavities with a monolayer CVD graphene grown on the flat mirror of the cavity. These have not yet been characterized but the experimental design and measurement procedure have been already developed.

The first stage of the setup will be similar to that introduced in Section 6.2.3, where the pump beams are first tightly focused onto the graphene sample, which is moved in and out of the focal point, and the signal is later collimated before being coupled into the detector. For this experiment, we plan to first measure the stimulated FWM signal, so we would use the signal at  $\omega_1 = 1454$  nm and idler at  $\omega_2 = 1683$  nm from the OPO and look for the stimulated FWM signal at  $\omega_{\text{FWM}} = 1280$  nm. In the collection stage, we will use a notch filter to suppress the pump, and will use a dichroic mirror to separate  $\omega_2$  from  $\omega_{\text{FWM}}$ . These would then be collected and detected by two independent SNSP detectors. Finally, using a coincidence counter, we would look for coincidences between these two signals. The jump from the stimulated to the spontaneous process will, in theory, just require turning off the stimulating beam  $\omega_2$  and looking for coincidences.

Although the efficiency of such a process would be extremely low, we believe it would be a stepping stone towards strong nonlinear effects at the single-photon level. Indeed, such an emission could be used as a heralded single-photon source, where the detection of a photon on one arm ensures the presence of another photon in the other arm.

The second idea towards spontaneous FWM would be based on graphene plasmon resonances. In this case, the idea would be substituting the resonance of the microcavity by the resonance of the plasmon itself. The measurement method would thus be exactly the same but the input wavelengths  $\omega_1$  and  $\omega_2$  would have to be adapted so that the stimulating beam matches the plasmon resonance,  $\omega_2 = \omega_p$ .



# Chapter 9

## Conclusion

When I started this thesis I had barely heard about graphene in the news and all I knew about my project was summarized in a very ambitious grant proposal. At first, I was incredibly excited about it. A single layer of carbon atoms interacting with light to create single photons with unprecedented efficiency. Can you imagine? Coming from the field of photonic quantum computation, the promise of a deterministic single-photon source was indeed a reason to be eager.

However, reality struck me after the first meeting with our collaborators, when I understood all the challenges that the project entailed. In a nutshell, we needed a tunable laser in the mid-IR, we needed single-photon detectors with high efficiency at longer wavelengths than had ever been achieved and we needed graphene devices with strong nonlinear plasmonic resonances that we could excite. We could buy the tunable laser, the rest we and our collaborators had to develop ourselves. Does not sound so bad, does it?

This was the beginning of an incredible journey; we were given an empty lab and a large amount of resources to make this happen. What else did we need? Time, persistence and patience. And this is what we did. We tackled each problem along the way for 5 years and the details are collected in the previous 100 pages. However, I just want to end with a sweet taste and a sense of achievement. Because we should not underestimate what we have done and I believe we are indeed not so far from achieving our ultimate goal of measuring single-photon level effects from graphene plasmons.

After our thorough study of the third-order nonlinearity in graphene via THG, we now have the tools and knowledge to continue our research towards spontaneous FWM, and measure the first signatures of quantum light with graphene. Additionally, we have also demonstrated that graphene-based quantum logic gates can beat the performance of their classical equivalents, potentially overcoming the scalability limitation of current quantum computations.

In summary, the work presented in my thesis brings us closer towards deterministic single-photon sources and quantum logic gates, which are the two main drawbacks of current photonic quantum computation.



# List of Figures

2.1	<b>Conceptual sketches to understand Maxwell's equations</b> <b>a.</b> When the total vector field flows exiting the surface given by $S$ , the divergence will be positive. In contrast, when the divergence is negative, it indicates that the total vector field flows inside $S$ . <b>b.</b> Sketch of magnetic fields around a magnet. The divergence of any given surface, such as $S$ or $S'$ , is always zero, indicating that there is no source of magnetic field. <b>c.</b> Faraday's experiment that made him discover that an electric field changing in space induces a magnetic field changing in time. . . . .	9
2.2	<b>Continuity conditions.</b> The fields in the interface between two materials with permittivities $\epsilon_1$ and $\epsilon_2$ . . . . .	11
2.3	<b>Sketch of Fresnel coefficients.</b> Refraction and transmission components of an incident <b>a.</b> $s$ -polarized and (TE mode) <b>b.</b> $p$ -polarized (TM mode) light. .	13
3.1	<b>Plasmon.</b> <b>a.</b> When a photon impinges into a metal, the free electrons in the conduction band follow the electromagnetic oscillation, creating a wave of electrons, known as plasmon, whose wavelength can be three times shorter than that of the initial photon. <b>b.</b> We look for plasmonic modes in the interface between two materials with opposite real dielectric constant signs; i.e., a conductor and a dielectric, where the modes propagate in the $x$ -direction ( $\beta = k_x$ ) and are confined in the $z$ -direction. Note that the plasmon field decays in the $x$ -direction as $e^{i\beta x}$ . However, for the sake of clarity, this is not represented in the sketch. . . . .	18
3.2	<b>Metallic sphere in a uniform electrostatic field.</b> We consider a homogeneous and isotropic sphere, with radius $a$ and dielectric constant $\epsilon(\omega)$ , in an isotropic and non-absorbing medium. . . . .	21
3.3	<b>Sketch of a metallic stripe on planar graphene.</b> Graphene is infinite in $x$ and $y$ directions and the metallic stripe has a width $L$ , centered at $x = 0$ and extends infinitely in the $y$ direction. The incident electromagnetic wave $\mathbf{E}$ propagates in the $z$ direction and is polarized in the $x$ direction. . . . .	23
3.4	<b>Electric field outside the metal stripe.</b> As a result of the incident electromagnetic wave $E^{\text{ext}}$ , there is a field originating on the edge of the metal and propagating away from it in the $x$ direction. For $L/\lambda_0/2$ the resonance condition is found, where the field strength is much stronger than with the non-resonant cases. Additionally, the field strength decreases as $x$ increases and far away, there is no sign of plasmonic behaviour and only a homogenous field above zero can be observed. Image taken from [33], page 157. . . . .	24

4.1	<b>Carbon allotropes. a.</b> Graphite. Graphene layers stick to each other via Van der Waals forces to form macroscopic size stacks. <b>b.</b> Buckminsterfullerene or bucky ball. 60 carbon atoms form a mesh of pentagons and hexagons and acquire a stable hollow sphere. <b>c.</b> Single-walled carbon nanotubes. Graphene sheets are rolled up to form cylinders with different diameters in the nanometer scale. Depending on the edges of the initial graphene and the chirality at which this is rolled up, its electronic properties can be tuned. <b>d.</b> Graphene. Carbon atoms form hexagons to build a stable 2D structure where electrons can hop from atom to atom, leading to extraordinary electronic mobility. . . . .	28
4.2	<b>Graphene’s electronic properties. a.</b> Sketch of the orbitals of a carbon atom. The $sp^2$ hybrid orbitals lie on the $x - y$ plane with $120^\circ$ separation between them. These have strong $\sigma$ bonds with the neighboring atoms. The $p_z$ orbital extends along the $z$ axis, with an unpaired electron that can create weak $\pi$ bonds. <b>b.</b> Valence and conduction bands of graphene. These are completely symmetric and intersect at points $\mathbf{K}$ and $\mathbf{K}'$ , where $E_F = 0$ . <b>c.</b> For relatively low energies ( $ E_E  < 2$ eV) the dispersion relation of graphene is linear and has the shape of two cones known as the Dirac cones. This is due to its similarity to the Dirac equation for massless fermions. At the intersection of the cones, known as the Dirac point, $E_F = 0$ . . . . .	29
4.3	<b>Real and reciprocal lattices of graphene. a.</b> In the real lattice, the unit cell is determined by the shaded area, where A and B are two atoms separated by the minimum distance $a_0 = 1.421\text{\AA}$ . $a_1$ and $a_2$ are the lattice vectors of the Bravais sublattice describing the honeycomb structure of graphene. <b>b.</b> In the reciprocal lattice, the first Brillouin zone is defined by the shaded area with the center at $\Gamma$ . $b_1$ and $b_2$ are the basis vectors of the reciprocal lattice. Image taken from[91]. . . . .	30
4.4	<b>Dispersion relation of graphene a.</b> Sketch of the optical dispersion relation of graphene and <b>b.</b> density plot summarizing all the allowed transitions in graphene, including intraband and interband transitions, and excitations of SPPs. This is calculated via the random-phase approximation (RPA) model for a free standing graphene ( $\epsilon_1 = \epsilon_2 = 1$ ) with $E_F = 0.4$ eV and $\mu = 10^4$ cm <sup>2</sup> /Vs. Image taken from [26], page 37. . . . .	32
5.1	<b>a.</b> Every point in the Bloch sphere represents a quantum state. The computational basis, $ 0\rangle$ and $ 1\rangle$ , is defined along the $z$ -axis, while the diagonal basis, $ +\rangle$ and $ -\rangle$ , lies on the $x$ -axis. <b>b.</b> CNOT and <b>c.</b> CZ truth tables. These gates flip or change the phase of a target qubit if the control qubit is 1. . . . .	38
5.2	<b>Logic gates built from the universal NAND gate.</b> . . . . .	39

5.3 **CNOT gate.** **a.** Implementation of the CNOT gate proposed by Pittman, *et al.* [72], where the gate succeeds when a single photon is detected on each polarization-sensitive detector. **b.** Quantum circuit of a CNOT gate operation with single-qubit  $\pi/2$  rotations ( $R_y, R_z$ ), two SWAP<sup>1/2</sup> gates (1/2) and a Pauli z operator ( $\sigma_z$ ). . . . . 41

5.4 **SWAP<sup>1/2</sup> gate with a directional coupler and atoms.** **a.** The waveguides of the directional coupler are surrounded by an atom cloud that shows single-photon transparency and strong two-photon absorption. **b.** Energy-level diagram of a three-level atom. *Left:* If the energy difference between the energy levels is the same, both single- and two-photon states can be absorbed. *Right:* However, if the energy of the second level is shifted, a single photon is no longer resonant but two photons can still be absorbed, as energy conservation is obeyed. 42

5.5 **Concept of a SWAP<sup>1/2</sup> gate with a directional coupler.** **a.** On a SWAP gate, the qubit always swaps modes between the input and the output ports. **b.** When this SWAP operation is only performed halfway, one can no longer define whether the qubit has swapped modes or not, thus creating a superposition of output modes. In a directional coupler, two waveguides are placed so close to each other that the evanescent field of the photon allows it to swap from one mode to the other. **c.** There is a certain interaction length  $L$ , after which it is certain that the qubit has swapped modes. **d.** However, if this interaction length is shortened to  $L/2$ , one can no longer determine whether the SWAP has happened or not, leading to a superposition of output modes; that is, a SWAP<sup>1/2</sup> operation. . . . . 46

5.6 **SWAP<sup>1/2</sup> gate** **a.** Sketch of the arrangement of the waveguides in a directional coupler. **b.** Refractive index as a function of  $x$ . In this example the waveguides have different refractive indices but we have considered the case with identical waveguides. **c.** Field distributions of both waveguides, where the overlapping tails contribute to the coupling between them. . . . . 47

5.7 **Sketched examples of the Zeno effect interpretations.** **a.** If the system is prepared in the excited state at  $t_0$ , in the absence of external forces, it will decay into the ground state at time  $t_d$ . However, if continuous observations are carried out, these measurements will keep collapsing the system into the excited state and will keep it in place. **b.** If the polarizer is set perpendicular to the incident light, no light will make it through. However, if the polarizer angle is slowly rotated starting from the polarization of the incident light, this will evolve in a way to adapt and avoid the loss channel. In this case the beam will change the polarization to that set by the polarizer. . . . . 49

5.8 **Bomb-tester thought experiment.** **a.** When the upper and lower arms of a Mach-Zehnder interferometer are balanced, if a photon is inserted in the lower input port, its self-interference will make it always exit through the upper output port. **b.** However, when a bomb is placed on the upper arm, if the bomb is not detonated, the photon has 75% and 25% probability of exiting the upper and upper ports, respectively. Thus, one can detect whether a bomb is present without ever interacting with it. . . . . 51

5.9 **Concatenated Mach-Zehnder interferometers.** Kwiat, *et al.* noticed that the probability of determining whether a bomb is present in the interferometer or not can be arbitrarily high if one concatenates several Mach-Zehnder interferometers. The success probability is thus proportional to the total number of BSs chained. . . . . 52

6.1 **Photon-blockade.** **a.** Classically, when a nonlinear medium is placed in a cavity, the resonance frequency depends on the refractive index of the material. At the same time, this refractive index varies with intensity. Thus, when a resonant photon enters the cavity, the refractive index of the nonlinear media changes, which leads to a shift of the cavity resonance, which means that the next photon will need some extra energy to be resonant. **b.** A graphene nanostructure works as a cavity for plasmons. When a photon excites a plasmon in the graphene, the resonance energy of the nanostructure shifts so a second photon would require a different frequency to be resonant to the system. 54

6.2 **Setup in Exeter.** A 1kHz pulsed laser pumps two independent OPAs with tunable wavelengths in the 480 – 2600 nm. These two beams are then spatially and temporally overlapped on the graphene sample and the generated FWM signal is collected at the angle given by momentum conservation. This is done with an APD. Hence, the measurement consists of monitoring the detected signal as a function of the temporal overlap between the beams; only when both beams coincide temporally will the FWM process take place. . . . . 57

6.3 **Setup in Vienna.** A 80MHz pulsed laser pumps an OPO, whose signal and idler beams cover the 1 – 4  $\mu\text{m}$  wavelength range. These are further mix on a DFG process, covering the spectrum all the way to 10  $\mu\text{m}$ . Due to the architecture of the setup, both spatial and temporal overlap are given. The beams are then focused down and collimated via two short focal length lenses, in between which the sample is placed. A set of series will then filter the pump beams from the created nonlinear signal (FWM, THG...) and these are measured using a single-photon APD or a SNSP detector, depending on the wavelength. The measurement thus consists on detecting the nonlinear signal as the sample is moved in and out of the focus; the signal is biggest at the focal point. . . . . 58

6.4 **Optical components.** **a.** It is recommendable screwing the post holder directly on the table holes instead of using clamps. This way it is easier to keep the beamline straight when other optical components are added. **b.** Sketch of the pinhole with the dispersed beam after this goes through the tight focus lens. **c.** Sketch of the lend holders with translation degree in the x and y direction. . . . . 60

6.5 **Alignment procedure step 1.** Place pinholes  $p_1$  and  $p_2$  on the chosen line and steer the beam to follow this line by using mittors  $m_1$  and  $m_2$ . First do it roughly using the IR card that allows you seeing the beam at 1500 nm and then proceed with the fine alignment by walking the beam into the powermeter, as explained in the main text. . . . . 60

6.6 **Alignment procedure step 2.** Once the beam is properly align, proceed inserting the first lens  $L_1$  by taking pinhole  $p_3$  as a reference. Afterwards, collimate back the beam with lens  $L_2$ . Use pinhole  $p_4$  as a reference, both close to  $L_2$  and very far from it. Placing  $L_2$  on a translation stage will provide you the required accuracy to find the optimal distance between  $L_1$  and  $L_2$ . . . . . 61

6.7 **Alignment procedure step 3.** After setting the lenses, you need to couple the light into a multi-mode fiber. Use mirrors  $m_3$  and  $m_4$  to walk the beam into the fiber coupler. Use the x-y-z defrees of freedom of the coupling lens to further optimize the coupling. Spectral filters will clear the desired wavelength from leakage light from the MIRA pump, and signal and idler beams of the OPO. . . . . 62

6.8	<p><b>Picture of the setup and sample. a.</b> Top view of the setup. The red line is a visual guide representing the laser beam that travels from right to left in the picture. <math>p_1</math> and <math>p_2</math> are the pinholes used for the initial alignment, <math>L_1</math> and <math>L_2</math> are the tight focusing and collimating lenses, respectively, and <math>m_3</math> and <math>m_4</math> are the mirrors to walk the beam and couple it into the multi-mode fiber. In this case, the collected signal is detected with an avalanche photodiode (APD). Note that all the optical components in the setup are standard parts from Thorlabs.</p> <p><b>b.</b> Sample with gold nanoribbons. The visible gold pads correspond to the source and drain connections of the different graphene stripes shown in Fig. 6.9. These are connected one at a time, depending on the stripe that is being measured. On the other hand, the gate is shared. . . . .</p>	63
6.9	<p><b>SEM images of the graphene with gold nanoribbon sample.</b> The samples build by the group of Prof. Frank Koppens at ICFO have different arrays of nanoribbons with different widths, indicated in the image in nm units. The dark vertical stripes are the areas where there is graphene. There is a replica of the same kind of nanoribbon arrays with and without graphene in order to make reference measurements. On the right panel, the good quality of the nanoribbons can be appreciated. . . . .</p>	64
6.10	<p><b>Sample component contributions to the TH signal.</b> The sample allows us to study the individual contribution of each component of the sample. <b>a.</b> We find no nonlinear signal when there is only substrate or gold nanoribbons and <b>b.</b> shows a significant signal with bare graphene and an extremely enhanced signal when gold nanoribbons are added on top of the graphene. Note the logarithmic scales of the plots. . . . .</p>	64
6.11	<p><b>TH signal enhancement quantification. a.</b> Power dependence of the TH for bare graphene (red) and graphene with gold nanoribbons of different widths (yellow through blue). The interception points found with the fits, whose slopes are set to 3, enable calculating the enhancement of the signals due to the field confinement. In the case of THG, the maximum enhancement is 1580 for <math>W = 200</math> nm. <b>b.</b> Calculated <math>\chi^{(3)}</math> for different nanoribbon widths with input power <math>P = 0.4</math> mW. . . . .</p>	65

---

6.12	<b>Study of the input and output polarization.</b> <b>a.</b> When rotating the polarization of the input light, as theoretically predicted, bare graphene is isotropic to the incident polarization while the gold nanoribbons impose a $\cos^6 \theta$ dependence for TH , maximizing the signal when the incident light is perpendicular to the direction of the nanoribbons. <b>b.</b> Changing the output polarization while keeping the input polarization fixed shows that the pump and TH signals are copolarized. The discrepancies between the theory and data are due to the polarization-dependent efficiency of the SNSP detectors. . . . .	66
6.13	<b>Fermi energy tuning via electrical doping.</b> <b>a.</b> TH signal as a function of the Fermi energy $E_F$ tuned by an applied gate voltage. When the $E_F$ increases, the TH signal increases as it matches the single-, two- and three-photon transitions. As expected, these resonances shift with the input wavelength. <b>b.</b> and <b>c.</b> show TH signal gating measurements for nanoribbon arrays with widths $W = (55 \text{ nm}, 47 \text{ nm})$ and gap between nanoribbons $g = (45 \text{ nm}, 53 \text{ nm})$ , respectively. Apart from the large modulation due to the single-, two- and three-photon transition resonances, there are some additional signal variations that can be explained by the excitations of plasmons in graphene. . . . .	67
8.1	<b>Conceptual sketch of the mechanism of SNSP detectors.</b> The superconducting nanowire only shows this property ( $R = 0\Omega$ ) when it is cooled down below certain critical temperature $T < T_c$ and the bias current driven through is below certain critical current $I < I_c$ . When a photon is absorbed, its energy creates a <i>hotspot</i> , where the temperature raises above $T_c$ and the superconductivity breaks. The current bunches around this hotspot, increasing the current density above $I_c$ , which also breaks the superconductivity. Therefore, the absorption of a photon breaks the superconductivity through the entire nanowire and this can be monitored by the bias current. . . . .	106
8.2	<b>SNSP detector fabrication details.</b> <b>a.</b> The nanowire can be designed as a meander to cover the entire optical mode of the photon coming out of the optical fiber. <b>b.</b> On the growing process, one can add a layer of gold, creating a cavity around the nanowire, which will increase the number of times the photon crosses it and thus the detection efficiency. <b>c.</b> Absorption of our cavities optimized at 1550 nm. . . . .	108
8.3	<b>Designed optical feedthrough.</b> We use a swagelok-type feedthrough with a mating sleeve to couple a fiber outside the cryostat to a fiber inside the cryostat. All the parts are glued using vacuum-friendly epoxy. . . . .	109



# Acknowledgements

This thesis would not be possible without the trust and support of my supervisor, who blindly gave this chance to that girl that was lost in life. Don't get me wrong, I am still lost but thanks to this opportunity that you gave me I have acquired quite some skills (and a title!) that will surely be helpful on the way. So, Philip, thank you very much for believing in me and believing in impossible projects that turn out to be possible. Milagro!

I cannot be more thankful to have a Lee in my life. I mean, who doesn't want one? Although you are the definition of what being a good scientist means and you know more than the wikipedia, you have always made me feel like my opinion mattered and my questions weren't stupid. We know they were not always the smartest but we can leave this between us. Even outside the lab, thank you for being the perfect conference buddy; I will not forget the runs in california or the too-late sunsets in Rio. So, Lee, thank you for being the best mentor that one could wish for.

Thank you very much to all my collaborators; to the graphene-team, to Teo and David, to Joel, José Ramón and Javier, to David and Frank, to Tom, Justus and Euan, thank you very much for your hospitality and making it so easy and pleasant to work with you.

I wanna thank the person that brought me to Vienna and has been the biggest support through this PhD. And what a PhD! I have to recall the words of an old professor of mine: Having a PhD is just a prove that you can take a lot of shit. I believe many of us can relate to those wise words. So, thank you so much Thomas, for being there, in the *latina-drama-queen* moments when things didn't work out and the *euforic-reggeaton-party* moments when things went well. Bihotzez, eskerrik asko, maittia.

Etxeko guztiei, Ama eta aitari bereziki, milesker horren urrun egon harren zuen maitasun eta laguntza honaino iritsiarazi izanagatik. Kuadrilari, aspaldian zuekin egon ez harren inoiz joan izan ez banintz bezela sentiarazteagatik.

I would like to finish thanking all the people that make feel Vienna like home. To my running friends, specially to Stevan, who is the best runner I know, not only because he runs ultras like he drinks coffee, but because he also enjoys grandma runs with me. To my cooking friends; Jess, Meaghan, Stevan, Sophia, Lorenzo, Michael, you just know the essence of life and the kind of evenings I like. To my whiskey-friday boys, cause I love our most stupid conversations. To Thomas' friends, for the fun cocktail nights and perfect surf trips. This acknowledgements section would be longer than the thesis itself if I would actually show my gratitude to every single person that is important to me so, please, do not feel offended if I did not mention you.



# Bibliography

- [1] S. Aaronson. Lecture notes for quantum information and computation.
- [2] E. Abbe. Beiträge zur theorie des mikroskops und der mikroskopischen wahrnehmung. *Archiv f. mikrosk. Anatomie*, 9:413–468, 1873.
- [3] D. R. M. Arvidsson-Shukur and C. H. W. Barnes. Quantum counterfactual communication without a weak trace. *Physical Review A*, 94(6):062303, 2016.
- [4] N. W. Ashcroft and N. D. Mermin. *Solid State Physics*. Harcourt College Publishers, New York, 1976.
- [5] Z. Bai and G. Huang. Enhanced third-order and fifth-order kerr nonlinearities in a cold atomic system via rydberg-rydberg interaction. *Optics express*, 24(5):4442–4461, 2016.
- [6] Q. Bao and K. P. Loh. Graphene photonics, plasmonics, and broadband optoelectronic devices. *ACS nano*, 6(5):3677–3694, 2012.
- [7] D. S. Bethune, C. H. Kiang, M. S. de Vries, G. Gorman, R. Savoy, and R. Vazquez, J. Beyers. Cobalt-catalysed growth of carbon nanotubes with single-atomic layer walls. *Nature*, 363:605–607, 1993.
- [8] R. W. Boyd. *Nonlinear Optics*. Academic Press, New York, 2003.
- [9] H. E. Burton. The optics of euclid. *J. Opt. Soc. Am.*, 35(5):357–372, 1945.
- [10] J. Chen, M. Badioli, P. Alonso-Gonzalez, S. Thongrattanasiri, F. Huth, J. Osmond, M. Spasenovic, A. Centeno, A. Pesquera, P. Godignon, A. Z. Elorza, N. Camara, F. J. García de Abajo, R. Hillenbrand, and F. H. L. Koppens. Optical nano-imaging of gate-tunable graphene plasmons. *Nature*, 487:77–81, 2012.
- [11] J. Cheng, N. Vermeulen, and J. Sipe. Third order optical nonlinearity of graphene. *New Journal of Physics*, 16(5):053014, 2014.
- [12] J. L. Cheng, N. Vermeulen, and J. Sipe. Third-order nonlinearity of graphene: Effects of phenomenological relaxation and finite temperature. *Physical Review B*, 91(23):235320, 2015.
- [13] I. L. Chuang and Y. Yamamoto. Simple quantum computer. *Physical Review A*, 52(5):3489, 1995.

- [14] R. Ciesielski, A. Comin, M. Handloser, K. Donkers, G. Piredda, A. Lombardo, A. C. Ferrari, and A. Hartschuh. Graphene near-degenerate four-wave mixing for phase characterization of broadband pulses in ultrafast microscopy. *Nano letters*, 15(8):4968–4972, 2015.
- [15] M. Currie, J. D. Caldwell, F. J. Bezares, J. Robinson, T. Anderson, H. Chun, and M. Tadjer. Quantifying pulsed laser induced damage to graphene. *App. Rev. Lett.*, 99(211909), 2011.
- [16] J. P. Dowling, J. D. Franson, H. Lee, and G. J. Milburn. Towards scalable linear-optical quantum computers. In *Experimental Aspects of Quantum Computing*, pages 205–213. Springer, 2005.
- [17] E. Dremetsika, B. Dlubak, S.-P. Gorza, C. Ciret, M.-B. Martin, S. Hofmann, P. Seneor, D. Dolfi, S. Massar, P. Emplit, et al. Measuring the nonlinear refractive index of graphene using the optical kerr effect method. *Optics letters*, 41(14):3281–3284, 2016.
- [18] P. Drude. Zur elektronentheorie der metalle. *Annalen der Physik*, (306):566–613, 1900.
- [19] P. Drude. Zur elektronentheorie der metalle. *Annalen der physik*, 306(3):566–613, 1900.
- [20] K. J. Ebeling. *Integrated optoelectronics: waveguide optics, photonics, semiconductors*. Springer Science & Business Media, 2012.
- [21] A. C. Elitzur and L. Vaidman. Quantum mechanical interaction-free measurements. *Found. Phys.*, 23:987–997, 1993.
- [22] J. S. Fakonas, H. Lee, Y. A. Kelaita, and H. A. Atwater. Two-plasmon quantum interference. *Nat. Photonics*, 8:317–320, 2014.
- [23] Z. Fei, G. O. Andreev, W. Bao, L. M. Zhang, A. S. McLeod, C. Wang, M. K. Stewart, Z. Zhao, G. Dominguez, M. Thiemens, et al. Infrared nanoscopy of dirac plasmons at the graphene-sio2 interface. *Nano letters*, 11(11):4701–4705, 2011.
- [24] Z. Fei, A. Rodin, G. Andreev, W. Bao, A. McLeod, M. Wagner, L. Zhang, Z. Zhao, M. Thiemens, G. Dominguez, et al. Gate-tuning of graphene plasmons revealed by infrared nano-imaging. *Nature*, 487(7405):82, 2012.
- [25] R. P. Feynmand. Simulating physics with computers. *International Journal of Theoretical Physics*, 21:467–48, 1982.
- [26] I. S. Flores. *Plasmonic response of graphene nanostructures*. PhD thesis, Universidad de Santiago de Compostela Departamento de Física Aplicada, 2015.

- 
- [27] J. Franson, B. Jacobs, and T. Pittman. Quantum computing using single photons and the zeno effect. *Physical Review A*, 70(6):062302, 2004.
- [28] F. J. García de Abajo. Graphene plasmonics: challenges and opportunities. *Acs Photonics*, 1(3):135–152, 2014.
- [29] F. J. García de Abajo. Graphene plasmonics: Challenges and opportunities. *ACS Photonics*, 1:135–152, 2014.
- [30] E. Garmire. Nonlinear optics in daily life. *Optics express*, 21(25):30532–30544, 2013.
- [31] S. Gasparoni, J.-W. Pan, P. Walther, T. Rudolph, and A. Zeilinger. Realization of a photonic controlled-not gate sufficient for quantum computation. *Physical review letters*, 93(2):020504, 2004.
- [32] J. Gea-Banacloche. Impossibility of large phase shifts via the giant kerr effect with single-photon wave packets. *Physical Review A*, 81(4):043823, 2010.
- [33] P. A. D. Goncalves and N. M. R. Peres. *An Introduction to Graphene Plasmonics*. World Scientific, Singapore, 2016.
- [34] D. J. Griffiths. Introduction to electrodynamics, 2005.
- [35] A. Grigorenko, M. Polini, and K. Novoselov. Graphene plasmonics. *Nature photonics*, 6(11):749, 2012.
- [36] R. W. Heeres, L. P. Kouwenhoven, and V. Zwiller. Quantum interference in plasmonic circuits. *Nature Nanotechnology*, 8:719—722, 2013.
- [37] E. Hendry, P. J. Hale, J. Moger, A. K. Savchenko, and S. A. Mikhailov. Coherent nonlinear optical response of graphene. *Phys. Rev. Lett.*, 105:097401, 2010.
- [38] R. Hillenbrand, T. Taubner, and F. Keilmann. Phonon-enhanced light–matter interaction at the nanometre scale. *Nature*, 418(6894):159–162, 2002.
- [39] C.-K. Hong, Z.-Y. Ou, and L. Mandel. Measurement of subpicosecond time intervals between two photons by interference. *Physical review letters*, 59(18):2044, 1987.
- [40] S.-Y. Hong, J. I. Dadap, N. Petrone, P.-C. Yeh, J. Hone, and R. M. Osgood Jr. Optical third-harmonic generation in graphene. *Physical Review X*, 3(2):021014, 2013.
- [41] S. Iijima and T. Ichihashi. Single-shell carbon nanotubes of 1-nm diameter. *Nature*, 363:603–605, 1993.

- [42] D. A. Iranzo, S. Nanot, E. J. C. Dias, I. Epstein, C. Peng, D. K. Efetov, M. B. Lundberg, R. Parret, J. Osmond, J.-Y. Hong, J. Kong, D. R. Englund, N. M. R. Peres, and F. H. L. Koppens. Probing the ultimate plasmon confinement limits with a van der waals heterostructure. *Science*, 360:291–295, 2018.
- [43] M. Jablan, M. Soljačić, and H. Buljan. Plasmons in graphene: fundamental properties and potential applications. *Proceedings of the IEEE*, 101(7):1689–1704, 2013.
- [44] J. D. Jackson. *Classical Electrodynamics*. Wiley, New York, 1975.
- [45] T. Jiang, D. Huang, J. Cheng, X. Fan, Z. Zhang, Y. Shan, Y. Yi, Y. Dai, L. Shi, K. Liu, et al. Gate-tunable third-order nonlinear optical response of massless dirac fermions in graphene. *Nature Photonics*, 2018.
- [46] L. Ju, B. Geng, J. Horng, C. Girit, M. Martin, Z. Hao, H. A. Bechtel, X. Liang, A. Zettl, Y. R. Shen, et al. Graphene plasmonics for tunable terahertz metamaterials. *Nature nanotechnology*, 6(10):630, 2011.
- [47] M. Kauranen and A. V. Zayats. Nonlinear plasmonics. *Nat. Photon.*, 6:737–748, 2012.
- [48] E. Knill, R. Laflamme, and G. J. Milburn. A scheme for efficient quantum computation with linear optics. *Nature*, 409:46–52, 2001.
- [49] F. H. Koppens, D. E. Chang, and F. J. García de Abajo. Graphene plasmonics: A platform for strong light-matter interactions. *Nano Lett.*, 11:3370–3377, 2011.
- [50] H. W. Kroto, J. R. Heath, S. C. O’Brien, R. F. Curl, and R. E. Smalley.  $c_{60}$ : Buckminsterfullerene. *Nature*, (318):162–163, 1985.
- [51] N. Kumar, J. Kumar, C. Gerstenkorn, R. Wang, H.-Y. Chiu, A. L. Smirl, and H. Zhao. Third harmonic generation in graphene and few-layer graphite films. *Physical Review B*, 87(12):121406, 2013.
- [52] P. Kwiat, H. Weinfurter, T. Herzog, A. Zeilinger, and M. A. Kasevich. Interaction-free measurements. *Phys. Rev. Lett.*, 74(4763), 1995.
- [53] P. M. Leung and T. C. Ralph. Optical zeno gate: bounds for fault tolerant operation. *New Journal of Physics*, 9(7):224, 2007.
- [54] R. Loudon. The quantum theory of light. *American Journal of Physics*, 42(11):1041–1042, 1974.
- [55] A. Lund and T. Ralph. Nondeterministic gates for photonic single-rail quantum logic. *Physical Review A*, 66(3):032307, 2002.

- 
- [56] S. A. Maier. *Plasmonics. Fundamentals and Applications*. Springer, New York, 2007.
- [57] F. Marsili, F. Bellei, F. Najafi, A. E. Dane, E. A. Dauler, R. J. Molnar, and K. K. Berggren. Efficient single photon detection from 500 nm to 5  $\mu$ m wavelength. *Nano Lett.*, 12:4799–4804, 2012.
- [58] F. Marsili, V. B. Verma, J. A. Stern, S. Harrington, A. E. Lita, T. Gerrits, I. Vayshenker, B. Baek, M. D. Shaw, R. P. Mirin, and S. W. Nam. Detecting single infrared photons with 93% efficiency. *Nature*, 7(13), 2013.
- [59] J. C. Maxwell. A dynamical theory of the electromagnetic field. *Philosophical Transactions of the Royal Society of London*, 155:459–512, 1865.
- [60] S. A. Mikhailov. Theory of the giant plasmon-enhanced second-harmonic generation in graphene and semiconductor two-dimensional electron systems. *Phys. Rev. B*, 84:045432, 2011.
- [61] S. A. Mikhailov. Quantum theory of the third-order nonlinear electrodynamic effects of graphene. *Phys. Rev. B*, 93:085403, 2016.
- [62] B. Misra and E. C. G. Sudarshan. The Zeno’s paradox in quantum theory. *J. Math. Phys.*, 18:756, 1977.
- [63] C. M. Natarajan, M. G. Tanner, and R. H. Hadfield. Superconducting nanowire single-photon detectors: physics and applications. *IOPscience*, 25(063001), 2012.
- [64] A. Neville, C. Sparrow, R. Clifford, E. Johnston, P. M. Birchall, A. Montanaro, and A. Laing. Classical boson sampling algorithms with superior performance to near-term experiments. *Nat. Phys*, 13:1153–1157, 2017.
- [65] G. X. Ni, A. S. McLeod, Z. Sun, L. Wang, L. Xiong, K. W. Post, S. S. Sunku, B.-Y. Jiang, J. Hone, C. R. Dean, M. M. Fogler, and D. N. Basov. Fundamental limits to graphene plasmonics. *Nature*, 557:530–533, 2018.
- [66] M. A. Nielsen and I. L. Chuang. *Quantum Computation and Quantum Information*. Cambridge University Press, 2013.
- [67] K. S. Novoselov, A. K. Geim, S. V. Morozov, D. Jiang, Y. Zhang, S. V. Dubonos, I. V. Grigorieva, and A. A. Firsov. Electric field effect in atomically thin carbon films. *Science*, (306):666–669, 2004.
- [68] J. L. O’Brien, G. J. Pryde, A. G. White, T. C. Ralph, and D. Branning. Demonstration of an all-optical quantum controlled-not gate. *Nature*, 426(6964):264–267, 2003.

- [69] C. Okoth, A. Cavanna, T. Santiago-Cruz, and M. Chekhova. Microscale generation of entangled photons without momentum conservation. *Physical Review Letters*, 123(26):263602, 2019.
- [70] D. O’Shea, C. Junge, J. Volz, and A. Rauschenbeutel. Fiber-optical switch controlled by a single atom. *Phys. Rev. Lett.*, 110:193601, 2013.
- [71] J. M. Pitarke, V. M. Silkin, E. V. Chulkov, and P. Echenique. Theory of surface plasmons and surface-plasmon polaritons. *Rep. Prog. Phys.*, (70):1–87, 2007.
- [72] T. Pittman, M. Fitch, B. Jacobs, and J. Franson. Experimental controlled-not logic gate for single photons in the coincidence basis. *Physical Review A*, 68(3):032316, 2003.
- [73] T. Pittman, B. Jacobs, and J. Franson. Probabilistic quantum logic operations using polarizing beam splitters. *Physical Review A*, 64(6):062311, 2001.
- [74] T. Pittman, B. Jacobs, and J. Franson. Demonstration of nondeterministic quantum logic operations using linear optical elements. *Physical Review Letters*, 88(25):257902, 2002.
- [75] J. Preskill. Lecture notes for physics 229: Quantum information and computation. *California Institute of Technology*, 16, 1998.
- [76] T. C. Ralph and G. J. Pryde. Optical quantum computation. In *Progress in optics*, volume 54, pages 209–269. Elsevier, 2010.
- [77] D. V. Reddy, A. E. Lita, S. W. Nam, R. P. Mirin, and V. B. Verma. Achieving 98% system efficiency at 1550 nm in superconducting nanowire single photon detectors. In *Rochester Conference on Coherence and Quantum Optics (CQO-11)*, page W2B.2. Optical Society of America, 2019.
- [78] L. Rego, K. M. Dorney, N. J. Brooks, Q. L. Nguyen, C.-T. Liao, J. San Román, D. E. Couch, A. Liu, E. Pisanty, M. Lewenstein, L. Plaja, H. C. Kapteyn, M. M. Murnane, and C. Hernández-García. Generation of extreme-ultraviolet beams with time-varying orbital angular momentum. *Science*, 364(6447), 2019.
- [79] J.-G. Ren, P. Xu, H.-L. Yong, L. Zhang, S.-K. Liao, J. Yin, W.-Y. Liu, W.-Q. Cai, M. Yang, L. Li, et al. Ground-to-satellite quantum teleportation. *Nature*, 549(7670):70, 2017.
- [80] H. Rostami and M. Polini. Theory of third-harmonic generation in graphene: A diagrammatic approach. *Physical Review B*, 93(16):161411, 2016.

- 
- [81] H. Ruska, B. v. Borries, and E. Ruska. Die bedeutung der übermikroskopie für die virusforschung. *Archiv für die gesamte Virusforschung*, 1(1):155–169, 1939.
- [82] J. R. M. Saavedra. *Classical and quantum aspects of the optical response at the nanoscale*. PhD thesis, ICFO - Institut de Ciències Fotòniques, 2018.
- [83] K. Sanaka, T. Jennewein, J.-W. Pan, K. Resch, and A. Zeilinger. Experimental nonlinear sign shift for linear optics quantum computation. *Physical review letters*, 92(1):017902, 2004.
- [84] H. Schmidt and A. Imamoglu. Giant kerr nonlinearities obtained by electromagnetically induced transparency. *Optics letters*, 21(23):1936–1938, 1996.
- [85] J. H. Shapiro. Single-photon kerr nonlinearities do not help quantum computation. *Physical Review A*, 73(6):062305, 2006.
- [86] T. Shiino, S. Shiba, N. Sakai, T. Yamakura, L. Jiang, Y. Uzawa, H. Maezawa, and S. Yamamoto. Improvement of the critical temperature of superconducting nbtin and nbn thin films using the aln buffer layer. *Superconductor Science and Technology*, 23(4):045004, 2010.
- [87] G. Soavi, G. Wang, H. Rostami, D. G. Purdie, D. De Fazio, T. Ma, B. Luo, J. Wang, A. K. Ott, D. Yoon, et al. Broadband, electrically tunable third-harmonic generation in graphene. *Nature nanotechnology*, page 1, 2018.
- [88] M. I. Stockman. Nanoplasmonics: The physics behind the applications. *Phys. Today*, 64(2):39–44, 2011.
- [89] J. W. Suk, A. Kitt, C. W. Magnuson, Y. Hao, S. Ahmed, J. An, A. K. Swan, B. B. Goldberg, and R. S. Ruoff. Transfer of cvd-grown monolayer graphene onto arbitrary substrates. *ACS nano*, 5(9):6916–6924, 2011.
- [90] R. R. A. Syms and J. R. Cozens. *Optical guided waves and devices*. McGraw-Hill, New York, 1992.
- [91] E. Thune. Investigations on carbon nanotubes. 09 2004.
- [92] M. Von Ardenne. Das elektronen-rastermikroskop. *Zeitschrift für Physik*, 109(9-10):553–572, 1938.
- [93] G. Wachter, S. Kuhn, S. Minniberger, C. Salter, P. Asenbaum, J. Millen, M. Schneider, J. Schalko, U. Schmid, A. Felgner, et al. Silicon microcavity arrays with open access and a finesse of half a million. *Light: Science & Applications*, 8(1):1–7, 2019.

- [94] A. Woessner, M. B. Lundberg, Y. Gao, A. Principi, P. Alonso-González, M. Carrega, K. Watanabe, T. Taniguchi, G. Vignale, M. Polini, J. Hone, R. Hillenbrand, and F. H. L. Koppens. Highly confined low-loss plasmons in graphene-boron nitride heterostructures. *Nat. Mater.*, 14:421—425, 2015.
- [95] L.-A. Wu, P. Walther, and D. A. Lidar. No-go theorem for passive single-rail linear optical quantum computing. *Scientific reports*, 3:1394, 2013.
- [96] H. Yan, X. Li, B. Chandra, G. Tulevski, Y. Wu, M. Freitag, W. Zhu, P. Avouris, and F. Xia. Tunable infrared plasmonic devices using graphene/insulator stacks. *Nature nanotechnology*, 7(5):330, 2012.
- [97] H. Yan, Z. Li, X. Li, W. Zhu, P. Avouris, and F. Xia. Infrared spectroscopy of tunable dirac terahertz magneto-plasmons in graphene. *Nano letters*, 12(7):3766–3771, 2012.
- [98] N. Yoshikawa, T. Tamaya, and K. Tanaka. High-harmonic generation in graphene enhanced by elliptically polarized light excitation. *Science*, 356(6339):736–738, 2017.
- [99] J. Zeuner, A. N. Sharma, M. Tillmann, R. Heilmann, M. Gräfe, A. Moqanaki, A. Sza-meit, and P. Walther. Integrated-optics heralded controlled-not gate for polarization-encoded qubits. *npj Quantum Information*, 4(1):1–7, 2018.
- [100] Y.-X. Zhang, Y. Zhang, and K. Mølmer. Directional launching of surface plasmons by polariton superradiance. *ArXiv*, 1807.03682, 2018.
- [101] Z. Zhao, A.-N. Zhang, Y.-A. Chen, H. Zhang, J.-F. Du, T. Yang, and J.-W. Pan. Experimental demonstration of a nondestructive controlled-not quantum gate for two independent photon qubits. *Physical review letters*, 94(3):030501, 2005.